

Surfactant and gravity dependent instability of two-layer channel flows: Linear theory covering all wave lengths

Alexander L. Frenkel, David Halpern and Adam J. Schweiger

December 4, 2018

Department of Mathematics, University of Alabama, Tuscaloosa AL 35487, USA

Abstract

A linear stability analysis of a two-layer plane Couette flow of two immiscible fluid layers with different densities, viscosities and thicknesses, bounded by two infinite parallel plates moving at a constant relative velocity to each other, with an insoluble surfactant monolayer along the interface and in the presence of gravity is carried out. The normal modes approach is applied to the equations governing flow disturbances in the two layers. These equations, together with boundary conditions at the plates and the interface, yield a linear eigenvalue problem. When inertia is neglected the velocity amplitudes are the linear combinations of certain hyperbolic functions, and a quadratic dispersion equation for the increment, that is the complex growth rate, is obtained where coefficients depend on the aspect ratio, the viscosity ratio, the basic velocity shear, the Marangoni number Ma that measures the effects of surfactant, and the Bond number Bo that measures the influence of gravity. An extensive investigation is carried out that examines the stabilizing or destabilizing influences of these parameters. Since the dispersion equation is quadratic in the growth rate, there are two continuous branches of the normal modes: a robust branch that exists even with no surfactant, and a surfactant branch that, to the contrary, vanishes when $Ma \downarrow 0$. Due to the availability of explicit forms for the growth rates, in many instances the numerical results are corroborated with analytical asymptotics. For the less unstable branch, a mid-wave interval of unstable wavenumbers (Halpern and Frenkel [2003]) sometimes co-exists with a long-wave one. We study the instability landscape, determined by the threshold curve of the long-wave instability and the critical curve of the mid-wave instability in the (Ma, Bo) -plane. The changes of the extremal points of the critical curves with the variation of the other parameters, such as the viscosity ratio, and the extrema bifurcation points are investigated.

1 Introduction

Surfactants are surface active compounds that reduce the surface tension between two fluids, or between a fluid and a solid. Frenkel and Halpern [2002] (hereafter referred to as FH) and Halpern and Frenkel [2003] (from now on referred to as HF) uncovered that certain stable surfactant-free Stokes flows become unstable if an interfacial surfactant is introduced. For this, the interfacial shear of velocity must be nonzero; in particular, this instability disappears if the basic flow is stopped. In contrast to the well-known instability of two viscous fluids (Yih [1967]) which needs inertia effects for its existence, this instability may exist in the absence of fluid inertia. With regard to multi-fluid horizontal channel flows, this instability has been further studied in a number of papers, such as Blyth and Pozrikidis [2004b], Pozrikidis [2004], Blyth and Pozrikidis [2004a], Frenkel and Halpern [2005], Wei [2005], Frenkel and Halpern [2006], Halpern and Frenkel [2008], Bassom et al. [2010], Peng and Zhu [2010], Kalogirou and Papageorgiou [2016], Picardo et al. [2016], and Frenkel and Halpern [2017]. In the latter paper, we have added gravity to the long-wave considerations of FH. Since in the absence of surfactants gravity can be either stabilizing or destabilizing depending on the

flow parameters, the interaction of the Rayleigh-Taylor instability with the surfactant instability leads to interesting phenomena.

In the present work, we expand the linear stability analysis of Frenkel and Halpern [2017], which was confined to long waves, by including disturbances of arbitrary wavenumbers. The current paper can also be regarded as an extension of HF, who considered arbitrary wavenumbers, by incorporating the effects of gravity. As was indicated in Frenkel and Halpern [2017], one can expect a rich landscape of stability properties, especially since there are two active normal modes of infinitesimal disturbances corresponding to the presence of two interfacial functions: the interface displacement function and the interfacial surfactant concentration (FH, HF). Since the growth rates of the normal modes satisfy a (complex) quadratic equation, and thus are relatively simple, in many instances numerical results may enjoy analytic (asymptotic) corroboration. The stability properties of two-layer Couette flows with both the interfacial surfactant and gravity effects for arbitrary wavenumbers were the subject of the dissertation Schweiger [2013]. These studies are further developed and expanded in the present paper. In section 2, the stability problem is formulated. In section 3, the dispersion equation is obtained. The long-wave stability properties are considered in section 4, while in section 5 we consider normal modes of arbitrary wavelengths and study the so-called mid-wave instability (uncovered in HF but significantly modified by gravity effects). In section 6, we consider the instability landscape in the (Marangoni number, Bond number)-plane that is determined by the threshold curve of the long-wave instability and the critical curve of the mid-wave instability, and study how it changes with the other parameters. Finally, section 7 contains discussion and concluding remarks. Some of the more technical information appears in Appendices.

2 Stability problem formulation

The general framework and governing equations of the problem were given before (see Schweiger [2013], Frenkel and Halpern [2016], Frenkel and Halpern [2017]) and are as follows. Two immiscible Newtonian fluid layers with different densities, viscosities and thicknesses are bounded by two infinite horizontal plates, a distance $d = d_1 + d_2$ apart, with the top plate moving at a constant relative velocity, U^* , as shown in figure 1. The z^* -axis is the spanwise, vertical, coordinate perpendicular to the moving plates, with the upper plate located at $z^* = d_2$ and the lower plate located at $z^* = -d_1$, and with $z^* = 0$ determining the location of the unperturbed liquid-liquid interface. (The symbol $*$ indicates a dimensional quantity.) The direction of the horizontal x^* -axis is parallel to the plates. At the interface, the surface tension, σ^* , depends on the concentration of the insoluble surfactant monolayer, Γ^* . The frame of reference is fixed at the liquid-liquid interface so that the velocity of the lower plate is $-U_1^*$, and that of the upper plate is U_2^* , where $U_1^* + U_2^* = U^*$, the velocity of the top plate relative to the bottom plate. In the base state, the horizontal velocity profiles are linear in z^* , the interface is flat, and the surfactant concentration is uniform. Once disturbed, the surfactant concentration is no longer uniform and the deflection of the interface is represented by the function $\eta^*(x^*, t^*)$ where t^* represents the time. The infinitesimal disturbances may grow under the action of the Marangoni and/or gravity forces (Frenkel and Halpern [2017]). The governing equations for this problem are given, for example, in Frenkel and Halpern [2016], in both dimensional and dimensionless forms. (Also, the dimensionless form of these equations can be found in Frenkel and Halpern [2017].) We use the following notations (with $j = 1$ for the bottom liquid layer and $j = 2$ for the top liquid layer): ρ_j is the density; $\mathbf{v}_j^* = (u_j^*, w_j^*)$ is the fluid velocity vector with horizontal component u_j^* and vertical component w_j^* ; p_j^* is the pressure; μ_j is the viscosity; and g is the gravity acceleration.

We assume the dependence of surface tension σ^* on the surfactant concentration Γ^* to be given by the Langmuir isotherm relation (e.g., Edwards et al. [1991]). For the small disturbances,

$$\sigma^* = \sigma_0 - E(\Gamma^* - \Gamma_0), \quad (2.1)$$

where σ_0 is the base surface tension corresponding to the base surfactant concentration Γ_0 and the known constant $E := -(\partial\sigma^*/\partial\Gamma^*)|_{\Gamma^*=\Gamma_0}$ is the elasticity parameter.

We use the following dimensionless variables:

$$(x, z, \eta) = \frac{(x^*, z^*, \eta^*)}{d_1}, \quad t = \frac{t^*}{d_1\mu_1/\sigma_0}, \quad \mathbf{v}_j = (u_j, w_j) = \frac{(u_j^*, w_j^*)}{\sigma_0/\mu_1},$$

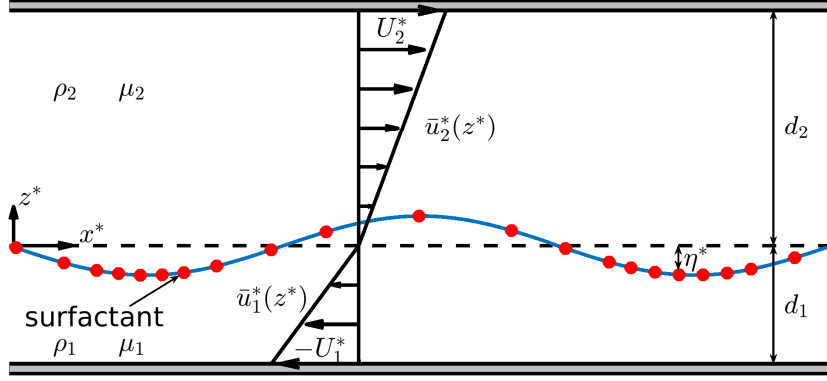


Figure 1: Sketch of a disturbed two-layer Couette flow of two horizontal liquid layers with different thicknesses, viscosities, and mass densities. The insoluble surfactant monolayer is located at the interface and is indicated by the dots. The (spanwise) uniform gravity field with a constant acceleration g is not shown.

$$p_j = \frac{p_j^*}{\sigma_0/d_1}, \quad \Gamma = \frac{\Gamma^*}{\Gamma_0}, \quad \sigma = \frac{\sigma^*}{\sigma_0}. \quad (2.2)$$

As in Frenkel and Halpern [2016, 2017], the dimensionless velocity field of the basic Couette flow, with a flat interface, $\eta = 0$, uniform surface tension, $\bar{\sigma} = 1$, and corresponding surfactant concentration, $\bar{\Gamma} = 1$ (where the over-bar indicates a base quantity), is

$$\bar{u}_1(z) = sz, \quad \bar{w}_1 = 0, \quad \text{and} \quad \bar{p}_1 = -\text{Bo}_1 z \quad \text{for} \quad -1 \leq z \leq 0, \quad (2.3)$$

$$\bar{u}_2(z) = \frac{s}{m}z, \quad \bar{w}_2 = 0, \quad \text{and} \quad \bar{p}_2 = -\text{Bo}_2 z \quad \text{for} \quad 0 \leq z \leq n, \quad (2.4)$$

where $\text{Bo}_j := \rho_j g d_1^2 / \sigma_0$ is the Bond number of the layer j , $m = \mu_2 / \mu_1$ is the ratio of the viscosities, and $n = d_2 / d_1$ is the ratio of the thicknesses. The constant s represents the base interfacial shear rate of the bottom layer, $s = D\bar{u}_1(0)$, where $D = d/dz$, and is used to characterize the flow instead of the relative velocity of the plates. It is straightforward to establish that $U = \mu_1 U^* / \sigma_0 = s(1 + n/m)$. The disturbed state with small deviations (indicated by the tilde, \sim) from the base flow is given by

$$\eta = \tilde{\eta}, \quad u_j = \bar{u}_j + \tilde{u}_j, \quad w_j = \tilde{w}_j, \quad p_j = \bar{p}_j + \tilde{p}_j, \quad \Gamma = \bar{\Gamma} + \tilde{\Gamma}. \quad (2.5)$$

The normal modes are disturbances of the form

$$(\tilde{\eta}, \tilde{u}_j, \tilde{w}_j, \tilde{p}_j, \tilde{\Gamma}) = [h, \hat{u}_j(z), \hat{w}_j(z), \hat{f}_j(z), G] e^{i\alpha x + \gamma t}, \quad (2.6)$$

where $\hat{u}_j(z)$, $\hat{w}_j(z)$, and $\hat{f}_j(z)$ are the complex amplitudes that depend on the depth, α is the wavenumber of the disturbance, G is the constant amplitude of $\tilde{\Gamma}$ ($G = \hat{\Gamma}$), h is the constant amplitude of $\tilde{\eta}$ ($h = \hat{\eta}$), and (complex) γ is the increment, $\gamma = \gamma_R + i\gamma_I$. The stability of the flow depends on the sign of the growth rate γ_R : if $\gamma_R > 0$ for some normal modes then the system is unstable; and if $\gamma_R < 0$ for all normal modes then the system is stable. The linearized governing equations for the disturbances translate into the following system for the normal mode amplitudes (See Frenkel and Halpern [2016, 2017] for the omitted details). The continuity equation becomes

$$\hat{u}_j = \frac{i}{\alpha} D \hat{w}_j. \quad (2.7)$$

Eliminating the pressure disturbances from the horizontal and vertical components of the momentum equations with neglected inertia yields the well-known Orr-Sommerfeld equations, here for the vertical velocity disturbances,

$$m_j (D^2 - \alpha^2)^2 \hat{w}_j = 0, \quad (2.8)$$

where $m_j := \mu_j/\mu_1$ (so that $m_1 = 1$ and $m_2 = m$). The disturbances of the velocities are subject to the boundary conditions at the plates and at the interface. At the plates, the boundary conditions are

$$D\hat{w}_1(-1) = 0, \hat{w}_1(-1) = 0, D\hat{w}_2(n) = 0, \hat{w}_2(n) = 0. \quad (2.9)$$

The kinematic boundary condition and surfactant transport equation yield, respectively,

$$\gamma h - \hat{w}_1 = 0 \quad (z = 0), \quad (2.10)$$

$$\gamma G - D\hat{w}_1 + si\alpha h = 0 \quad (z = 0). \quad (2.11)$$

(Note that equation (2.11) is the normal form of equation (2.9) in Frenkel and Halpern [2017] which was derived in HF, and was mentioned there to be consistent with the more general equation of Wong et al. [1996]. The last term in (2.11) comes from the Taylor expansion of the base state fluid velocities at $z = \eta(x, t)$.) Continuity of velocity at the interface yields

$$\hat{w}_1 - \hat{w}_2 = 0 \quad (z = 0) \quad (2.12)$$

and

$$D\hat{w}_2 - D\hat{w}_1 - i\alpha sh \left(\frac{1-m}{m} \right) = 0 \quad (z = 0). \quad (2.13)$$

To obtain the linearized homogeneous normal stress condition, the pressure amplitude, \hat{f}_j , is first written in terms of \hat{w}_j . From the horizontal momentum equation it is given by

$$\alpha^2 \hat{f}_j = m_j (D^2 - \alpha^2) D\hat{w}_j. \quad (2.14)$$

The interfacial tangential stress condition is

$$mD^2\hat{w}_2 - D^2\hat{w}_1 + \alpha^2(m\hat{w}_2 - \hat{w}_1) - \alpha^2 G\text{Ma} = 0 \quad (z = 0), \quad (2.15)$$

where

$$\text{Ma} := E\Gamma_0/\sigma_0$$

is the Marangoni number, and the normal stress condition is

$$mD^3\hat{w}_2 - 3m\alpha^2 D\hat{w}_2 - D^3\hat{w}_1 + \text{Bo}\alpha^2 h + 3\alpha^2 D\hat{w}_1 + \alpha^4 h = 0 \quad (z = 0), \quad (2.16)$$

where Bo is the effective Bond number

$$\text{Bo} = \text{Bo}_1 - \text{Bo}_2 = \frac{(\rho_1 - \rho_2)gd_1^2}{\sigma_0}. \quad (2.17)$$

Note that Bo can be negative, unlike the parameters n , m , s and Ma. Equations (2.8)-(2.13), (2.15) and (2.16) form the eigenvalue boundary value problem for the disturbances, which determines the growth rate as a function of the wavenumber α and the parameters s , m , n , Ma, and Bo. The eigenvalue, the increment γ , satisfies a quadratic equation which is obtained in the next section.

3 Dispersion relation; special points of dispersion curves

For finite aspect ratio, n , the general solutions of (2.8) are given by

$$\hat{w}_j(z) = a_j \cosh(\alpha z) + b_j \sinh(\alpha z) + c_j z \cosh(\alpha z) + d_j z \sinh(\alpha z), \quad (3.1)$$

where the coefficients a_j , b_j , c_j , and d_j are determined by the boundary conditions up to a common normalization factor. Equation (2.12) yields $a_2 = a_1$, which is used to eliminate a_2 from the equations.

Applying the plate velocity conditions, equation (2.9), the coefficients c_1 and d_1 are expressed in terms of a_1 and b_1 , and the coefficients c_2 and d_2 are expressed in terms of a_1 and b_2 :

$$\begin{aligned}\hat{w}_1(z) &= a_1 \cosh(\alpha z) + b_1 \sinh(\alpha z) + \frac{1}{\alpha} [-s_\alpha^2 b_1 + (s_\alpha c_\alpha + \alpha) a_1] z \cosh(\alpha z) \\ &+ \frac{1}{\alpha} [-(s_\alpha c_\alpha - \alpha) b_1 + c_\alpha^2 a_1] z \sinh(\alpha z)\end{aligned}\quad (3.2)$$

and

$$\begin{aligned}\hat{w}_2(z) &= a_1 \cosh(\alpha z) + b_2 \sinh(\alpha z) - \frac{1}{\alpha n^2} [s_{\alpha n}^2 b_2 + (s_{\alpha n} c_{\alpha n} + \alpha n) a_1] z \cosh(\alpha z) \\ &+ \frac{1}{\alpha n^2} [(s_{\alpha n} c_{\alpha n} - \alpha n) b_2 + c_{\alpha n}^2 a_1] z \sinh(\alpha z),\end{aligned}\quad (3.3)$$

where

$$c_\alpha = \cosh(\alpha), \quad s_\alpha = \sinh(\alpha), \quad c_{\alpha n} = \cosh(\alpha n), \quad s_{\alpha n} = \sinh(\alpha n). \quad (3.4)$$

We substitute these velocity expressions into the interfacial conditions (2.13), (2.15), and (2.16) to obtain a linear nonhomogeneous system for a_1 , b_1 , and b_2 . Solving this system yields a_1 , b_1 , and b_2 in terms of h and G . Hence, we have the velocities $\hat{w}_j(z)$ in terms of h and G . Then the kinematic boundary condition (2.10) and surfactant transport equation (2.11) yield a linear homogeneous system for h and G , written in matrix form as

$$\begin{bmatrix} (\gamma + A_{11}) & A_{12} \\ A_{21} & (\gamma + A_{22}) \end{bmatrix} \begin{bmatrix} h \\ G \end{bmatrix} = \begin{bmatrix} 0 \\ 0 \end{bmatrix}, \quad (3.5)$$

where A_{11} , A_{12} , A_{21} , and A_{22} are known functions of the wavenumber α and the system parameters (see Appendix B). The condition for the existence of nontrivial solutions is $\det(A) = (\gamma + A_{11})(\gamma + A_{22}) - A_{12}A_{21} = 0$; this yields a quadratic equation for the mode increment γ . We write this 'dispersion equation' in the form

$$F_2 \gamma^2 + F_1 \gamma + F_0 = 0, \quad (3.6)$$

and its two solutions in the forms

$$\gamma = \frac{1}{2F_2} \left(-F_1 + [F_1^2 - 4F_2F_0]^{1/2} \right) \quad (3.7)$$

or

$$\gamma = -\frac{F_1}{2F_2} + \left[\left(\frac{F_1}{2F_2} \right)^2 - \frac{F_0}{F_2} \right]^{1/2}, \quad (3.8)$$

where F_2 , F_1 , and F_0 are as follows:

$$\begin{aligned}\text{Re}(F_2) &= \frac{1}{\alpha^4} \{ (c_{\alpha n}^2 + \alpha^2 n^2) (s_\alpha^2 - \alpha^2) m^2 + 2 (s_\alpha c_\alpha s_{\alpha n} c_{\alpha n} - \alpha^2 n + \alpha^4 n^2) m \\ &+ (s_{\alpha n}^2 - \alpha^2 n^2) (c_\alpha^2 + \alpha^2) \},\end{aligned}\quad (3.9)$$

$$\text{Im}(F_2) = 0, \quad (3.10)$$

$$\begin{aligned}\text{Re}(F_1) &= \frac{1}{2\alpha^3} \{ m \text{Ma} (s_{\alpha n} c_{\alpha n} + \alpha n) (s_\alpha^2 - \alpha^2) + \text{Ma} (s_{\alpha n}^2 - \alpha^2 n^2) (s_\alpha c_\alpha + \alpha) \\ &+ \frac{1}{\alpha^2} m (s_{\alpha n} c_{\alpha n} - \alpha n) (s_\alpha^2 - \alpha^2) (\text{Bo} + \alpha^2) \\ &+ \frac{1}{\alpha^2} (s_{\alpha n}^2 - \alpha^2 n^2) (s_\alpha c_\alpha - \alpha) (\text{Bo} + \alpha^2) \},\end{aligned}\quad (3.11)$$

$$\text{Im}(F_1) = \frac{s}{\alpha^2} (1 - m) (s_{\alpha n} c_{\alpha n} - \alpha n + n^2 s_\alpha c_\alpha - \alpha n^2), \quad (3.12)$$

$$\text{Re}(F_0) = \frac{\text{Ma}}{4\alpha^4} (s_{\alpha n}^2 - \alpha^2 n^2) (s_\alpha^2 - \alpha^2) (\text{Bo} + \alpha^2), \quad (3.13)$$

$$\text{Im}(F_0) = -\frac{\text{Ma}}{2\alpha} s (s_{\alpha n}^2 - s_\alpha^2 n^2). \quad (3.14)$$

Because the coefficients of the quadratic equation (3.6) are complex numbers, it is clear that in general the imaginary parts of the solutions γ_1 and γ_2 are non zero which signifies an oscillatory instability. One can see that the growth rate γ_R (as well as the increment γ) has the function symmetry property

$$\gamma_R(-n\alpha; ns, m^{-1}, n^{-1}, \text{Ma}, n^2\text{Bo}) = nm\gamma_R(\alpha; s, m, n, \text{Ma}, \text{Bo}). \quad (3.15)$$

In view of this symmetry, it is sufficient to consider stability for $n \geq 1$. (See Frenkel and Halpern (2016) for comprehensive details.) We also note the following facts. All the coefficients of the quadratic equation (3.6) are continuous at each point $(\alpha; s, m, n, \text{Ma}, \text{Bo})$ for the physical values of α and the parameters. All parenthetical expressions in equations (3.9) through (3.14) containing hyperbolic functions are positive. Therefore, $F_2 > 0$, and $\text{Re}(F_1)$ and $\text{Re}(F_0)$ are positive for $\text{Bo} \geq 0$. For $\text{Bo} < 0$, the functions $\text{Re}(F_1)$ and $\text{Re}(F_0)$ are positive provided $\alpha^2 > -\text{Bo}$. Also, $\text{Im}(F_1) > 0 (< 0)$ for $m < 1 (> 1)$. Furthermore, $\text{Im}(F_0) = 0$ for $n = 1$, and negative for $n > 1$. The zero gravity limit studied in FH and HF is recovered when $\text{Bo} = 0$. We want to investigate the dependence of the growth rates $\gamma_R = \text{Re}(\gamma)$ on the wavenumber α and the parameters n, m, s, Ma and Bo in the ranges $0 < \alpha < \infty, 1 \leq n < \infty, 0 < m < \infty, 0 \leq s < \infty, 0 \leq \text{Ma} < \infty$ and $-\infty < \text{Bo} < \infty$.

It is an elementary fact of complex analysis that there are two analytic, and therefore continuous, branches of the complex square root function in every simply connected domain not containing the origin (see e.g. Bak and Newman [2010] pages 114-115). Then, as the discriminant

$$\zeta = F_1^2 - 4F_0F_2 \quad (3.16)$$

is clearly a smooth function of α and the parameters, there are two continuous branches of the increment γ (3.7) as functions of α and the parameters, and correspondingly two continuous branches of the growth rate γ_R . If $\text{Ma} \downarrow 0$ then $\gamma_1\gamma_2 = F_0/F_2 \downarrow 0$ and $\gamma_1 + \gamma_2 = -F_2/F_1 \not\rightarrow 0$ and so either $\gamma_1 \downarrow 0$ or $\gamma_2 \downarrow 0$. We call the increment branch that is non-zero at $\text{Ma} = 0$ the ‘‘robust branch,’’ and the other one, that vanishes as $\text{Ma} \downarrow 0$, is named the ‘‘surfactant branch’’. Correspondingly, these are the continuous robust and surfactant branches of the growth rate. In certain cases, such as the one considered in section 4.3.1 with $m = 1$, it can be shown that the discriminant ζ never takes the zero value and the range of the function $\zeta(\alpha; s, m, n, \text{Ma}, \text{Bo})$ is a simply connected domain in the complex ζ -plane. Then, there are two branches of the growth rate which are continuous functions of $(\alpha; s, m, n, \text{Ma}, \text{Bo})$.

However, as will be seen below, the discriminant (3.16) may become zero for some parameter values. This happens when $\text{Re}(\zeta) = 0$ and $\text{Im}(\zeta) = 0$. These two equations define a manifold of co-dimension two in the $(\alpha; s, m, n, \text{Ma}, \text{Bo})$ space that is analogous to a branch point in the complex plane; and if we draw the line of increasing α from each point of this manifold, that is a ray parallel to the α -axis, with all the parameter values fixed, we obtain the ‘‘branch cut’’ hypersurface. The growth rates are not defined on this branch cut, and there is a jump in the growth rate when crossing from one side of the branch cut to the other. Still, each of the two growth-rate branches is defined and continuous almost everywhere in the α -parameter space (with the branch cut hypersurface excluded from it), and the growth-rate branches defined this way are smooth in α . The surfactant branch of the growth rate is again defined as the one which vanishes as $\text{Ma} \downarrow 0$. These considerations are given in more detail in appendix A. It will be seen below, as for example in figure 9, that the discriminant equal to zero corresponds to the reconnection point of the two growth rate branches, when the crossing dispersion curves of the two branches become non-crossing at a certain value of a changing parameter. There is a jump discontinuity of the growth rate in the changing parameter at its reconnection-point value, for all α exceeding the reconnection-point value of α . Except for such reconnection situations, all the dispersion curves are smooth at all α .

Typical dispersion curves of stable and unstable cases look like those in figure 2. The unstable branch starts at $\alpha = 0$ and $\gamma_R = 0$, grows with α , attains a maximum value $\gamma_{R\text{max}}$ at some $\alpha = \alpha_{\text{max}}$, then decreases and crosses the α -axis so that $\gamma_R = 0$ at some non-zero wavenumber, α_0 , called the marginal wavenumber. The other, stable, branch also starts at $\alpha = 0$ and $\gamma_R = 0$ but then decreases with α . The values of $\alpha_0, \gamma_{R\text{max}}$, and α_{max} depend on the parameters n, m, s, Ma , and Bo .

Each solution $(\gamma; h, G)$ of the system (3.5) determines the normal-mode amplitudes (and thus the complete structure of the normal mode), since h and G determine the coefficients a_1, b_1 , and b_2 , and thus the vertical velocities \hat{w}_j via equations (3.2) and (3.3), then the horizontal velocities \hat{u}_j via equations (2.7) and the pressures \hat{f}_j via equations (2.14).

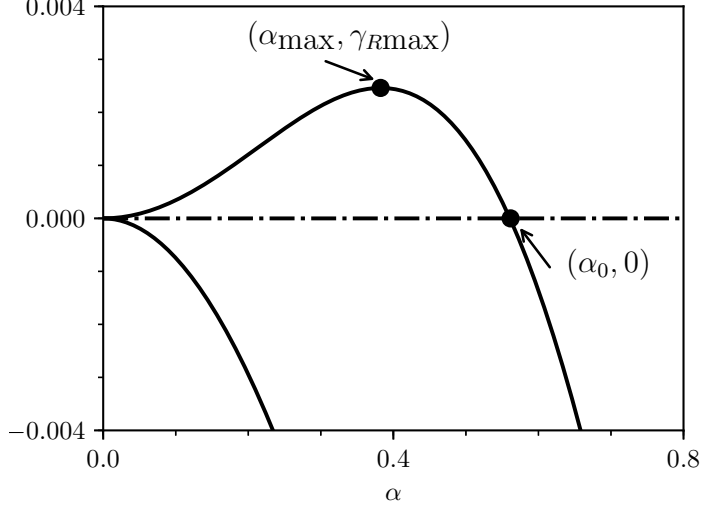


Figure 2: Typical dispersion curves of the two normal modes: (1) the unstable mode, which has a maximum growth rate $\gamma_R = \gamma_{R\max}$ at a wavenumber $\alpha = \alpha_{\max}$ and then decays, eventually becoming stable for $\alpha > \alpha_0$, and (2) the stable mode, which has negative growth rates for all wavenumbers.

It is pointed out in FH (i.e., for the case $\text{Bo} = 0$) that at least one of the modes for each given α is stable. This result holds for $\text{Bo} \geq 0$ as well, which is seen as follows. (However, we will see that for $\text{Bo} < 0$ both modes are unstable sometimes.) Let the two solutions of (3.7) be $\gamma_1 = \gamma_{1R} + i\gamma_{1I}$ and $\gamma_2 = \gamma_{2R} + i\gamma_{2I}$. Then the real parts of the solutions satisfy $\gamma_{1R} + \gamma_{2R} = -\text{Re}(F_1)/F_2 < 0$. The latter inequality holds because, as was discussed before, $\text{Re}(F_1) > 0$ when $\text{Bo} \geq 0$. So, if one of the quantities γ_{jR} is positive (corresponding to an unstable mode), then the other must be negative, thus giving a stable mode.

In order to compute the maximum growth rate, $\gamma_{R\max}$, the wavenumber corresponding to the maximum growth rate, α_{\max} , and the marginal wavenumber, α_0 , it is convenient to split the dispersion equation (3.6) into its real and imaginary parts,

$$F_2\gamma_R^2 - F_2\gamma_I^2 + \text{Re}(F_1)\gamma_R - \text{Im}(F_1)\gamma_I + \text{Re}(F_0) = 0, \quad (3.17)$$

$$2F_2\gamma_R\gamma_I + \text{Re}(F_1)\gamma_I + \text{Im}(F_1)\gamma_R + \text{Im}(F_0) = 0. \quad (3.18)$$

The imaginary part of the growth rate γ_I is expressed in terms of γ_R using equation (3.18) (assuming $\text{Re}(F_1) \neq 0$) and then substituted it into (3.17) to obtain the following quartic equation for γ_R ,

$$\begin{aligned} & 4F_2^3\gamma_R^4 + 8F_2^2\text{Re}(F_1)\gamma_R^3 + F_2[4F_2\text{Re}(F_0) + \text{Im}(F_1)^2 + 5\text{Re}(F_1)^2]\gamma_R^2 \\ & + \text{Re}(F_1)[\text{Re}(F_1)^2 + 4F_2\text{Re}(F_0) + \text{Im}(F_1)^2]\gamma_R - F_2\text{Im}(F_0)^2 \\ & + \text{Re}(F_1)^2\text{Re}(F_0) + \text{Re}(F_1)\text{Im}(F_1)\text{Im}(F_0) = 0. \end{aligned} \quad (3.19)$$

Since $\gamma_R = 0$ at the marginal wavenumber, α_0 , equation (3.19) becomes

$$-F_2\text{Im}(F_0)^2 + \text{Re}(F_1)\text{Im}(F_1)\text{Im}(F_0) + \text{Re}(F_1)^2\text{Re}(F_0) = 0, \quad (3.20)$$

the marginal wavenumber equation. This equation (3.20) is a polynomial in Ma and Bo

$$k_{20}\text{Ma}^2 + k_{11}\text{Ma}B + k_{31}\text{Ma}^3B + k_{22}\text{Ma}^2B^2 + k_{13}\text{Ma}B^3 = 0 \quad (3.21)$$

where $B := \text{Bo} + \alpha^2$ and the coefficients k_{ij} are given in appendix B. For $\text{Ma} = 0$, it transpires that these marginal wavenumber equations are not valid. However, then the coefficient F_0 of the quadratic equation (3.6) vanishes, and there remains just one mode corresponding to the Rayleigh-Taylor instability whose

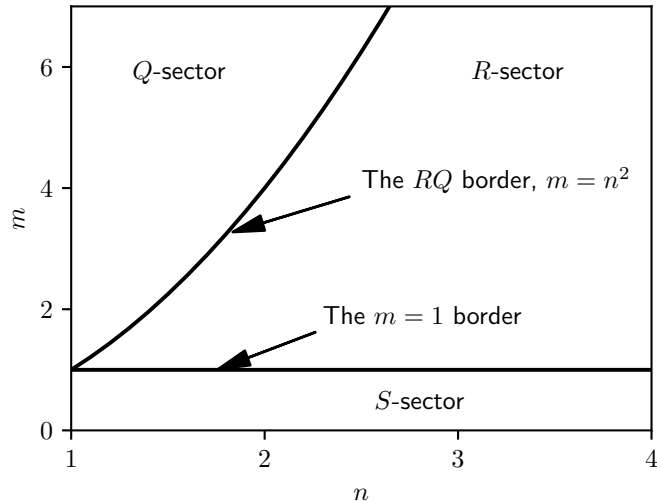


Figure 3: Partition of the (n, m) -plane of the system, $n \geq 1$ and $m > 0$, into three sectors (Q , R , and S) and their borders corresponding to differences in stability properties of the flow.

increment $\gamma = -F_1/F_2$. For the marginal wavenumber, it follows that $\text{Re}(F_1) = 0$, which implies that $\alpha_0 = (-\text{Bo})^{1/2}$. This corresponds to capillary forces balancing the destabilizing gravitational forces provided $\text{Bo} < 0$.

The wavenumber α_{max} corresponding to the maximum growth rate $\gamma_{R \text{max}}$ is obtained by simultaneously solving (3.19) and the equation obtained by differentiating (3.19) with respect to α , taking into account that $d\gamma_R/d\alpha = 0$ at the maximum. The latter equation is written as

$$\gamma_R^4 \frac{d}{d\alpha} C_4(\alpha) + \gamma_R^3 \frac{d}{d\alpha} C_3(\alpha) + \gamma_R^2 \frac{d}{d\alpha} C_2(\alpha) + \gamma_R \frac{d}{d\alpha} C_1(\alpha) + \frac{d}{d\alpha} C_0(\alpha) = 0, \quad (3.22)$$

where C_j denotes the coefficient of the γ_R^j term that appears in equation (3.19). (For example, $C_4 = 4F_2^3$.)

4 Long-wave approximation

As was mentioned earlier, from the long-wave approximation by FH ($\text{Bo} = 0$), three sectors in the (n, m) -plane were identified that characterize the stability of the flow for $n \geq 1$. Based on the long-wave results of FH17, the same three sectors are found to be relevant in the presence of gravity effects: the Q sector ($m > n^2$), the R sector ($1 < m < n^2$), and the S sector ($0 < m < 1$). Figure 3 shows the three sectors and their borders. Stability properties of the robust and surfactant branches can change significantly from sector to sector, and can be special on borders as well.

4.1 General asymptotics for the three sectors

4.1.1 Increments and growth rates

While it is straightforward to use equation (3.7) to evaluate and graph growth rates, the limit of long waves yields some simpler asymptotic expressions. The general growth rate (and the increment) expressions in the three sectors are given in this subsection, but additional results in each sector will be discussed in later sections. First, the coefficients F_2 , F_1 , and F_0 (3.9)-(3.14) in the dispersion equation (3.6) are expanded in a Taylor series about $\alpha = 0$. The leading order terms are given in Appendix C. Unless $s = 0$ and $\text{Bo} \neq 0$, we have $|F_1^2| \gg |F_2 F_0|$, provided $\alpha \ll s$, since if $s \neq 0$, then $|F_1^2| \approx \text{Re}(F_1^2) \sim \alpha^2$ and $|F_2 F_0| \approx \text{Im}(F_2 F_0) \sim \alpha^3$; and if $s = 0$ and $\text{Bo} = 0$ then $|F_1^2| \sim \alpha^4$ and $|F_2 F_0| \sim \alpha^6$ (see Appendix C). Therefore, keeping the four

leading members in the series for the second term of equation (3.7), the two increments are

$$\gamma \approx \frac{1}{2F_2} \left(-F_1 \pm F_1 \left[1 + \frac{1}{2} \left(-\frac{4F_2F_0}{F_1^2} \right) - \frac{1}{8} \left(-\frac{4F_2F_0}{F_1^2} \right)^2 + \frac{1}{16} \left(-\frac{4F_2F_0}{F_1^2} \right)^3 \right] \right), \quad (4.1)$$

or, keeping the terms necessary to obtain the growth rate γ_R to the leading order,

$$\gamma \approx -\frac{F_1}{F_2} + \frac{F_0}{F_1} + \frac{F_0^2 F_2}{F_1^3} \quad (4.2)$$

and

$$\gamma \approx -\frac{F_0}{F_1} - \frac{F_2 F_0^2}{F_1^3} - 2 \frac{F_0^3 F_2^2}{F_1^5}. \quad (4.3)$$

For $s \neq 0$ the growth rates for the robust (4.2) and surfactant (4.3) branches are found to be, respectively,

$$\gamma_R \approx \left(\frac{\varphi(m-n^2)}{4(1-m)\psi} \text{Ma} - \frac{n^3(n+m)}{3\psi} \text{Bo} \right) \alpha^2 \quad (4.4)$$

and

$$\gamma_R \approx \frac{(n-1)\text{Ma}}{4(1-m)} \alpha^2 + k_S \alpha^4, \quad (4.5)$$

where

$$\varphi = n^3 + 3n^2 + 3mn + m \quad (4.6)$$

and

$$\psi = n^4 + 4mn^3 + 6mn^2 + 4mn + m^2. \quad (4.7)$$

We include the term with k_S in equation (4.5) because the coefficient of the α^2 term vanishes when $n = 1$. The expression for k_S is given in appendix B, see equation (B.17). For the case $s = 0$ and $\text{Bo} = 0$, the growth rates for the robust (4.2) and surfactant (4.3) branches are found to be

$$\gamma_R \approx -\frac{n^3}{12(m+n^3)} \alpha^4$$

and

$$\gamma_R \approx -\frac{n(m+n^3)\text{Ma}}{\psi} \alpha^2$$

which is in agreement with FH.

Finally, for the case $s = 0$ and $\text{Bo} \neq 0$, we find that $|F_1^2| \sim \alpha^4 \sim |F_2 F_0|$. So, the expansion (4.1) is no longer valid. However, both modes are stable if $\text{Bo} > 0$, but there is instability if $\text{Bo} < 0$. Indeed, if $\text{Bo} < 0$ then $F_0 \approx \frac{1}{36} n^4 \alpha^4 \text{MaBo} < 0$ (see equation (C.4)). Therefore, the discriminant $F_1^2 - 4F_0 F_2 > F_1^2$. Then equation (3.7) yields one of the two growth rates to be positive, so we have instability. On the other hand, if $\text{Bo} > 0$, then $\text{Re}(F_1) > 0$ but the discriminant can be either positive or negative. If it is negative, then the square roots in equation (3.7) are purely imaginary and therefore both values of γ_R are negative. If the discriminant is positive, then $|\sqrt{F_1^2 - 4F_0 F_2}| < F_1$, so that both values of γ given by equation (3.7) are negative again. These leading-order results were obtained in a different way and discussed in more detail in Frenkel and Halpern [2016] and FH17.

4.1.2 Marginal wavenumbers and their small s asymptotics

When the marginal wavenumber determined by equation (3.20) happens to be small (typically, due to the smallness of some of the three parameters s , Bo , and Ma), it is approximated by substituting the long-wave expressions for the coefficients (C.1)-(C.5) into (3.20) provided $\text{Ma} \neq 0$. If $s \neq 0$ is fixed, then by keeping only the two leading terms in α^2 , we arrive at

$$\zeta_0 + \zeta_2 \alpha^2 = 0 \quad (4.8)$$

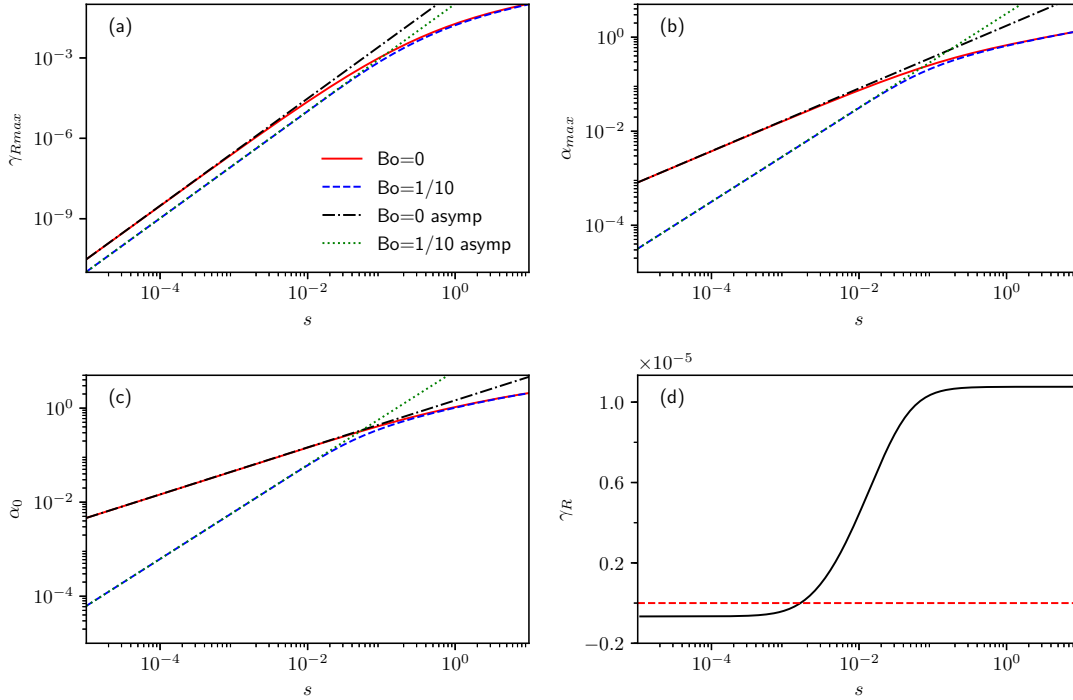


Figure 4: (a) $\gamma_{R\max}$, (b) α_{\max} , (c) α_0 , for $\text{Bo} = 0$ and $\text{Bo} = 0.1$, along with their small- s asymptotics, and (d) γ_R at $\alpha = 0.01$ and $\text{Bo} = 0.1$, vs s for $n = 2$ and $m = 2$ (which is in the R sector), with $\text{Ma} = 1$.

where ζ_0 and ζ_2 are polynomials in Ma and Bo given by equations (B.18) and (B.19). Therefore, at leading order,

$$\alpha_0 = \sqrt{-\zeta_0/\zeta_2}.$$

Clearly, for this result to be consistent, ζ_0/ζ_2 must be negative and small, which is the case for appropriate parameter values, such as, for example, those used in figures 4, 5, and 6. It is interesting to investigate the transition from instability to stability of the case $s = 0$ by considering the limit $s \downarrow 0$. In this we should distinguish two cases: $\text{Bo} = 0$ and $\text{Bo} \neq 0$. For $\text{Bo} \neq 0$, the marginal wavenumber is given by

$$\tilde{\zeta}_0 s^2 + \zeta_{20} \alpha^2 = 0 \quad (4.9)$$

instead of equation (4.8), where, by definition the coefficients $\tilde{\zeta}_0 = \zeta_0/s^2$ and $\zeta_{20} = \zeta_2(s=0)$ (see equations (B.18) and (B.19)). These coefficients are independent of s and α , and so, asymptotically α_0 is proportional to s , with the coefficient of proportionality $\sqrt{-\tilde{\zeta}_0/\zeta_{20}}$.

However, for $\text{Bo} = 0$, the coefficient of the α^2 term in equation (4.9) vanishes, and, instead the leading order equation for the marginal wavenumber is found to be

$$\tilde{\zeta}_0 s^2 + \zeta_{40} \alpha^4 = 0,$$

where $\zeta_{40} = \frac{1}{324} n^2 (m + n^3)^2 \text{Ma}^2$. Then the marginal wavenumber is asymptotically $\alpha_0 = (-\tilde{\zeta}_0/\zeta_{40})^{1/4} s^{1/2}$. Panel (c) of figure 4 shows these asymptotes along with the marginal wavenumbers obtained by solving equation (3.21) for $\text{Bo}=0$ and some positive values of Bo in the R sector. Panel (d) shows, for a fixed wavenumber, $\alpha = 0.01$, how the instability at the larger s corresponding to the (positive) growth rate (4.4), changes to stability with the growth rate corresponding, in the leading order, to the case of $s = 0$ and nonzero Bo . The growth rate that crosses the zero value at the s for which $\alpha = 0.01$ is the marginal wavenumber.

In the analogous figure for the Q sector, figure 5, the marginal wavenumber is the left endpoint of the interval of the unstable wavenumbers, which is bounded away from the zero of the wavenumber axis. There

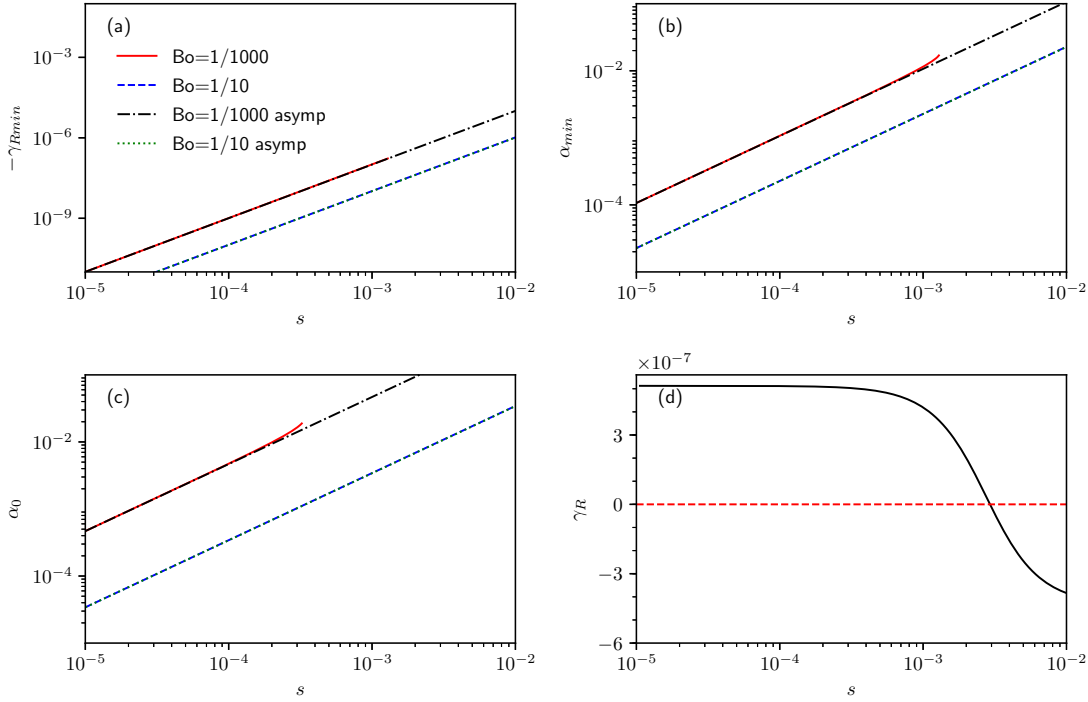


Figure 5: (a) γ_{Rmin} , (b) α_{min} , (c) α_0 , for $Bo = -0.001$ and $Bo = -0.1$, along with their small- s asymptotics, and (d) γ_R at $\alpha = 0.01$ and $Bo = -0.1$, vs s for $n = 2$ and $m = 5$ (which is in the Q sector), with $Ma = 1$.

is a band of stable wavenumbers between this marginal wavenumber and the zero, and inside it there is a minimum of the growth rate, γ_{Rmin} , at the corresponding wavenumber α_{min} ; their dependencies on s are plotted in panels (a) and (b), respectively. Correspondingly, panel (d) shows stability at the larger s , and instability at the smaller s , since here, in the Q sector, it is the band of *stable* wavenumbers that shrinks toward zero as $s \downarrow 0$. We call such cases, in which there is an interval of unstable wavenumbers bounded away from zero, the mid-wave instability, to distinguish them from the long-wave instability, in which the interval of unstable wavenumbers is bordered by zero. We study the mid-wave instability in detail below (see sections 5 and 6). By considering the formula for ζ_2 (B.19) for sufficiently small Ma and Bo , we see that all the terms are negligible as compared to the last one (the capillary term), and equation (4.9), after being multiplied by an appropriate factor, is interpreted as the instability term (4.4) being balanced by the capillary effect (corresponding to the term α^2 in $B = Bo + \alpha^2$, and arising from the second term of equation (4.9).) The resulting, asymptotically s -independent, value of the marginal wavenumber, as one can see at the larger s in figure 6, is still small, consistent with the long-wave approximation. However, for the same fixed small values of Ma and Bo , at sufficiently small s , the last, capillary, term in ζ_{20} is negligible, and the stabilization near the marginal wavenumber is due to non-capillary effects of the combined action of surfactants and gravity. It is clear that the three corresponding terms in ζ_{20} are not zero only if both the Marangoni and Bond numbers are non-zero. These (non-additively) combined surfactant-gravity effects are beyond the lubrication approximation, and can be captured only by the post-lubrication correction theory considered in Frenkel and Halpern [2016]. Figure 6 shows the numerical solution of the marginal-wavenumber equation (3.20) without using the long-wave asymptotics, along with the larger- s (capillary) and small- s (gravity- and surfactant-determined, non-lubrication) approximations of the wavenumber given by the long-wave asymptotic equation (4.9). Excellent agreement is evident.

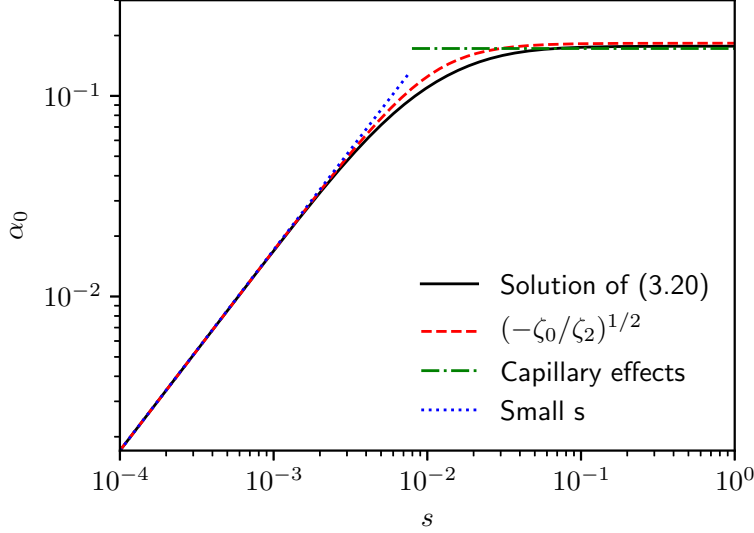


Figure 6: Marginal wavenumber α_0 vs the shear parameter s , along with its asymptotics, at larger s , due to the capillary effects, and at smaller s , due to the combined gravity-surfactant effects, for $n = 2$, $m = 2$, $\text{Ma} = 0.05$, and $\text{Bo} = -0.05$.

4.1.3 Maximum growth rates

As indicated earlier, a way to find $\gamma_{R\text{max}}$ and α_{max} is to solve equations (3.19) and (3.22). For $s \downarrow 0$, numerical computations suggest that $\alpha_{\text{max}} \propto s$ if $\text{Bo} \neq 0$ (just like α_0) and $\alpha_{\text{max}} \propto s^{2/3}$ if $\text{Bo} = 0$, and that $\gamma_{R\text{max}} \propto s^2$ for both $\text{Bo} \neq 0$ and $\text{Bo} = 0$, as one can see in figure 4. We find the coefficients of these asymptotic dependencies as follows:

For the case $\text{Bo} = 0$, we write $\gamma_{R\text{max}}$ and s^2 as functions of α_{max} to the two leading orders,

$$s^2 \approx \phi_1 \alpha^3 + \phi_2 \alpha^4, \quad \gamma_{R\text{max}} \approx \psi_1 \alpha^3 + \psi_2 \alpha^4, \quad (4.10)$$

with indeterminate coefficients ϕ_1 , ϕ_2 , ψ_1 and ψ_2 . We have to use two leading orders because the leading order system for ϕ_1 and ψ_1 turns out to be degenerate, and only gives one relation between ϕ_1 and ψ_1 . The other relation between ϕ_1 and ψ_1 is found as the solvability condition for the next order non-homogeneous system for ϕ_2 and ψ_2 . The leading order of equation (3.19) consists of terms that are proportional to α^9 . Therefore, the terms which are nonlinear in γ_R are discarded. This yields

$$(d\alpha^6)\psi_1\alpha^3 + (f\alpha^6)\phi_1\alpha^3 = 0, \quad (4.11)$$

where $d = \langle \text{Re}(F_1) \rangle^3$ and $f = \langle \text{Re}(F_1) \rangle \langle \text{Im}(F_1) \rangle \langle \text{Im}(F_0) \rangle - F_2 \langle \text{Im}(F_0) \rangle^2$. Here the bracketed quantities are the coefficients of powers of s and α in the leading order terms of the corresponding “unbracketed” coefficients (A24)-(A28): $\langle \text{Re}(F_1) \rangle = \frac{1}{3}n(m+n^3)\text{Ma}$, $\langle \text{Im}(F_1) \rangle = \frac{2}{3}n^2(n+1)(1-m)$, $\langle \text{Re}(F_0) \rangle = \frac{1}{36}n^4\text{Ma}$, and $\langle \text{Im}(F_0) \rangle = \frac{1}{6}n^2(1-n^2)\text{Ma}$. When obtaining equation (3.22) by differentiating with respect to α at constant γ_R and s^2 , only the powers of α inside the parentheses of equation (4.10) are differentiated, and this yields

$$(6d\alpha^5)\psi_1\alpha^3 + (6f\alpha^5)\phi_1\alpha^3 = 0.$$

So, the matrix of the coefficients of the linear homogeneous system for ϕ_1 and ψ_1

$$M = \begin{bmatrix} f & d \\ 6f & 6d \end{bmatrix}$$

is singular, and the leading-order system yields the single relation

$$\phi_1 = -\frac{d}{f}\psi_1. \quad (4.12)$$

Therefore, we need to consider the next order of equation (3.19), proportional to α^{10} . We obtain

$$\begin{aligned} (d\alpha^6)\psi_2\alpha^4 + (f\alpha^6)\phi_2\alpha^4 &= -5(F_2 < \text{Re}(F_1) >^2 \alpha^4)\psi_1^2\alpha^6 \\ &\quad - (< \text{Re}(F_1) > < \text{Im}(F_1) >^2 \alpha^4)\psi_1\alpha^3\phi_1\alpha^3 \\ &\quad - (< \text{Re}(F_1) >^2 < \text{Re}(F_0) >)\alpha^{10}. \end{aligned} \quad (4.13)$$

Differentiating the quantities inside the parentheses with respect to α , the second equation for ϕ_2 and ψ_2 is

$$\begin{aligned} (6d\alpha^5)\psi_2\alpha^4 + (6f\alpha^5)\phi_2\alpha^4 &= -5(4F_2 < \text{Re}(F_1) >^2 \alpha^3)\psi_1^2\alpha^6 \\ &\quad - (4 < \text{Re}(F_1) > < \text{Im}(F_1) >^2 \alpha^3)\psi_1\alpha^3\phi_1\alpha^3 \\ &\quad - 10(< \text{Re}(F_1) >^2 < \text{Re}(F_0) >)\alpha^9. \end{aligned} \quad (4.14)$$

Equations (4.13) and (4.14) form a nonhomogeneous linear system for $[\phi_2, \psi_2]$ with the same matrix M . The condition for the solution $[\phi_2, \psi_2]$ to exist requires that the right hand of the second equation is six times that of the first equation, which yields after eliminating ϕ_1 by equation (4.12) the following equation for ψ_1

$$(5F_2f - < \text{Re}(F_1) >^2 < \text{Im}(F_1) >^2)\psi_1^2 = 2f < \text{Re}(F_0) >.$$

This determines ψ_1 , and then from equation (4.12), ϕ_1 , namely,

$$\phi_1 = \left[\frac{8n^2(m+n^3)^6}{3(n-1)(n+1)^4(n^2-m)\phi(16(m-1)^2(m+n^3)^2 + 5(n-1)(n^2-m)\phi\psi)} \right]^{1/2} \text{Ma}^{3/2}$$

and

$$\psi_1 = \left[\frac{n^4(n-1)(n^2-m)\phi}{6(16n^2(m-1)^2(m+n^3)^2 + 5(n-1)(n^2-m)\phi\psi)} \right]^{1/2} \text{Ma}^{1/2}.$$

Returning to the independent variable s , the asymptotics

$$\gamma_{R\max} = \frac{\psi_1}{\phi_1}s^2, \quad \alpha_{\max} = \phi_1s^{2/3}$$

are shown in figure 4 along with the full dependencies for a representative set of the parameter values.

For the case $\text{Bo} \neq 0$, it is sufficient to consider only the leading order of equations (3.19) and (3.22) (proportional correspondingly to α^8 and α^7) to determine the coefficients c_1 and d_1 in the asymptotics $s^2 = c_1\alpha^2$ and $\gamma_{R\max} = d_1\alpha^2$. Since there are contributions from the terms of equations (3.19) and (3.22) with all powers of $\gamma_{R\max}$, the resulting system of two quartic equations for c_1 and d_1 can only be solved numerically. The small- s asymptotics,

$$\gamma_{R\max} = \frac{d_1}{c_1}s^2, \quad \alpha_{\max} = c_1^{-1/2}s$$

are shown in figure 4 along with the full numerics.

We see that the cases $\text{Bo} = 0$ and $\text{Bo} \neq 0$ have different powers of s in the asymptotics for α_0 , and the same is true for α_{\max} . Figure 4(c) shows that as $\text{Bo} \downarrow 0$, the interval of small s for which $\alpha_0 \propto s$ shrinks, and there is a crossover to the $s^{1/2}$ behavior characteristic of $\text{Bo} = 0$ for an interval of larger (but still small) wavenumbers. Similarly, for α_{\max} there is a crossover from $\alpha_{\max} \propto s$ at the smallest s to the $s^{2/3}$ asymptotic characteristic of $\text{Bo} = 0$ for an interval of larger wavenumbers.

These considerations clarify the transition from the instability at $s \neq 0$ to stability at $s = 0$, and the relation between the different powers in the α_0 and α_{\max} asymptotics of the $\text{Bo} \neq 0$ and $\text{Bo} = 0$ cases.

4.2 Instability thresholds in the different sectors and nearby asymptotic behavior

In both the R sector ($1 < m < n^2$) and the Q sector, ($m > n^2$), the surfactant branch (4.5) is stable for all Bo and the robust branch (4.4) is unstable if $\text{Bo} < \text{Bo}_{cL}$, where, in view of equation (4.4), the threshold value is

$$\text{Bo}_{cL} = \frac{3\varphi(m-n^2)}{4n^3(1-m)(n+m)}\text{Ma}. \quad (4.15)$$

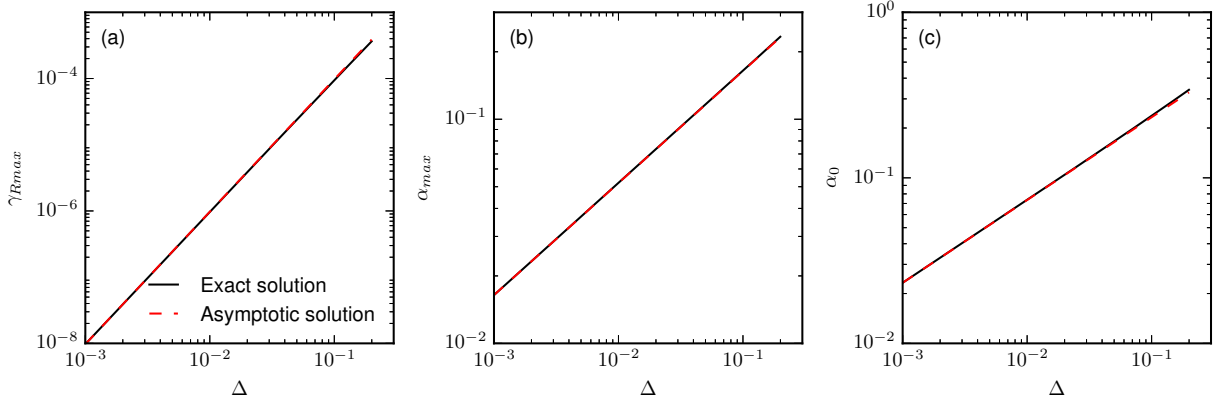


Figure 7: $\gamma_{R\max}$, α_{\max} and α_0 vs Δ for the same n , m and Ma as in figure 4, and $s = 1$. The solid lines represent the full solutions, equation (3.21), and the dashed lines represent the asymptotics given by (4.17).

In the R sector, the Marangoni effect is destabilizing, so $\text{Bo}_{cL} > 0$; gravity renders the flow stable for $\text{Bo} > \text{Bo}_{cL}$, whereas for $\text{Bo} < \text{Bo}_{cL}$, the flow is unstable. In the Q sector (and in the S sector as well), the Marangoni effect is stabilizing, $\text{Bo}_{cL} < 0$, and the gravity effect renders the robust branch unstable when the (negative, destabilizing) $\text{Bo} < \text{Bo}_{cL}$.

From equation (4.15) the ratio Bo_{cL}/Ma is a function of m and n only, and its graph is a surface in the $(n, m, \text{Bo}_{cL}/\text{Ma})$ -space. This surface is plotted in figure 3 of Frenkel and Halpern [2016], and is discussed in detail there. The window of unstable wavenumbers, $0 < \alpha < \alpha_0$, shrinks to zero as $\text{Bo} \uparrow \text{Bo}_{cL}$, so that the marginal wavenumber $\alpha_0 \downarrow 0$ for both the R and Q sectors. To obtain the asymptotic approximation for α_0 , we write the Bond number as

$$\text{Bo} = \text{Bo}_{cL} - \Delta \quad (4.16)$$

with $\Delta \downarrow 0$. Equation (3.9) is substituted into (4.8) and when retaining the leading order terms in Δ and α^2 we find that ζ_0 is proportional to Δ and ζ_2 is a cubic polynomial in Bo_{cL} (and is independent of Δ , to the leading order). The solution is

$$\alpha_0 \approx \left[1 + \beta_1 \text{Bo}_{cL} + \beta_3 \text{Bo}_{cL}^3 \right]^{-1/2} \Delta^{1/2} \quad (4.17)$$

where the coefficients β_1 and β_3 are given by equations (B.21) and (B.22) in appendix B. Note here that Ma has been written in terms of Bo_{cL} using equation (4.15). If $\text{Bo}_{cL} \ll 1$ (i.e., $\text{Ma} \ll 1$) equation (4.17) simplifies to

$$\alpha_0 \approx \Delta^{1/2}. \quad (4.18)$$

We also find in the way described above the long-wave asymptotic dependences

$$\alpha_{\max} \propto \Delta^{1/2} \text{ and } \gamma_{R\max} \propto \Delta^2.$$

For example, the relative error of the asymptotic expression (4.18) for $n = m = 2$, $s = 1$, $\text{Bo} = 10^{-6}$, and $\text{Ma} = 10^{-6}$ to $\text{Ma} = 10$ is less than 10% for $\Delta < 0.2$. This is illustrated in figure 7, where $n = m = 2$, $s = 1$ and $\text{Ma} = 1$. The asymptotics for $\gamma_{R\max}$, α_{\max} and α_0 near $\text{Bo} = \text{Bo}_c$ are practically indistinguishable from the full numerical solutions. In the S sector ($1 < n < \infty$ and $0 < m < 1$), the robust branch (4.4) is stable when $\text{Bo} > \text{Bo}_{cL}$, the latter given by (4.15), and unstable otherwise. However, equation (4.5) for the surfactant branch does not contain the Bond number, and indicates instability. Thus the surfactant mode is unstable for any Bo provided α is sufficiently small. However, it is easy to see that the window of unstable wavenumbers shrinks to zero as $\text{Bo} \uparrow \infty$. Indeed in this limit, equation (4.8) reduces to

$$s^2(n-1)(n+1)^2(m-1) + 36n^3(n+m)\alpha^2\text{Bo}^2 = 0. \quad (4.19)$$

Hence the asymptotic formula for the marginal wavenumber is

$$\alpha_0 \approx \left[\frac{36s^2(n+1)^2(1-m)(n-1)}{n^3(n+m)} \right]^{1/2} \text{Bo}^{-1}. \quad (4.20)$$

For the Q sector, the instability threshold (4.15) can be written in a different way: to state that (while the surfactant branch (4.5) is stable for all Bo and Ma), the robust branch is stable if Ma exceeds a critical Marangoni number, Ma_{cL} given by

$$\text{Ma}_{cL} = \frac{4n^3(1-m)(n+m)}{3\varphi(m-n^2)} \text{Bo}, \quad (4.21)$$

which is the reciprocal of (4.15).

When $\text{Ma} \uparrow \text{Ma}_{cL}$, the marginal wavenumber is expressed in terms of $\Delta_M = \text{Ma}_{cL} - \text{Ma}$. From equation (4.8), we obtain in the same way that we derived (4.17) for the marginal wavenumber in the R sector that

$$\alpha_0 \approx [M_0 + M_1 \text{Ma}_{cL} + M_3 \text{Ma}_{cL}^3]^{-1/2} \Delta_M^{1/2}. \quad (4.22)$$

where the coefficients M_0 , M_1 and M_3 are given by (B.23)-(B.25) in appendix B.

4.3 Instabilities on the (n, m) -sector borders

The borders $m = 1$, $m = n^2$, and $n = 1$ are considered separately because of singularities that can occur in the expressions for the growth rates and the marginal wavenumber derived in the previous sections for the R , S , and Q sectors.

4.3.1 The $m = 1$ border

Consider first the case $m = 1$ and $n \neq 1$. In the long-wave limit, $F_1^2 \ll |F_2 F_0|$ since $F_1^2 \sim \alpha^4$ and $|F_2 F_0| \sim \text{Ma} \alpha^3$ (the truncated Taylor series for such quantities are shown in Appendix C of Schweiger [2013]). Therefore, the roots to the dispersion equation (3.7), are approximated by

$$\gamma \approx \frac{1}{2F_2} \left(-F_1 + (4F_2 F_0)^{1/2} \left[1 + \frac{1}{2} \left(-\frac{F_1^2}{4F_2 F_0} \right) \right] \right). \quad (4.23)$$

Hence, the growth rates of the two branches are

$$\gamma_R = \frac{-\text{Re}(F_1) + \text{Re}(\sqrt{\zeta})}{2F_2} \quad (4.24)$$

where ζ is the discriminant of (3.7). To leading order in α , equation (4.24) reduces to

$$\gamma_R \approx \frac{\text{Re}(\sqrt{\zeta})}{2F_2} = \pm \frac{n[|n-1|(n+1)s\text{Ma}]^{1/2}}{2(n+1)^2} \alpha^{3/2}. \quad (4.25)$$

This result does not depend on the Bond number and is the same as in FH and HF. It turns out that the next order correction, omitted in the leading order expression, depends on both the Bond number and the Marangoni number, and is proportional to α^2 . Note also that (4.25) is valid as $\alpha \downarrow 0$ with the Marangoni number fixed but it is not valid as $\text{Ma} \downarrow 0$ with the wavenumber fixed. We will show below that for $m = 1$, the discriminant ζ in the expression for γ_R is never zero, and thus there are two branches of γ_R that are continuous at all parameter values and all α , which we called the surfactant branch and the robust branch. It is unclear from equation (4.25) whether the positive growth rate corresponds to the surfactant branch or the robust branch. Recall that, as $\text{Ma} \downarrow 0$, with α remaining finite, the identity of each branch is clear since, by definition, the branch that vanishes in this limit is the surfactant branch. Starting from there, each branch can be traced to the asymptotic region of small α and finite Ma where equation (4.25) is valid and thus the branches will be identified there.

The fact that there are two continuous branches of $\gamma(\alpha, \text{Ma})$ (with the other parameters fixed and not shown explicitly) given by (3.7) is seen as follows. As was discussed previously, in section 3 (see also Appendix A), in any simply connected domain not containing 0 of the complex ζ -plane, there exist two distinct analytic branches of the square root function, $f(\zeta) = \zeta^{1/2}$. The $\sqrt{\zeta}$ in the expression for γ_R , is a composite function of (α, Ma) through $\zeta(\alpha, \text{Ma})$. The discriminant ζ is a single-valued continuous function of (α, Ma) . It is easy to see that it maps the first quadrant of the (α, Ma) -plane inside the upper half-plane U of the ζ -plane, which is a simply connected domain not containing 0. Indeed, when $m = 1$ ($n \neq 1$ and $s \neq 0$), then from equation (3.12), $\text{Im}(F_1) = 0$, and hence

$$\text{Im}(\zeta) = -4F_2 \text{Im}(F_0). \quad (4.26)$$

In view of $n > 1$, we have $s_{\alpha n} > s_\alpha n$, and hence, from equation (3.14), $-\text{Im}(F_0) > 0$. Therefore, equation (4.26) yields $\text{Im}(\zeta) > 0$. Since the upper half-plane U of the ζ -plane is a simply connected domain not including 0, the square root function $\xi = f(\zeta) = \zeta^{1/2}$ in U of ζ has two analytic branches. One of them maps U onto the first quadrant of the ξ -plane, so that $\text{Re}(\sqrt{\zeta}) > 0$ for this branch, and thus $\text{Re}(\sqrt{\zeta})$ is a *positive* continuous function of (α, Ma) . The other analytic branch of $\xi = \zeta^{1/2}$ has its range entirely in the third quadrant of the ξ -plane, so that $\text{Re}(\sqrt{\zeta}) < 0$ and thus $\text{Re}(\sqrt{\zeta})$ is a *negative* continuous function of (α, Ma) . Thus, there is the one branch of $\text{Re}(\sqrt{\zeta})$ that is continuous and positive at all (α, Ma) and the other branch of $\text{Re}(\sqrt{\zeta})$ that is continuous and negative at all (α, Ma) . (We note that for even for arbitrary $m \neq 0$, it readily follows that $\text{Im}(\zeta) > 0$, provided that $\text{Ma} \downarrow 0$ and $\text{Bo} > 0$, since then, according to equations (3.11)-(3.14), $F_0 = 0$, $\text{Re}(F_1) > 0$ and $\text{Im}(F_1) > 0$.)

In the limit of $\text{Ma} \downarrow 0$, the surfactant branch vanishes, $\gamma_R = 0$, which from equation (4.24) means $\text{Re}(\sqrt{\zeta}) = \text{Re}(F_1)$. Therefore, $\text{sgn}(\text{Re}(\sqrt{\zeta})) = \text{sgn}(\text{Re}(F_1))$, where sgn is the sign function. It is sufficient to consider here only small wavenumbers, from an interval $[0, \alpha_s]$, by choosing an arbitrary α_s such that $\alpha_s \ll 1$ and $\alpha_s < |\text{Bo}|$. Then equation (C.2) (with $\text{Ma} = 0$) yields $\text{sgn}(\text{Re}(F_1)) = \text{sgn}(\text{Bo})$, so that $\text{sgn}(\text{Re}(\sqrt{\zeta})) = \text{sgn}(\text{Bo})$. As was already established, each branch of $\text{Re}(\sqrt{\zeta})$ has the same sign for all (α, Ma) . Therefore, for the surfactant branch, the relation $\text{sgn}(\text{Re}(\sqrt{\zeta})) = \text{sgn}(\text{Bo})$ holds in the limit of $\alpha \downarrow 0$ as well. From equation (4.25), $\text{sgn}(\gamma_R) = \text{sgn}(\text{Re}(\sqrt{\zeta}))$, and then for the surfactant branch, $\text{sgn}(\gamma_R) = \text{sgn}(\text{Bo})$. Thus, the surfactant branch is unstable for $\text{Bo} > 0$, $\gamma_R \propto +\alpha^{3/2}$ and stable for $\text{Bo} < 0$, $\gamma_R \propto -\alpha^{3/2}$. Consequently, the robust branch is stable (unstable) for $\text{Bo} > 0$ ($\text{Bo} < 0$). This answers the question of identifying the stable and unstable modes as belonging to the appropriate branches.

In certain limits it is possible to find a long-wave approximation to γ_R that captures the growth rate behavior close to the marginal wavenumber α_0 . Assuming $\text{Bo} \gg \text{Ma}$, $\alpha^2 \ll \text{Bo}$, and $\text{Ma}/\text{Bo}^2 \ll \alpha \ll 1$, equation (3.7) can be simplified to yield, for the unstable surfactant branch,

$$\gamma_R \approx \frac{27}{4} \frac{(n-1)^2 (n+1)^3 s^2 \text{Ma}^2}{n^5 \text{Bo}^3} - \frac{1}{4} \frac{n \text{Ma}}{(n+1)} \alpha^2 \quad (4.27)$$

which is valid for $\alpha \approx \alpha_0$. (Note that this equation is not valid in the limit as $\alpha \downarrow 0$; in the latter limit, the leading order behavior is still given by (4.25)). In figure 8 the growth rate of the surfactant branch is plotted using (3.7) along with the asymptotic expression (4.27). One can see the dashed line approximations approaches the full dispersion curve as $\alpha \uparrow \alpha_0$. The long-wave γ_R approximation (4.25) is not plotted in figure 8 but for the same parameter values the error is less than 1% when $\alpha < 1.4 \times 10^{-9}$.

An asymptotic expression for α_0 is obtained by solving for α equation (4.27) with $\gamma_R = 0$:

$$\alpha_0 \approx \frac{3s |n-1| (n+1)^2 [3\text{Ma}]^{1/2}}{n^3 \text{Bo}^{3/2}}. \quad (4.28)$$

The above expression is also obtained from the long-wave marginal wavenumber equation (4.8). This expression also suggests that gravity is not completely stabilizing since $\alpha_0 > 0$ at any positive finite value of Bo . We had the similar result that gravity, no matter how strong, cannot completely stabilize the Marangoni instability for the S sector.

4.3.2 The case $n = 1$

Next, we consider the border $n = 1$ with $m \neq 1$. Just like the $m = 1$ and $n \neq 1$ case, the imaginary part of the discriminant ζ , $\text{Im}(\zeta) = 2 \text{Re}(F_1) \text{Im}(F_1)$, is positive (or negative) for $m < 1$ (or $m > 1$), see (3.9)-(3.14).

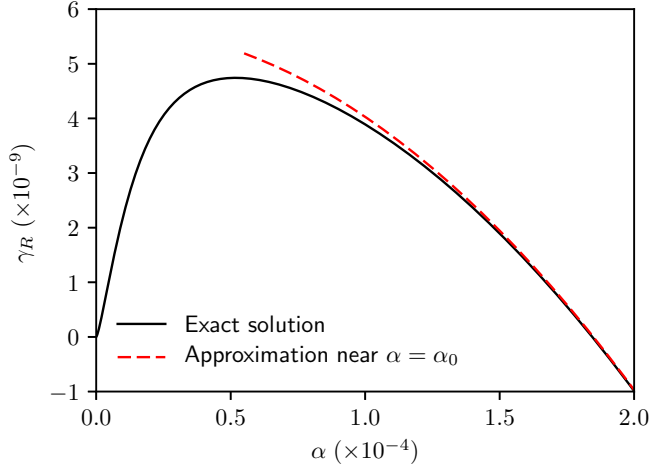


Figure 8: The exact dispersion curve (3.7) and the asymptotic expression of the growth rate around the marginal wavenumber (4.27) of γ_R for $m = 1$, $n = 2$, $s = 1$, $\text{Ma} = 1$, and $\text{Bo} = 1000$.

The growth rate for the robust mode is, from equation (4.4),

$$\gamma_R \approx -\frac{(1+m)}{m^2 + 14m + 1} \left\{ \text{Ma} + \frac{1}{3}\text{Bo} \right\} \alpha^2, \quad (4.29)$$

but, since the coefficient of the α^2 term in equation (4.5) becomes zero, we have for the surfactant branch, using equation (B.17) with $n = 1$,

$$\gamma_R \approx -\frac{1}{96} \frac{(1+m)}{s^2(m-1)^2} \left\{ \frac{1}{2}\text{Ma} + \frac{1}{3}\text{Bo} \right\} \text{Bo Ma} \alpha^4. \quad (4.30)$$

For this case the robust and surfactant branches are long-wave stable for $\text{Bo} > 0$. For $\text{Bo} < 0$ both branches are unstable if the magnitude of Bo is sufficiently large. This occurs when the leading term coefficients in (4.29) and (4.30) are positive, i.e. when $\text{Bo} < -3\text{Ma}$ for (4.29), and $-3\text{Ma}/2 < \text{Bo} < 0$ for (4.30).

4.3.3 The $m = n^2$ border

For the $m = n^2 \neq 1$ border, using the general equation (4.1) to obtain the growth rates to the leading orders, we find

$$\gamma_R \approx -\left\{ \frac{n\text{Bo}}{12(n+1)} \right\} \alpha^2 + \left\{ \frac{n(2\text{Ma} + n\text{Bo} - 5)}{60(n+1)} \right\} \alpha^4, \quad (4.31)$$

and

$$\gamma_R \approx -\left\{ \frac{\text{Ma}}{4(n+1)} \right\} \alpha^2. \quad (4.32)$$

We have kept two leading orders in equation (4.31) because the α^2 term vanishes for $\text{Bo} = 0$. Equation (4.32) shows that the surfactant branch is always stable, and this is consistent with HF in the limit $\text{Bo} \rightarrow 0$. Also, in this limit the robust branch, equation (4.31), reproduces the corresponding HF result, their equation (4.13). Also, for $\text{Bo} = 0$, equation (4.31) recovers the long-wave dispersion relation found in FH.

Finally, for the $m = 1$ and $n = 1$ case, the solutions to the dispersion equation (3.7) for arbitrary wavenumber are of the form

$$\gamma_R = \frac{-a\text{Ma} - b(\text{Bo} + \alpha^2) \pm [a\text{Ma} - b(\text{Bo} + \alpha^2)]}{2F_2\alpha^4}, \quad (4.33)$$

where

$$a = \alpha^2(s_\alpha^2 - \alpha^2)(c_\alpha s_\alpha + \alpha) \text{ and } b = (s_\alpha^2 - \alpha^2)(c_\alpha s_\alpha - \alpha).$$

After substituting F_2 , a , and b into (4.33), the growth rate for the robust branch is

$$\gamma_R = -\frac{(s_\alpha^2 - \alpha^2)(\text{Bo} + \alpha^2)}{4\alpha(c_\alpha s_\alpha + \alpha)} \approx -\frac{1}{24}(\text{Bo} + \alpha^2)\alpha^2 \text{ for } \alpha \ll 1,$$

and the growth rate for the surfactant branch is

$$\gamma_R = -\frac{\alpha(s_\alpha^2 - \alpha^2)\text{Ma}}{4(c_\alpha s_\alpha - \alpha)} \approx -\frac{1}{8}\text{Ma}\alpha^2 \text{ for } \alpha \ll 1.$$

Note that the surfactant branch is always stable but the robust branch is unstable if $\alpha^2 < -\text{Bo}$. Obviously, this only occurs if $\text{Bo} < 0$.

5 Arbitrary wavenumbers; mid-wave instability

In this section, results are given for arbitrary wavenumber, and comparisons are made across all parameter sectors. First, the influence of gravity on the maximum growth rate $\gamma_{R\max}$, the corresponding wavenumber α_{\max} and the marginal wavenumber α_0 in the R , S , and Q sectors are considered for fixed values of the Marangoni number. Then similar results are given to show the influence of surfactant for fixed values of the Bond number. Asymptotic results are also discussed.

5.1 Effects of gravity

We first examine the influence of Bo on the maximum growth rate $\gamma_{R\max}$, its corresponding wavenumber α_{\max} , and the marginal wavenumber α_0 . Figure 9 shows plots of γ_{\max} , α_{\max} and α_0 for a representative (n, m) pair from each of the three sectors where panels (a, d, g), (b, e, h) and (c, f, i) represent the R , S and Q sectors, respectively. In the R sector, panels (a, d, g) show that the system is unstable provided Bo does not exceed a finite positive value Bo_c and that $\gamma_{R\max}$, α_{\max} , and α_0 all decrease to zero as $\text{Bo} \downarrow \text{Bo}_c$. These findings were also observed in the long-wave limit (see section 4.2). This instability is of the long-wave type even when the marginal wavenumber α_0 is not small. However, for m sufficiently close to n^2 but still in the R sector, there appears a “mid-wave” instability (see figure 16 below), which is discussed below, in sections 5.3 and 6. Panels (b, e, h) show the surfactant branch is always unstable in the S sector. The discontinuity in the graph of α_{\max} in panel (e) is discussed below with figure 10. In the Q sector, surfactants are completely stabilizing provided $\text{Bo} > \text{Bo}_c$, as shown in panels (c), (f) and (i). Note that $\text{Bo}_c < 0$ agrees with the long-wave analysis (see equation (4.21)). The discontinuity that can occur in the S sector is displayed in figure 10. Panel (a) shows that for negligible Bo , one branch is long-wave unstable and the other one is stable. As the magnitude of Bo increases the previously stable branch becomes unstable ($\text{Bo} = -1$) and at some point the branches cross ($\text{Bo} = -1.5, -2.3$). Panel (e) shows that as $|\text{Bo}|$ continues to increase the crossing eventually disappears at which point the upper branch has two local extrema. At some value of Bo , the global maximum shifts from the right local extremum (as for $\text{Bo} = -2.45$) to the left local extremum (as for $\text{Bo} = -2.67$). Finally, as $\text{Bo} \downarrow -\infty$, both branches are unstable in the long-wave manner, and feature a single maximum.

5.2 Effects of surfactants in the R and S sectors

Here, we investigate, for a fixed value of Bo in the R and S sectors, the Marangoni number Ma dependences of the maximum growth rate γ_{\max} , the corresponding wavenumber α_{\max} , and the marginal wavenumber α_0 . The Q sector turns out to have somewhat different properties, which are discussed later (see figure 15). However, it is immediately clear that in the Q sector both branches are stable for $\text{Bo} > 0$ and fixed Ma (see panels (c), (f) and (i)) in figure 9.

Panels (a) and (b) of figure 11 show that $\gamma_{R\max}$ attains a maximum at some $\text{Ma} = O(1)$ in both the R and S sectors, and that $\gamma_{R\max} \downarrow 0$ as $\text{Ma} \uparrow \infty$. Both α_{\max} and α_0 also decrease to zero as $\text{Ma} \uparrow \infty$. However, in the R sector there is a threshold value of Ma , Ma_{cL} , below which the flow is stable; while in the S sector the flow is unstable for all $\text{Ma} > 0$. Recall from the long-wave results that $\text{Ma}_{cL}(\text{Bo})$ is the

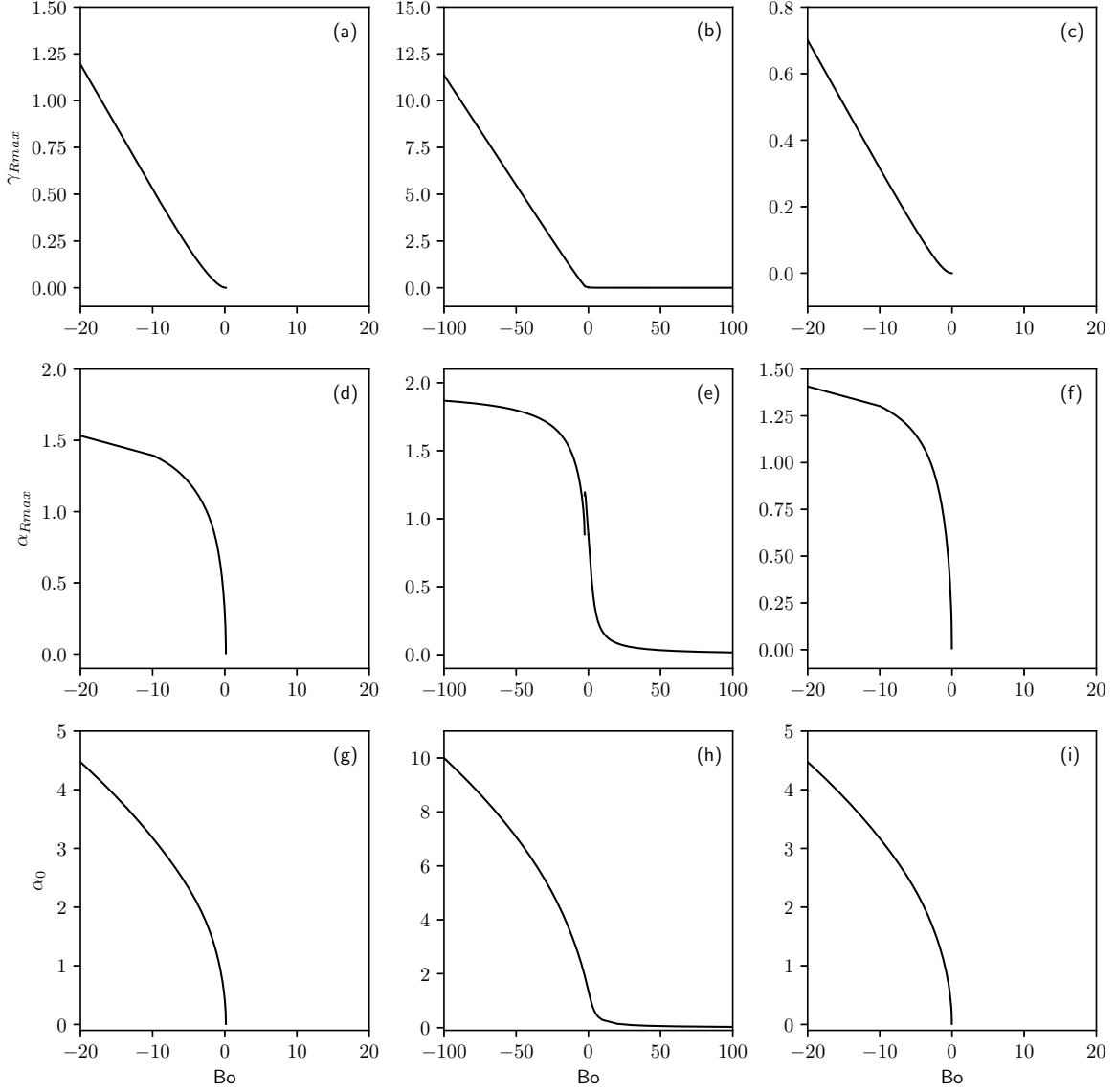


Figure 9: Dependence of the maximum growth rate $\gamma_{R\max}$, the corresponding wavenumber α_{\max} , and the marginal wavenumber α_0 on Bp in the R , S and Q sectors. Here $s = 1$, $Ma = 0.1$ and the values of the (n, m) pairs for the R (a,d,g), S (b,e,h), and Q (c,f,i) sectors are $(2, 2)$, $(2, 0.5)$, and $(2, 5)$, respectively.

inverse of $Bo_{cL}(Ma)$ (see equations (4.15) and (4.21)). In the S sector, α_{\max} and α_0 approach some non-zero constant values and $\gamma_{R\max} \downarrow 0$, showing no threshold value of Ma for complete stabilization of the flow.

The small and large Ma asymptotics of α_0 are discussed next. Panels (e) and (f) suggest that $\alpha_0 \downarrow 0$ as $Ma \uparrow \infty$. By substituting equations (B.12) - (B.16) into the marginal-wavenumber equation (3.21), and keeping only the dominant Ma terms, the following expression is obtained:

$$\frac{n^2}{324}(n^3 + m)^2 Bo Ma \alpha^2 + \frac{s^2}{108} \varphi(n-1)(n+1)^2(m - n^2) = 0, \quad (5.1)$$

from which

$$\alpha_0 \approx \frac{s(n+1)\sqrt{3\varphi(n-1)(n^2 - m)}}{n(n^3 + m)} Bo^{-1/2} Ma^{-1/2}. \quad (5.2)$$

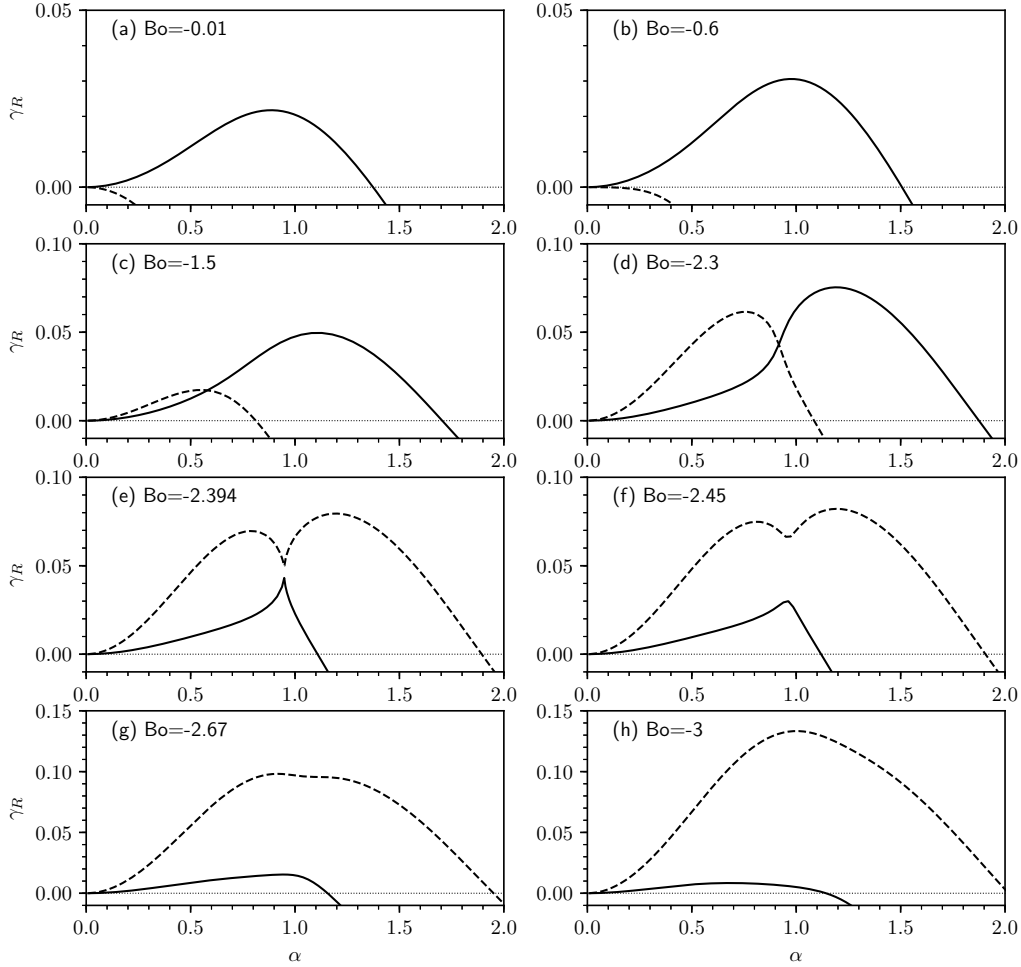


Figure 10: Dispersion curves given by (3.7) in the S sector ($n = 2$, $m = 0.5$) for selected values of Bo showing occurrence of two local maxima and a jump in the global maximum. Here $s = 1$ and $Ma = 0.1$.

This is consistent with the numerically-found behavior for α_0 at large Ma .

As $Ma \downarrow 0$, it is clear from panel (f) of figure 11 that in the S sector, α_0 approaches some finite non-zero value. Therefore, by keeping only the (dominant) linear Ma terms, equation (3.21) reduces to

$$k_{11} + k_{13}B^2 = 0, \quad (5.3)$$

where k_{11} and k_{13} depend on α , as given by equations (B.8) and (B.11). However, this equation must be solved numerically for α_0 since it is not necessarily small. Some other asymptotics for α_0 approaching zero in the R sector were discussed above in subsection 4.1.2. Panels (a), (b), (c) and (d) of figure 11 suggest that $\gamma_{R \max}$ and $\alpha_{\max} \downarrow 0$ as $Ma \uparrow \infty$. In the long-wave limit and for $Ma \gg 1$, the linear and constant terms of equation (3.19), whose coefficients are proportional to Ma^2 and Ma^3 , are dominant, giving rise to the

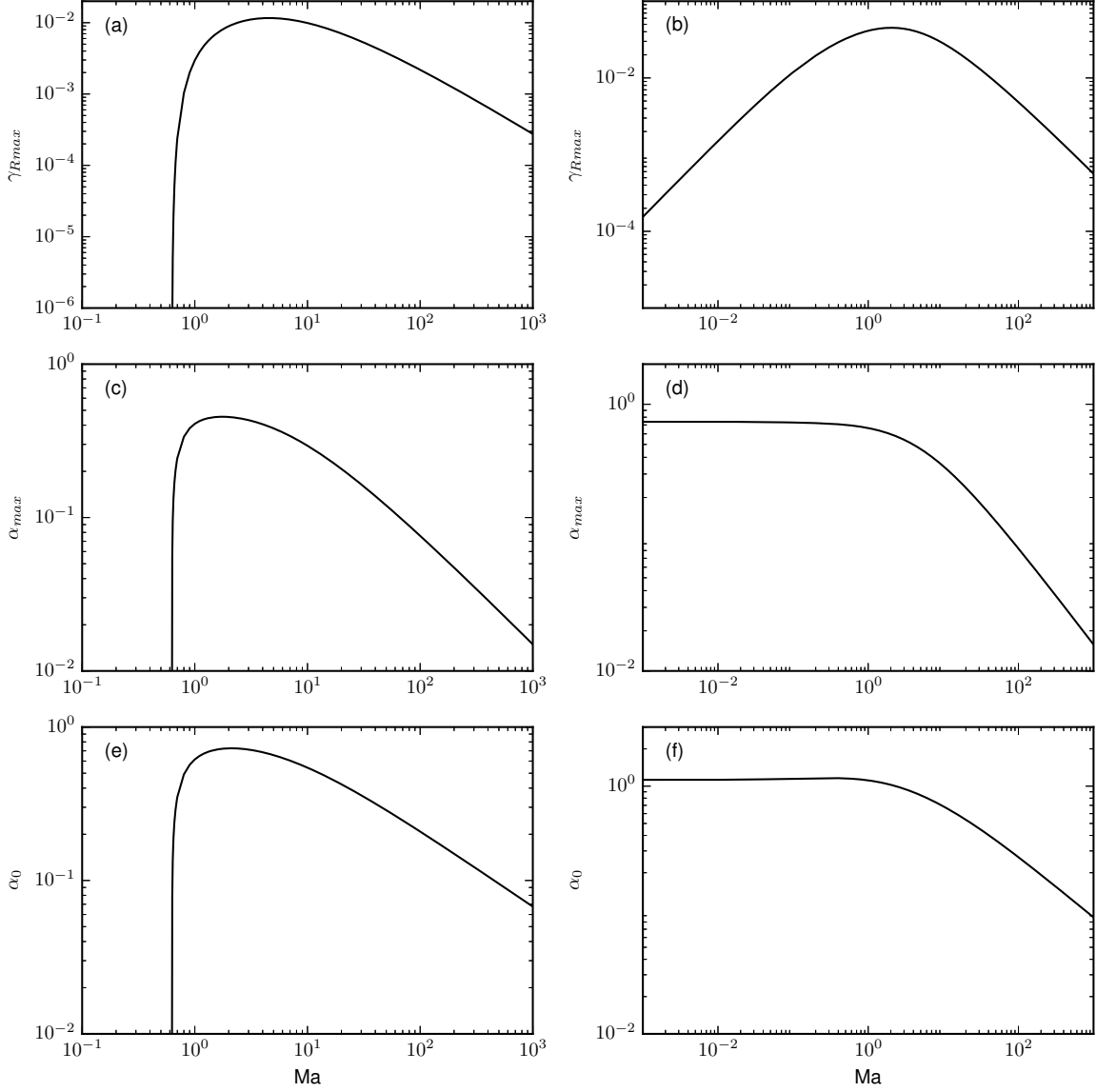


Figure 11: (a,b) $\gamma_{R\max}$, (c,d) α_{\max} and (e,f) α_0 vs Ma for $\text{Bo} = 1.0$ in the R sector (a,c,e) and S sector (b,d,f). Here $s = 1$ and the values of the (n, m) pairs in the R and S sectors are $(2, 2)$ and $(2, 0.5)$, respectively.

following simplified equation for γ_R :

$$\frac{1}{27}n^3(m+n^3)(n^2-m)\alpha^6\text{Ma}\gamma_R - \frac{1}{108}(n-1)n^4(n^2-m)s^2\varphi\alpha^6\text{Ma}^2 \approx 0. \quad (5.4)$$

The latter gives

$$\gamma_{R\max} \approx \frac{ns^2(n-1)(n+1)^2(m-n^2)\varphi}{4(n^3+m)^3}\text{Ma}^{-1}. \quad (5.5)$$

Because α^6 appears in the simplified equation above, it is convenient when solving for α_{\max} to subtract α times equation (3.22) from six times equation (3.19) and obtain

$$\frac{8}{27}(m-1)^2n^5(n+1)^2(n^3+m)s^2\alpha^4\text{Ma}\gamma_R - \frac{1}{162}n^6(n^3+m)^2\alpha^8\text{BoMa}^3 \approx 0. \quad (5.6)$$

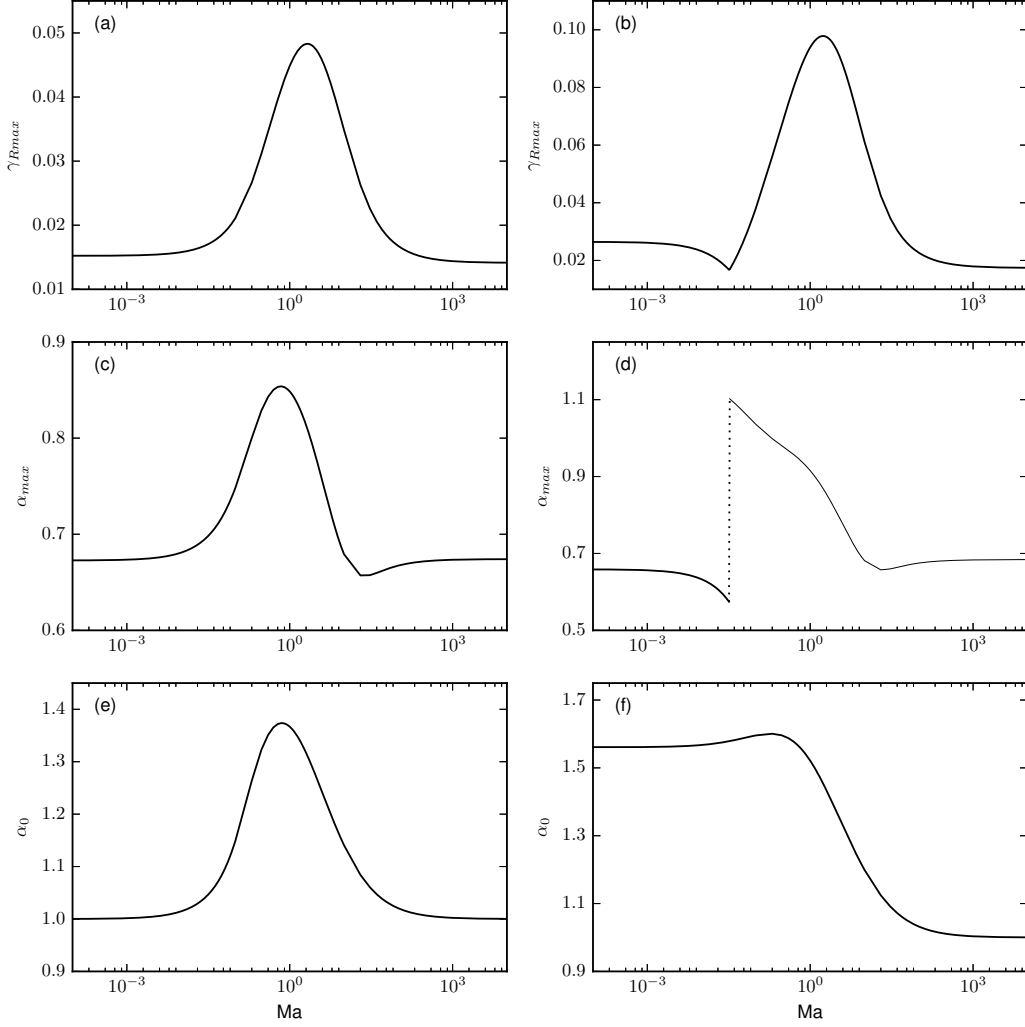


Figure 12: (a,b) $\gamma_{R\max}$, (c,d) α_{\max} and (e,f) α_0 as functions of Ma for $\text{Bo} = -1.0$ in the R sector (a,c,e) and S sector (b,d,f), for the same s and (n, m) points as in figure 11.

Solving for α yields

$$\alpha^4 \sim 48 \frac{(m-1)^2(n+1)^2}{n(n^3+m)} s^2 \text{Ma}^{-3} \text{Bo}^{-1} \gamma_R. \quad (5.7)$$

Equation (5.5) is substituted into (5.7), from which the following asymptotic expression for α_{\max} is obtained:

$$\alpha_{\max} \approx \frac{[12\varphi(1-n)(m-n^2)]^{1/4}(m-1)^{1/2}s}{(n^3+m)} \text{Ma}^{-3/4} \text{Bo}^{-1/4}. \quad (5.8)$$

Panels (b) and (d) show that $\gamma_{R\max} \downarrow 0$ and α_{\max} approaches some non-zero constant as $\text{Ma} \downarrow 0$. Therefore, equation (3.19) is approximately linear for $\gamma_R \ll 1$, $c_{10}\gamma_R\text{Ma} + c_{01} \approx 0$ so that

$$\gamma_R \approx -\frac{c_{01}}{c_{10}} \text{Ma}^{-1} \quad (5.9)$$

where the c_{ij} are independent of Ma . An equation for α_{\max} is obtained by differentiating (5.9) with respect to α and solving $d\gamma_R/d\alpha = 0$ numerically for α , which is then substituted into (5.9) to obtain $\gamma_{R\max}$.

In contrast to the case shown in figure 11 for $\text{Bo} > 0$, the flow is unstable for all Ma when $\text{Bo} < 0$ in either the R or S sectors. Moreover, figures 12 (a) and (b) also show that $\gamma_{R\max}$ has a global maximum at

$\text{Ma} = O(1)$. However, in the S sector $\gamma_{R\text{max}}$ decreases with increasing Ma for sufficiently small Ma , up to $\text{Ma} = \text{Ma}_0$. At $\text{Ma} = \text{Ma}_0$ there is a jump in α_{max} . This behavior is due to the fact that the dispersion curve has two maxima, and at this particular value of Ma there is a jump in the location of the global maximum, similar to that shown in figure 10. Figure 12 also shows that $\gamma_{R\text{max}}$, α_{max} and α_0 all approach some finite positive constant in the limits $\text{Ma} \uparrow \infty$ and $\text{Ma} \downarrow 0$ for both sectors.

Let us discuss the asymptotics of α_0 with respect to the Marangoni number for the case of $\text{Bo} < 0$. Panels (e) and (f) of figure 12 indicate that α_0 asymptotes to non-zero constants as both $\text{Ma} \uparrow \infty$ and as $\text{Ma} \downarrow 0$. The relevant values of α_0 can be obtained as follows. For $\text{Ma} \uparrow \infty$, the dominant term in equation (3.21) is the Ma^3 term, and since $k_{13} \neq 0$ this implies that $\text{Bo} + \alpha^2 \approx 0$, or

$$\alpha_0 \approx |\text{Bo}|^{1/2}. \quad (5.10)$$

For $\text{Bo} = -1$, $\alpha_0 \approx 1$ which is consistent with the numerical results shown in figures 12 (e) and (f). In the limit $\text{Ma} \downarrow 0$, equation (3.21) reduces to

$$(k_{11} + k_{13}B^2) \text{Ma}B \approx 0. \quad (5.11)$$

In the R sector, the solution $\alpha_0 \approx |\text{Bo}|^{1/2}$ is again obtained because k_{13} is always positive and k_{11} is the product of $(m-1)$ and a positive function, and thus $k_{11} > 0$ in the R sector. However, in the S sector $k_{11} < 0$, and α is a solution of $k_{11} + k_{13}B^2 = 0$ which is solved numerically for α . The solution is approximately $\alpha_0 \approx 1.56$, and agrees with figure 12 (f).

Next, the asymptotics of $\gamma_{R\text{max}}$ and α_{max} in the limit $\text{Ma} \uparrow \infty$, and then in the limit $\text{Ma} \downarrow 0$, (panels (a, b, c, d) of figure 12) are discussed. In this case, the terms proportional to Ma^3 in equation (3.19) yield

$$c_{03} + c_{13}\gamma_R \approx 0, \quad (5.12)$$

where the coefficients c_{ij} correspond to the $\gamma_R^i \text{Ma}^j$ terms in equation (3.19). Therefore,

$$\gamma_R \approx -\frac{c_{03}}{c_{13}} \approx -\frac{1}{2} \frac{(s_\alpha^2 - \alpha^2) (s_{\alpha n}^2 - \alpha^2 n^2) (\text{Bo} + \alpha^2)}{\alpha (s_\alpha^2 - \alpha^2) (s_{\alpha n} c_{\alpha n} + \alpha n) m + \alpha (s_{\alpha n}^2 - \alpha^2 n^2) (s_\alpha c_\alpha + \alpha)}. \quad (5.13)$$

Again, one must solve $d\gamma_R/d\alpha = 0$ numerically for α_{max} which in turn is substituted into equation (5.13) to obtain $\gamma_{R\text{max}}$.

Figure 13 shows the results of varying the shear parameter s . For any fixed s , the growth rate has a global maximum over the (α, Ma) -plane, denoted $\max \gamma_R$. We denote $\alpha(\max \gamma_R)$ and $\text{Ma}(\max \gamma_R)$ the values of the wavenumber and Marangoni number, respectively, at which the growth rate attains its maximum, $\max \gamma_R$. These quantities are plotted versus s in figure 13, for selected sampling points in the R and S sectors. We see that while in panels (a) and (c) the dependencies are linear, and also practically independent of the Bond number, this does not hold for the $\alpha(\max \gamma_R)$ shown in panel (b); in particular, in all four cases shown there, it stays almost constant (of magnitude order 1) at large s but falls off precipitously to zero as $s \downarrow 0$.

In this subsection we only had to deal with the long-wave instability because the values of Ma considered are either sufficiently large or sufficiently small, or the viscosity ratio was not sufficiently close to the $R-Q$ boundary $m = n^2$. It turns out that for the intermediate values of Ma and the appropriate values of m , even in the R sector, a different type of instability, called the ‘‘mid-wave’’ instability (HF), may happen. Its definition is recalled in the next subsection where the Q sector is considered, since this instability is more prevalent there. Some results on the mid-wave instability in the R sector are found in section 6 together with similar results for the Q sector. In the S sector, the mid-wave instability sometimes coexists with the long-wave instability of the robust mode. However, as far as we have observed, it is always weaker than the long-wave instability of the surfactant branch there. This is also discussed in section 6.

5.3 Surfactant effects in the Q sector

It was shown in HF (for $\text{Bo} = 0$) that for $\text{Ma} > 5/2$ and $m > n^2$ (Q sector), there is a mid-wave instability such that $\gamma_R > 0$ for a finite α -interval bounded away from $\alpha = 0$. (Note that the mid-wave instability was called type I in Cross and Hohenberg [1993] while the long-wave instability was called type II). In order

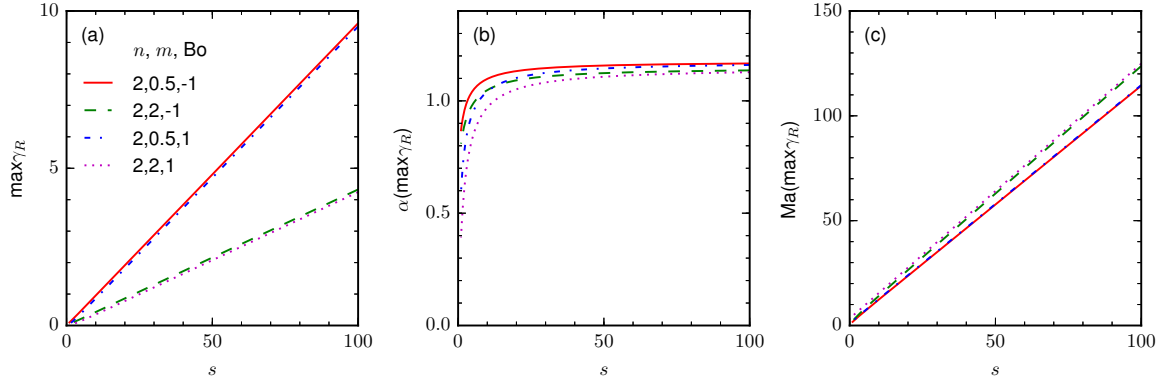


Figure 13: The influence of s on (a) the maximum of $\gamma_{R\max}$ over all α and Ma in the R sector (at $n = 2$ and $m = 2$) and the S sector (at $n = 2$, $m = 0.5$) for two different values of Bo as indicated in the legend. Panels (b) and (c) show the corresponding α and Ma .

to investigate such an instability allowing for nonzero Bond numbers, we introduce a critical Marangoni number, Ma_{cM} that corresponds to the onset (or the turnoff) of the mid-wave instability, and let α_{cM} be the corresponding wavenumber. Thus, the quantities Ma_{cM} and α_{cM} satisfy the equations $\gamma_R = 0$ and $\partial\gamma_R/\partial\alpha = 0$. In view of the quartic equation (3.19), Ma_{cM} and α_{cM} (for a given Bo) can be found by numerically solving simultaneously equation (3.21), which we write in the notation used in equation (3.22),

$$C_0(\text{Ma}, \alpha, \text{Bo}) = 0, \quad (5.14)$$

along with

$$\frac{\partial}{\partial\alpha}C_0(\text{Ma}, \alpha, \text{Bo}) = 0. \quad (5.15)$$

To illustrate the change of stability with Ma , in the top panels of figure 14, the growth rate in the Q sector (for $n = 2$ and $m = 5$, at $s = 1$) is plotted for three selected values of the Marangoni number and $\text{Bo} = -0.45$. The numerical results show that the instability is long-wave provided $\text{Ma} < \text{Ma}_{cL}$ (≈ 2.28 for the figure parameters). This is then followed by a region of stability when $\text{Ma} \in [\text{Ma}_{cL}, \text{Ma}_{cM}]$, where $\text{Ma}_{cM} \approx 15.6$. For $\text{Ma}_{cL} < \text{Ma} < \text{Ma}_m$, γ_R decreases monotonically with α (so that there is no $\gamma_{R\max}$; such dispersion curves are not shown in the top right panel), but starting from the Ma_m (≈ 3.70), the local maximum $\gamma_{R\max}$ appears on the dispersion curves. So, the growth rate γ_R has a local maximum $\gamma_{R\max}$ at some $\alpha_{max} > 0$ provided $\text{Ma} \geq \text{Ma}_m$; and once Ma exceeds Ma_{cM} , $\gamma_{R\max}$ becomes positive, i.e., the mid-wave instability switches on. Note that when $\text{Ma} > \text{Ma}_{cM}$ for at least some interval of Ma corresponding to the mid-wave instability, there are two positive marginal wavenumbers, one on the left at $\alpha = \alpha_{0L}$ and another one on the right at $\alpha = \alpha_{0R}$ so that the interval of unstable wavenumbers is $\alpha_{0L} < \alpha < \alpha_{0R}$. (Cases with both finite and infinite Ma intervals of mid-wave instability can be seen below in figure 20(a) and are discussed in the last paragraph of section 6.3.)

Although the stability properties of the normal modes are fully given by the dispersion curves (see panels (a) and (b) of figure 14), the normal modes have additional remarkable properties, such as the phase speed, the phase difference between the co-traveling waves of the interface and the surfactant, and the amplitude ratio of the interface to the surfactant disturbances. As an example, these quantities are plotted in figure 14 as functions of the wavenumber α . There, one notices a special value of the wavenumber, α_s , close to 0.7, at which the phase shift of the decaying branch has a jump discontinuity. The wave speed at α_s is zero for any Ma , so all three curves intersect at the same point $(\alpha_s, 0)$; similarly, the amplitude ratio is zero, independent of Ma . For the other branch, in the right panels (which, as panel (b) shows, goes, as Ma increases, from long-wave unstable, to stable and then to mid-wave unstable), all three growth rates are equal at the same α_s , and the wave speeds are equal as well, but the amplitude ratios are non-zero and different.

To explain these observations, note that the zero amplitude ratio implies that if $h = 0$ and $G \neq 0$, then from the first equation of (3.5) $A_{12} = 0$. Its solution, with the explicit expression of A_{12} from (B.3), yields

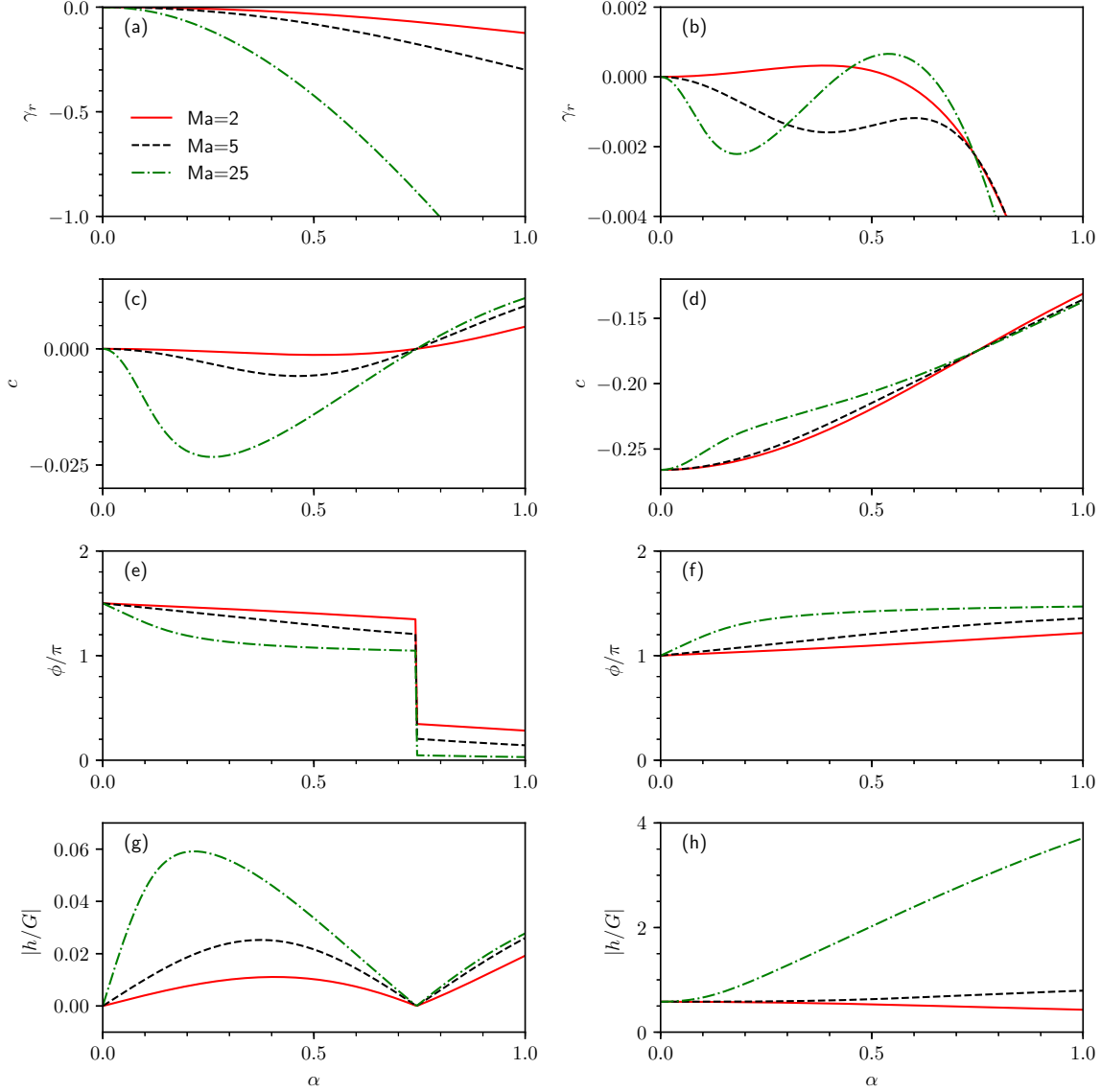


Figure 14: Curves for the four different functions of the wavenumber in the Q sector ($n = 2$, $m = 5$) for $s = 1$ and $\text{Bo} = -0.45$. The stable mode corresponds to the panels of the left-hand column, and the less stable mode to the panels of the right-hand column. For the three values of Ma given in the legend, panels (a) and (b) show the growth rates, (c) and (d) show the wave velocities, (e) and (f) show the interface-surfactant phase shifts, and (g) and (h) show the interface/surfactant amplitude ratio. The transition from the long-wave instability to stability to the mid-wave instability as Ma increases is evident in panel (b).

α_s in terms of n and m (but independent of Ma). The second equation of (3.5) with $h = 0$ yields $\gamma = -A_{22}$, which by (B.6), is real, negative, and proportional to Ma . This agrees with the left upper panel of figure 14. The wave speed is zero because $\text{Im}(\gamma) = 0$. The other mode corresponds to the right panels of this figure, and must have $h \neq 0$. Since $A_{12} = 0$ for $\alpha = \alpha_s$, we must have $\gamma + A_{11} = 0$. This implies $\text{Im}(\gamma) > 0$, i.e. a negative wave speed value, independent of Ma , corresponding to the triple intersection in panel (d) of figure 14. The growth rate, $\gamma_R = -\text{Re}(A_{11})$, is seen to be negative and independent of Ma , which explains the

triple intersection in panel (b). However, since $h \neq 0$ for this branch, the amplitude ratio is found to be

$$\left| \frac{h}{G} \right| = \left| \frac{A_{11} - A_{22}}{A_{21}} \right|.$$

Only A_{22} depends on Ma , and $|h/G|$ changes with Ma , so the three curves in figure 14 go through different points at $\alpha = \alpha_s$.

Having noticed the existence of the normal modes in which the surfactant is disturbed, $G \neq 0$, but the interface is undisturbed, $h = 0$, the question arises if there exist some “opposite” modes, in which only the interface, but not the surfactant is disturbed, so that $G = 0$, but $h \neq 0$. We answer this question in Appendix D. It turns out that such modes are possible, but only when $s = 0$.

In figure 15, $\gamma_{R\max}$, α_{\max} and α_0 are plotted versus the Marangoni number for $n = 2$, $m = 5$, $s = 1$ and for four selected values of Bo . If Bo is sufficiently negative, as in panels (a) and (c), then $\gamma_R > 0$ for all Ma . For $\text{Ma} < \text{Ma}_{LM}$, the instability is long-wave, in other words, there is no α_{0L} , since its definition implies that α_{0L} must be non-zero. However, a mid-wave instability ensues when $\text{Ma} > \text{Ma}_{LM}$, and there appears $\alpha_{0L} > 0$ (as in panels (b) and (d)). Initially, α_{0L} increases rapidly, while α_{0R} decreases by a small amount, leading to the shrinkage of the interval of unstable wavenumbers. After reaching a maximum, α_{0L} decreases towards zero with increasing Ma but never attains the zero value so that the instability does not return to the long-wave type, and the interval of unstable wavenumbers slowly expands. When $\text{Bo} = -0.51$ (see panels (e) and (f)), the stability picture up to $\text{Ma} = \text{Ma}_{cM_1}$ is very similar to that displayed in panels (b) and (d). The instability is long-wave provided $\text{Ma} < \text{Ma}_{LM}$. Starting at $\text{Ma} = \text{Ma}_{LM}$, corresponding to the lower left dot in panel (f), the long-wave instability disappears, and the mid-wave instability mentioned previously emerges. However, as Ma continues to increase, the interval of unstable wavenumbers quickly shrinks to a single, non-zero, α point, indicated by the dot at $\text{Ma} = \text{Ma}_{cM_1}$. The flow then becomes stable, with $\gamma_R < 0$ for a range of Marangoni numbers, $\text{Ma}_{cM_1} < \text{Ma} < \text{Ma}_{cM_2}$. Therefore, in this range, α_{0L} and α_{0R} are non-existent, but α_{\max} is defined because γ_R has a local maximum at a nonzero α . The mid-wave instability reappears at Ma_{cM_2} , (see the right-most dot in panel (f)) starting from $\gamma_R = 0$, which corresponds to the right-hand intersection point in panel (e). As Ma increases beyond Ma_{cM_2} , the interval of unstable wavenumbers expands in both directions. In the final set of panels, (g) and (h), with $\text{Bo} = -0.1$, the flow is stable, and $\gamma_{R\max}$, α_{\max} , and α_0 do not exist, in the interval $\text{Ma}_{cL} \leq \text{Ma} \leq \text{Ma}_m$. This is because γ_R has no local maximum at any $\alpha > 0$. Note that, as with the previous set of panels, the flow is long-wave unstable for $\text{Ma} < \text{Ma}_{cL}$ (i.e., to the left of the left-most dot of panel (h)) and mid-wave unstable for $\text{Ma} > \text{Ma}_{cM}$ (to the right of the right-most dot).

Thus, we have observed here, for the first time, the existence of another route to the mid-wave instability: the continuous transition from long-wave instability (see the marked point $(\text{Ma}_{LM}, 0)$ in panel (f) of figure 15). Only the other route, the onset of mid-wave instability from stability, was present for the case of zero gravity (see HF). In the former scenario, the mid-wave instability has a non-zero growth rate and a final support interval from the very beginning. A detailed investigation of the boundaries between the domains of the mid-wave instability, long-wave instability and stability in the (Ma, Bo) -plane appears below in section 6.

Figure 16 shows the dependencies of $\max \gamma_R$, $\alpha(\max \gamma_R)$ and $\text{Ma}(\max \gamma_R)$ on the shear parameter s in the Q sector similar to those shown in figure 13 for the other two sectors. We observe that the existence of the global maximum in Ma of the growth rate maxima with respect to the wavenumber is less common in the Q sector, especially for $\text{Bo} > 0$. At smaller values of s , the global maximum becomes a local one like the one in figure 15(a). This is indicated in figure 16 as the change from the solid to the dashed curve at the negative Bo and from the dashed to the dotted one at the positive Bo . At still smaller s , to the left of the end dot on each curve, there are neither global nor local maxima.

6 (Ma, Bo) -plane stability diagrams

6.1 Regions of the long-wave and mid-wave instabilities

Here we present a detailed account of the mid-wave instability changes as the viscosity ratio is increased, starting from a value in the R sector, $1 < m < n^2$, then crossing the $m = n^2$ border and further growing in

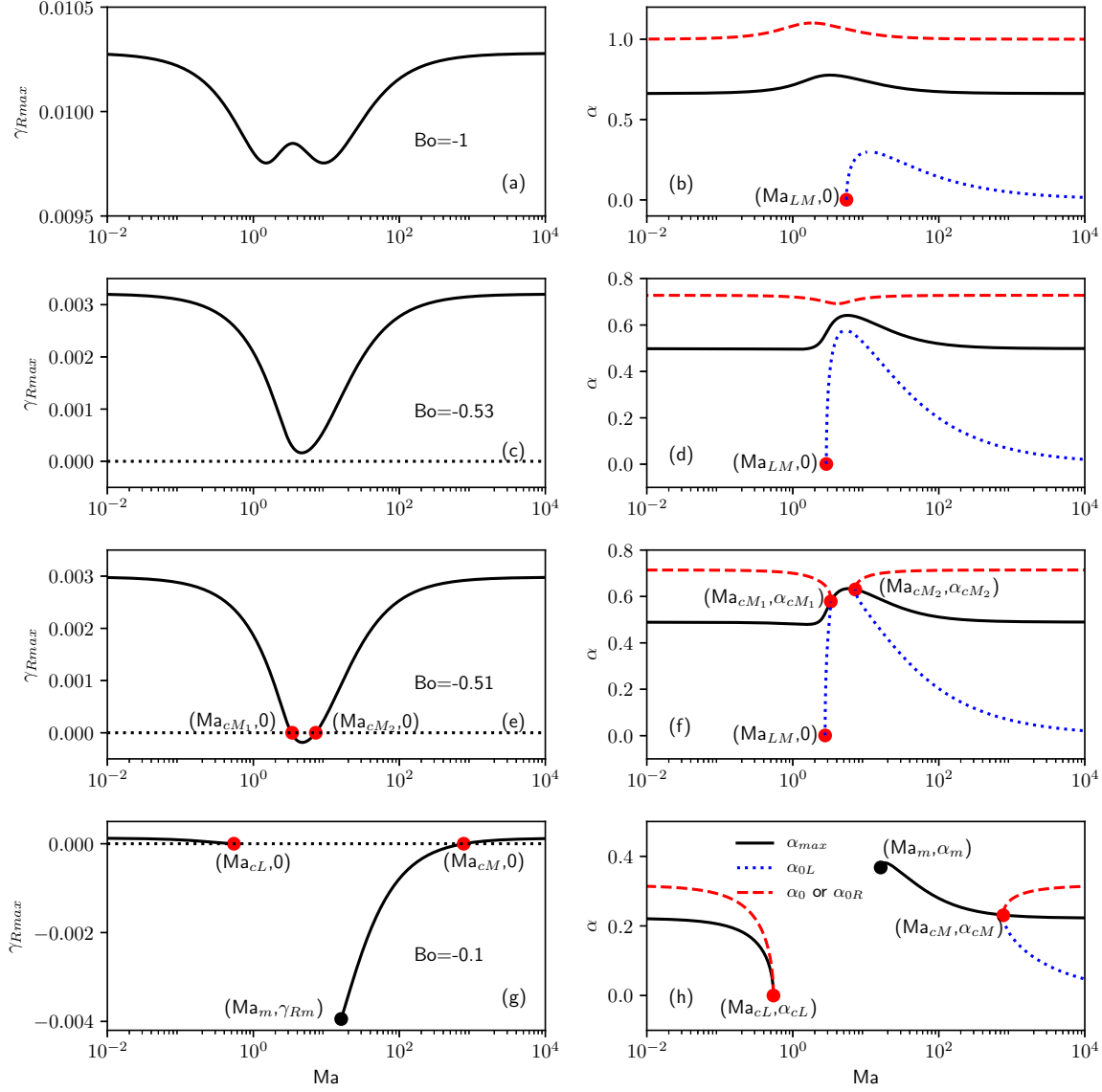


Figure 15: Plots of $\gamma_{R\max}$ (left-hand panels) and corresponding α_{\max} , α_{0R} , and α_{0L} (right-hand panels) vs Ma in the Q sector (here at $n = 2$, $m = 5$) for $s = 1$ and the four indicated values of Bo . (For labeled points, see the text.)

the Q sector, $m > n^2$. In the R sector, the robust branch is long-wave unstable provided $Bo < Bo_{cL}$ where $Bo_{cL}(Ma)$, as given by (4.15), is positive. If $m < n^2$ and sufficiently far from the $m = n^2$ border, there exists just one stability boundary, given by $Bo = Bo_{cL}$; it is a straight line (starting at the origin) that separates the long-wave unstable and stable regions, as shown in figure 17(a). As m increases and gets sufficiently close to $m = n^2$, the onset of a mid-wave instability is observed for certain intervals of Ma and Bo . In panels (b) and (c), a mid-wave instability occurs provided $Bo_{cL} < Bo < Bo_{cM}$, for a finite interval of the Marangoni numbers, $Ma_{LM1} < Ma < Ma_{LM2}$, as the Bo_{cL} and Bo_{cM} curves “intersect” each other at $Ma = Ma_{LM1}$ and $Ma = Ma_{LM2}$. The “quasi-intersection” points, marked in the figure as filled squares, are the boundary points for the critical curve but are not the critical points themselves: the critical wavenumber decreases to zero as $Ma \rightarrow Ma_{LMj}$, but the zero value is prohibited for a critical wavenumber. When m is approaching ever closer to n^2 , at some m the critical curve of the mid-wave instability acquires a maximum and a minimum,

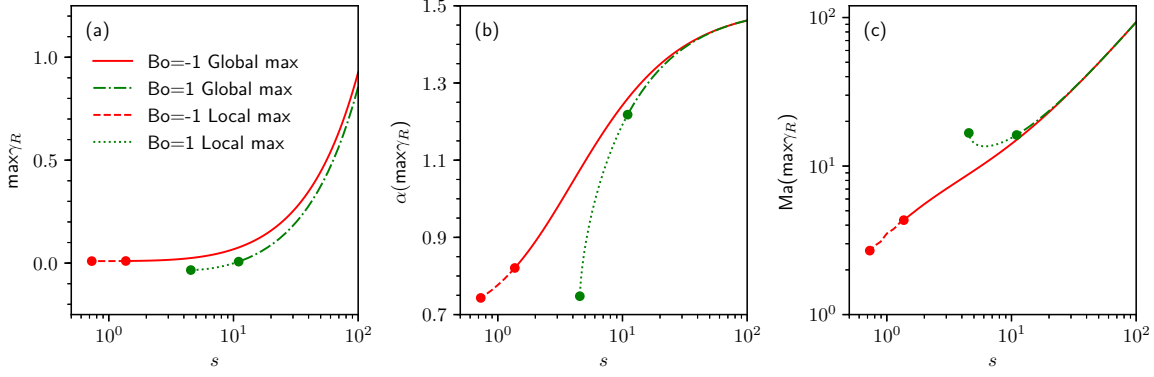


Figure 16: The influence of s on (a) the maximum of γ_R over all α and Ma in the Q sector (here at $n = 2$, $m = 5$) for two different values of Bo , one positive and the other one negative. Panels (b) and (c) show the values of α and Ma at which this maximum occurs. The global maxima of γ_{Rmax} with respect to Ma , present at larger s , become local maxima between the pairs of dots on each curve. At smaller s , to the left of the end dot on each curve, there are neither global nor local maxima.

such as the ones in panel (d). Clearly, for each fixed Ma of the Ma -interval $\text{Ma}_{LM1} < \text{Ma} < \text{Ma}_{LM2}$, there are three distinct Bo -intervals: a semi-infinite interval of stability $\text{Bo} > \text{Bo}_{cM}$; a finite interval of mid-wave instability $\text{Bo}_{cL} < \text{Bo} < \text{Bo}_{cM}$; and a semi-finite interval of long-wave instability $\text{Bo} < \text{Bo}_{cL}$.

In figure 18(a), the wavenumber α_{cM} corresponding to Bo_{cM} is plotted versus Ma for the values of m corresponding to panels (b) and (c) of figure 17, and also for $m = 15.96$, which is closer to the $m = n^2$ boundary value, $m = 16$, than $m = 15.75$ of figure 17(d). With this, 18(a) suggests the hypothesis that in approaching the sector boundary, the larger quasi-intersection value of Ma tends to infinity. The latter is in accordance with the stability diagram for the sector boundary value $m = 16$ (see figure 19 below). For all these cases, α_{cM} attains a maximum at an Ma such that $\text{Ma}_{LM1} < \text{Ma} < \text{Ma}_{LM2}$. Figure 18(b) shows, for the parameters of figure 17(c) and $\text{Ma} = 25$, that, as the Bond number grows, when it reaches the value Bo_{cL} , the long-wave instability changes into the mid-wave one by the left endpoint of the interval of unstable α departing from the zero α point. The unstable α interval continues to shrink from both ends, and finally becomes a single non-zero α point at $\text{Bo} = \text{Bo}_{cM}$, the right-most point on the curve. The maximum growth rate (not shown) decreases to zero at this point, and there is stability for larger Bo , in agreement with figure 17(c). On the $m = n^2$ border (e.g., for $m = 16$, $n = 4$), the robust branch is long-wave unstable in the half-plane $\text{Bo} < 0$ (with the boundary line $\text{Bo}_{cL} = 0$), as shown in figure 19. Along the Ma -axis ($\text{Bo} = 0$), the stability results of HF that show the existence of a mid-wave instability for $\text{Ma} > 5/2$ are recovered: $\text{Ma}_{LM1} = 5/2$ and $\text{Ma}_{LM2} = \infty$. Notably, $\text{Bo}_{cL}(\text{Ma}) \downarrow 0$ as $\text{Ma} \rightarrow \infty$. We also note that there is just a single extremum, a maximum, on the critical curve. In the Q sector, $\text{Bo}_{cL}(\text{Ma}) < 0$, as given by (4.15). We see the threshold curves $\text{Bo} = \text{Bo}_{cL}(\text{Ma})$ in figure 20, for each value of m represented there; all the threshold curves have the (Bo, Ma) -origin as their left-hand end (with linear scales on both axes, all the threshold lines would start from the origin and have a negative slope). The long-wave instability occurs below each threshold curve; the region of long-wave instability is labeled with an “L” in the figure. At some point on each L-threshold curve, the critical curve of the mid-wave instability begins, going unbounded rightward, in the direction of increasing Ma ; as $\text{Ma} \uparrow \infty$, each critical curve is asymptotic to $\text{Bo} = 0$ (thus, in a difference with the R sector, but similar to the boundary between the R and Q sectors, the threshold line of the long-wave instability intersects the critical curve of the mid-wave instability at a single point); however, in contrast with the boundary between the R and Q sectors, the critical curve approaches the axis $\text{Bo} = 0$ from below. Also, at the threshold-critical quasi-intersection, the $\text{Bo}_{cL}(\text{Ma})$ increases as $\text{Ma} \downarrow \text{Ma}_{LM1}$. Since there is still a local maximum on the critical curve, just as there is one in the R sector and on the inter-sector boundary, it follows that there must be at least two local minima as well.

The mid-wave instability occurs below such a critical curve $\text{Bo} = \text{Bo}_{cM}$ (and above, or to the right of, the right-hand part ($\text{Ma} > \text{Ma}_{LM1}$) of the corresponding threshold curve $\text{Bo} = \text{Bo}_{cL}(\text{Ma})$). This region is

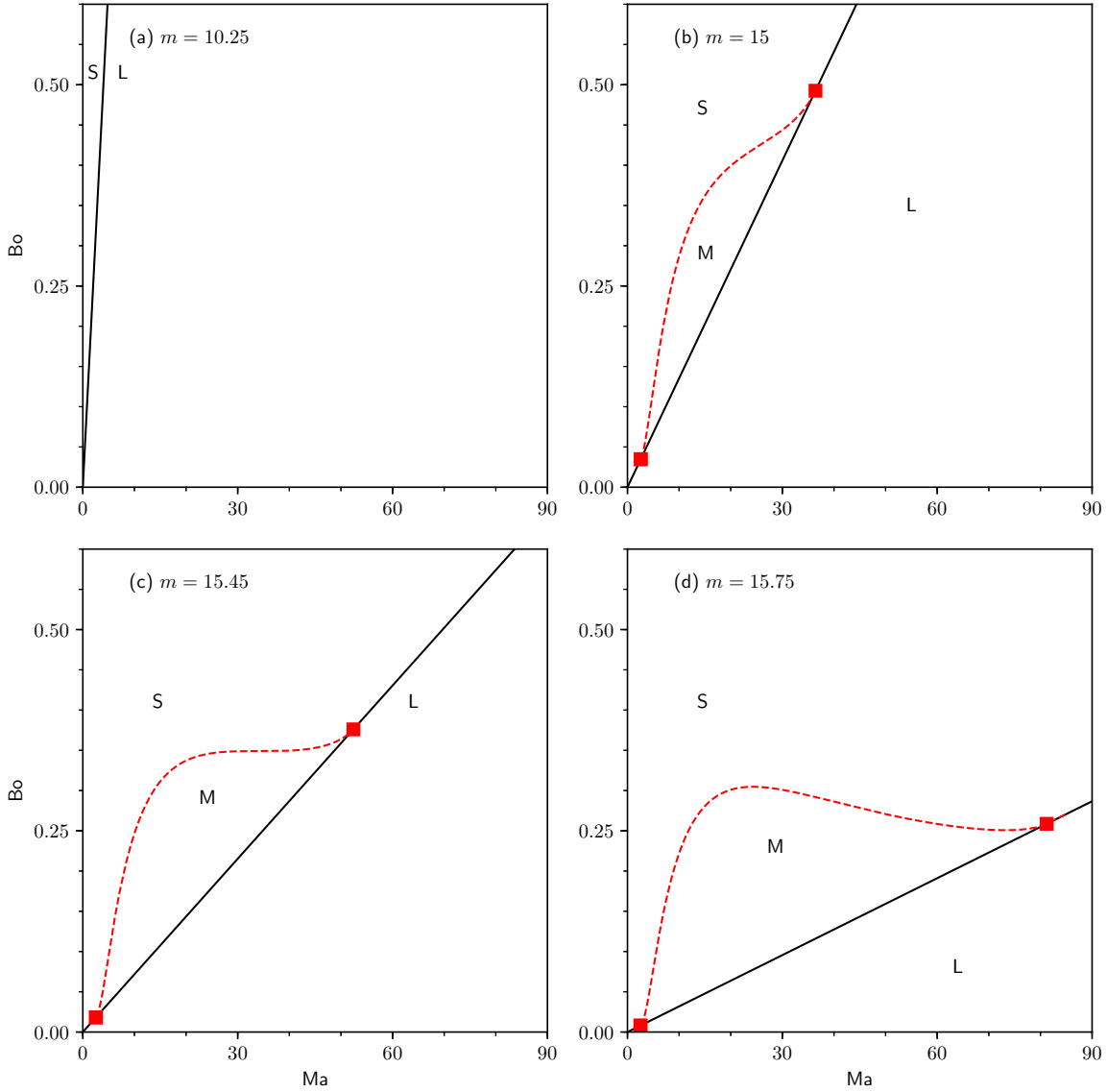


Figure 17: Stability diagrams in the (Ma, Bo) -plane showing the influence of the viscosity ratio m as $m \uparrow n^2$: (a) $m = 10.25$; (b) $m = 15$; (c) $m = 15.45$; and (d) $m = 15.75$. The solid and dashed curves represent long-wave and mid-wave instability boundaries respectively; S, L, and M denote the stable, long-wave unstable, and mid-wave unstable regions. Here $s = 1$ and $n = 4$.

labeled with an “M”. Above the critical curve, as well as above the left-hand part ($\text{Ma} < \text{Ma}_{LM1}$) of the corresponding threshold curve, the flow is stable. The critical curve is given by a single-valued function $\text{Bo} = \text{Bo}_{cM}(\text{Ma})$, that is seen in figure 20 to have two local minima and a maximum in between them, provided the viscosity ratio m is below a certain value m_N . These two minima appear to occur at the same value of Bo , and as m increases all three extrema move downward, but the single maximum moves faster than the two minima. Eventually, at $m = m_N$, the three extrema merge into a single minimum, such as the one on the $m = 36$ critical curve.

In the S sector, as was mentioned at the end of section 5.2, the mid-wave instability occurs for the robust mode, although it is overshadowed by the long-wave instability of the surfactant mode. It is illustrated in figure 21 for the parameter values indicated there. The zoom-in, the upper inset, shows that, in contrast

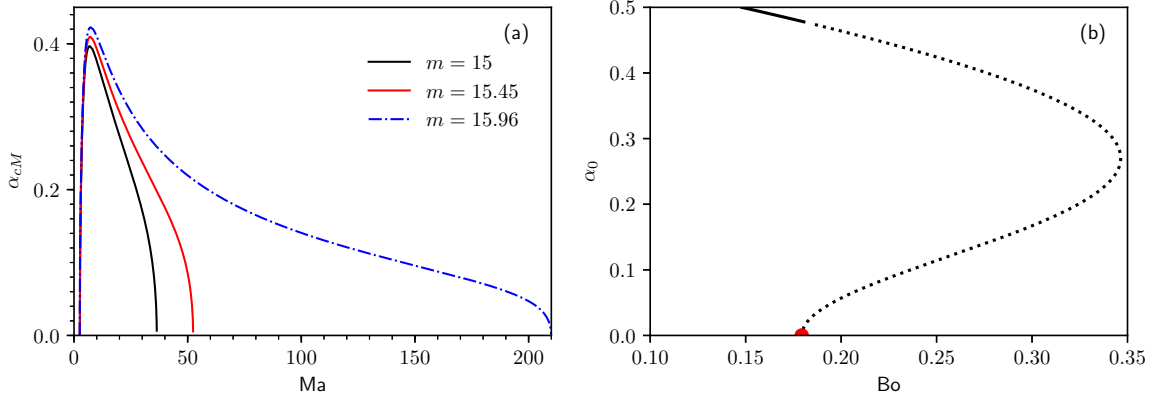


Figure 18: (a) The critical wavenumber α_{cM} versus Marangoni number Ma for the same parameter value choices as in figure 17; in particular, $n = 4$ and $s = 1$. (b) The marginal wavenumber α_0 versus Bond number Bo for $s = 1$, $Ma = 25$, $n = 4$, and $m = 15.45$. There is mid-wave instability in the region bounded by the two semicircles on the horizontal axis, long-wave instability to the left of this region, and stability to the right of this region.

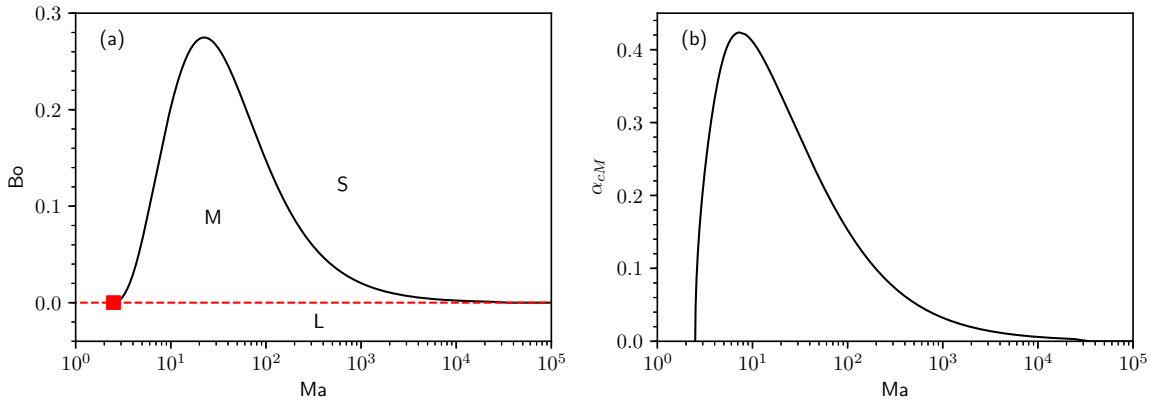


Figure 19: (a) Stability diagram in the (Ma, Bo) -plane similar to the ones shown in figure 17, for a case where $m = n^2$ (here $m = 16$) and (b) the corresponding critical wavenumber, α_{cM} . The end points have $Ma = 5/2$. Here $s = 1$.

with the other sectors, the critical curve does not end at its intersection with the threshold curve of the linear instability, but continues below the intersection, until it meets another critical curve. On the latter curve, each point corresponds to a dispersion curve having zero growth rate at a local minimum (as will be illustrated in the next figure). The bottom inset of figure 21 is a zoom-in near the quasi-intersection point of the lower critical curve and the threshold line, marked by a small circle, located at Ma slightly above 0.32 and Bo slightly above -3.45. The quasi-intersection point of the upper critical curve and the threshold line, marked by a small square, is located at Ma slightly above 0.046 and Bo slightly below -0.5. Figure 22 illustrates the change of the dispersion curves of the robust mode for the same values of n , m and s as in figure 21, and Ma fixed at 0.363 for a decreasing sequence of Bo values corresponding to moving in the upper inset of figure 21 from the domain of stability (22(a)) to long-wave instability (22(b)) to the domain of coexisting long-wave and mid-wave instabilities (22(c)) to the lower critical curve (corresponding to the zero minimum in figure 22(d)) and finally to the domain of long-wave instability (see panels (e) and (f) of figure 22). The mid-wave instability starts at a certain Bo between those of panels (b) and (c) as the maximum,

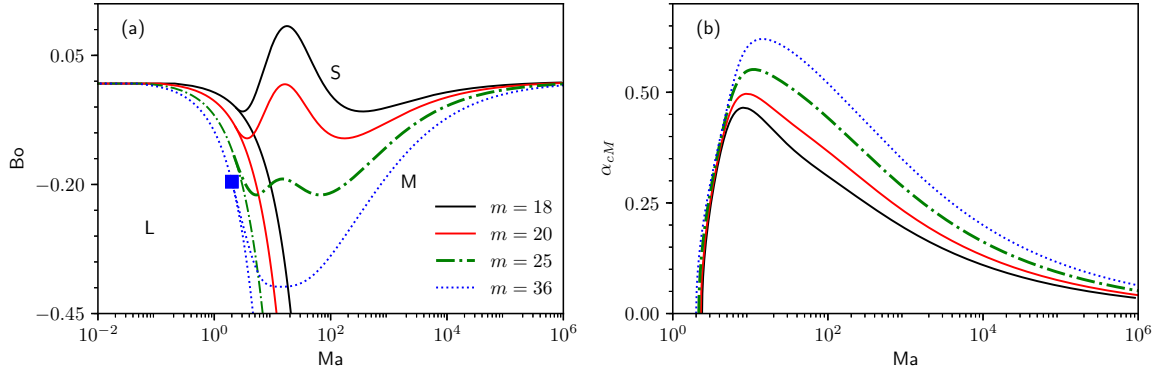


Figure 20: (a) Stability diagram showing the regions of mid-wave and long-wave instability and stability defined by the curves Ma_{cL} and Ma_{cM} as m increases in the Q sector, and (b) the wavenumber corresponding to Ma_{cM} for the indicated values of m . Here $n = 4$ and $s = 1$.

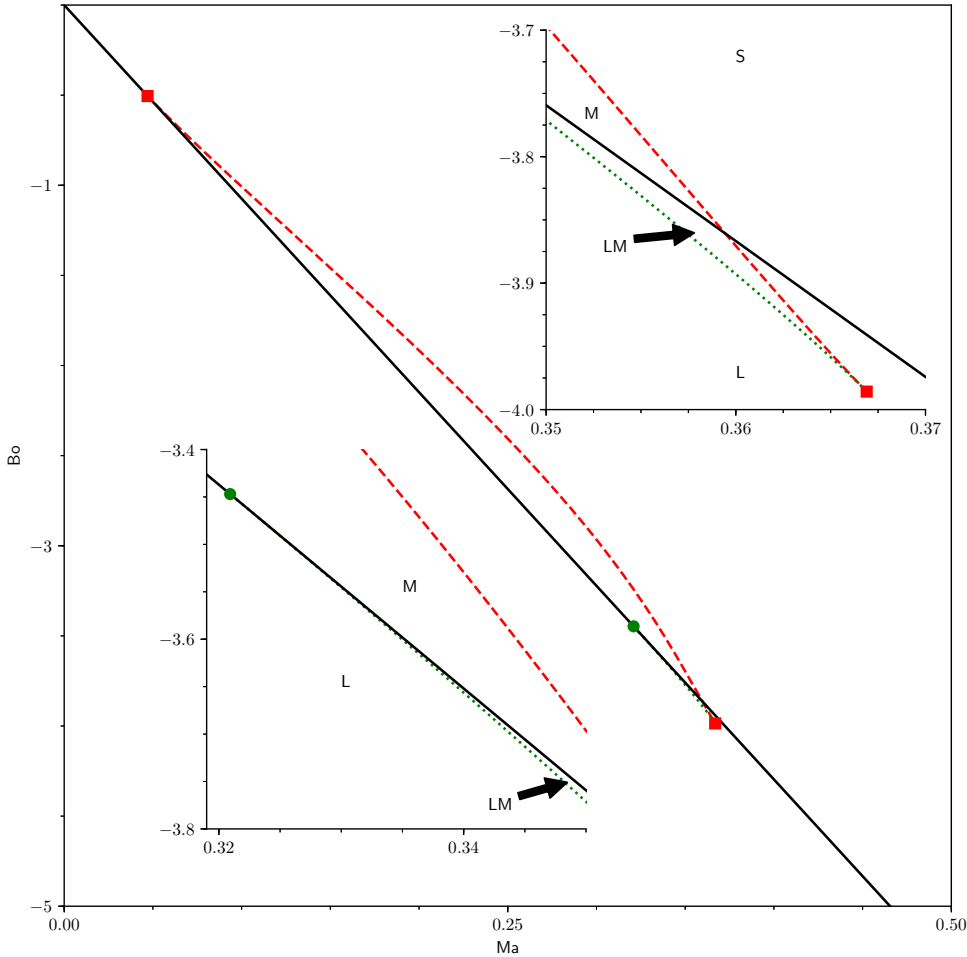


Figure 21: (a) Stability diagram of the less unstable mode for $s = 1$, $n = 10$, and $m = 0.1$. The long-wave instability is present below the solid line and absent above it, while the mid-wave instability is present between the dashed curve, and either the solid line line or the dotted curve. The top and bottom insets zoom in on the regions near the two lower pairwise intersections, marked by the square and the circle, respectively.

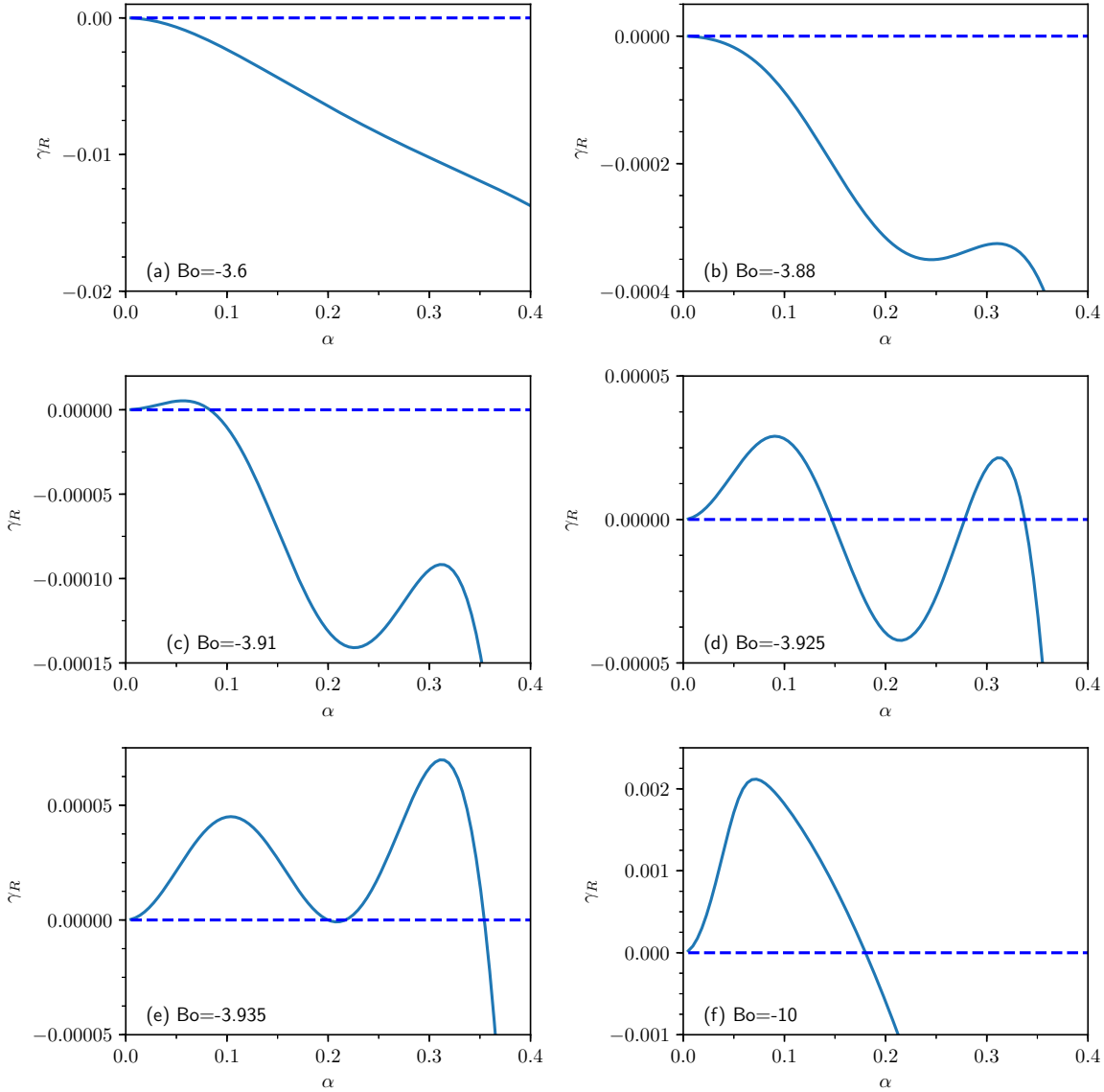


Figure 22: Dispersion curves for the robust mode in the S -sector. Here $n = 10$, $m = 0.1$, $s = 1$, and $\text{Ma} = 0.363$. The values of Bo are as indicated in each panel.

which is negative in panel (b), grows through the zero to positive values as in panel (c) near $\alpha = 0.3$. In this process both intervals of (co-existing) long-wave instability and mid-wave instability expand, until they coalesce which corresponds to the snapshot shown in panel (d). Also, in going from panel (c) to panel (d), the local minimum increases from negative to zero value, and becomes positive, as in panel (e). Finally, this minimum disappears, and the dispersion has a single maximum, see panel (f).

Figure 23 shows the salient features of the dispersion curves, such as the maximum growth rate, $\gamma_{R\max}$, the corresponding wavenumber, α_{\max} , and the marginal wavenumbers, α_0 , α_{0L} and α_{0R} , as continuous functions of the Bond number for three different values of the Marangoni number. In particular, figure 22 corresponds to panels (e) and (f) of figure 23. For smaller values of the Marangoni number, such as $\text{Ma} = 0.355$ in panels (c) and (d), which are to the left of the intersection of the (maximum) critical curve and the threshold curve, the mid-wave instability emerges before the long-wave instability as the value of Bo becomes more negative (see the upper inset of figure 21). For a small range of Bo , both long-wave and

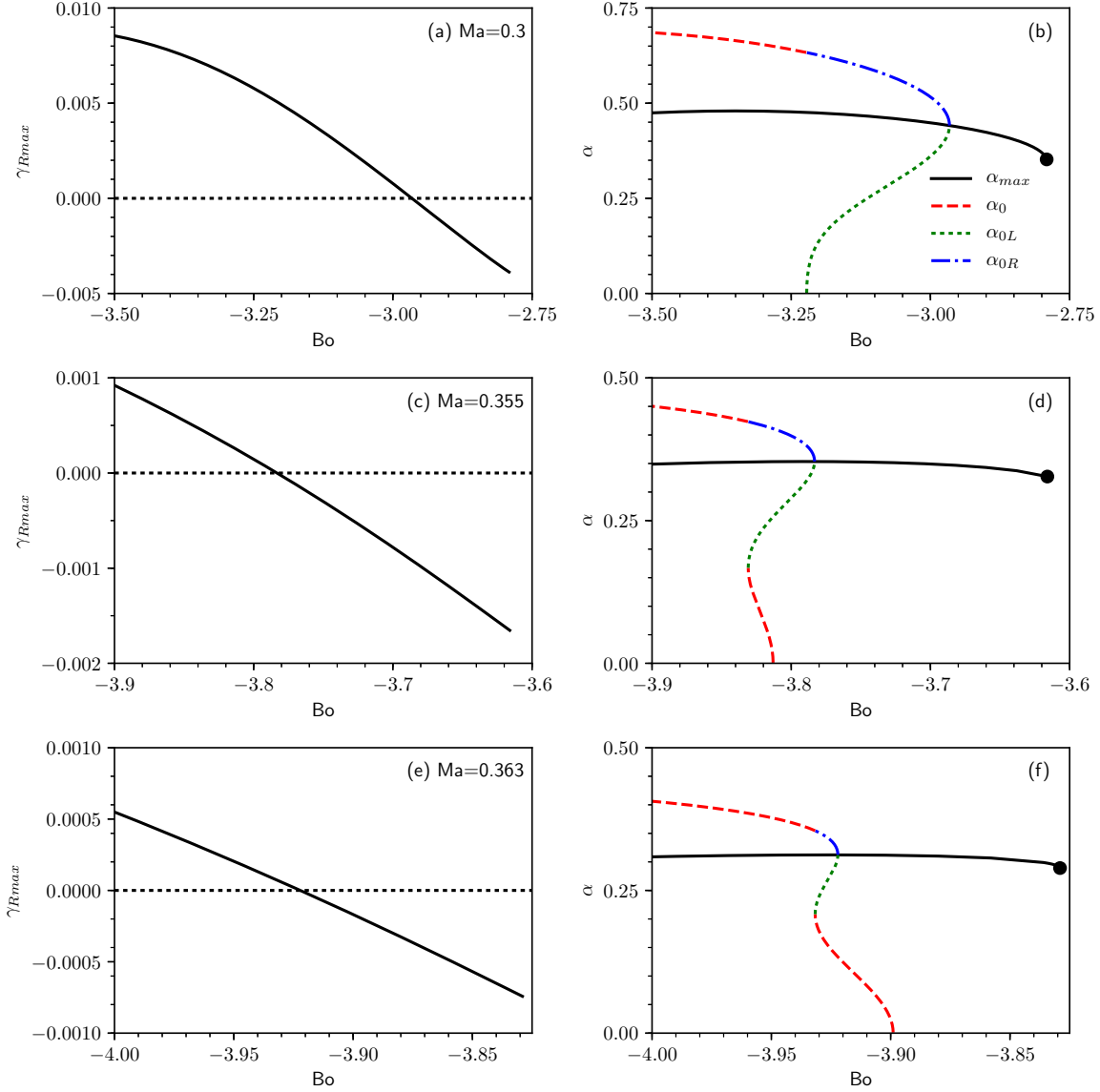


Figure 23: Plots of γ_{Rmax} , corresponding α_{max} , and α_0 , vs Bo in the S sector for the indicated values of Ma . Here $n = 10$, $m = 0.1$ and $s = 1$. Note that when there are two local maxima on the dispersion curves, γ_{Rmax} shown here corresponds to the right-hand maximum even if it is smaller than the left one.

mid-wave instabilities can coexist (indicated by the label “LM” in the upper inset of figure 21). This is then followed by a completely long-wave unstable regime. For still smaller Ma , such as $Ma = 0.3$, in panels (a) and (b), we observe the emergence of the mid-wave instability, which, subsequently, turns into a long-wave instability, similar to figure 18(b). Figure 24 is the plot of the critical wavenumber corresponding to the two critical curves in the preceding figure. It shows, similar to the analogous figures for the other two sectors, that the critical wavenumber, α_c , approaches zero at the quasi-intersection points. It also reveals that the rate of change of the critical wavenumber approaches infinity at the common point of the two critical curves. Using small wavenumber expansions as described in section 6.2, we obtained the cubic equation given by (6.9) below, and solved it numerically to verify that at the left quasi-intersection point $Ma=0.0458$, and at the other one $Ma=0.321$.

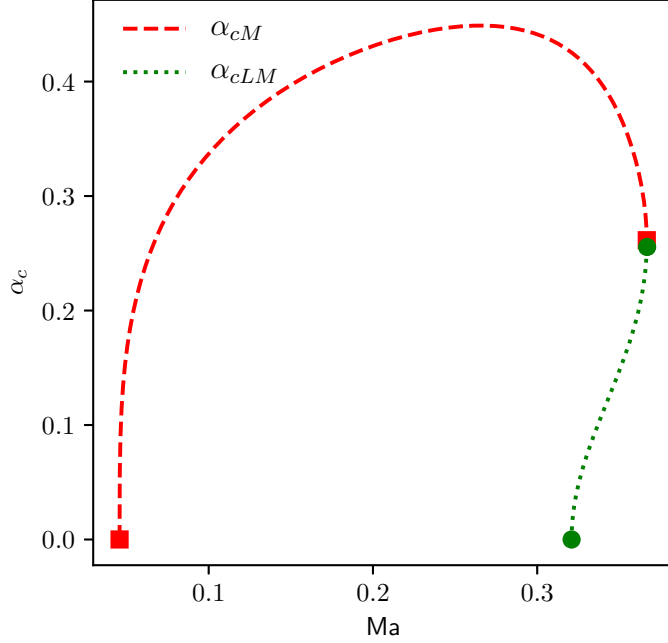


Figure 24: Critical α versus Ma corresponding to the previous figure.

6.2 Asymptotics of the critical curves near their boundaries

6.2.1 General considerations

It should be possible to establish the asymptotic behavior of the critical curves near their boundaries, in particular, the sense of the curve inclination at a finite boundary point, a priori, using only minimal numerical information. This, as already was indicated above, leads to certain conclusions about the number and sense of possible extrema, that in their turn facilitate the complete determination of the curve extrema. Near any finite quasi-intersection point, for both R and Q sectors, we look for the critical point coordinates in the form of generic power expansions

$$\text{Ma} = \text{Ma}_0 + \alpha^2 \text{Ma}_2 + \alpha^4 \text{Ma}_4 + \dots \quad (6.1)$$

and

$$\text{Bo} = \text{Bo}_0 + \alpha^2 \text{Bo}_2 + \alpha^4 \text{Bo}_4 + \dots, \quad (6.2)$$

where, to simplify notations, Ma_0 stands for Ma_{LMj} (with $j = 1, 2$), etc. We substitute these expansions into the critical curve equations (5.14) and (5.15) and require the collected coefficients of each power to vanish. Since the point $(\text{Ma}_0, \text{Bo}_0)$ lies on the threshold curve of the long-wave instability, we have $\text{Bo}_0 = \kappa \text{Ma}_0$, where κ is the coefficient of Ma in equation (4.15). Because of this relation, the leading orders α^6 in (5.14) and α^5 in (5.15) are satisfied identically. The next order system, given by the orders α^8 in (5.14) and α^7 in (5.15), is

$$\begin{aligned} k_{206} \text{Ma}_2 + k_{116} \text{Bo}_2 &= r_1, \\ 6k_{206} \text{Ma}_2 + 6k_{116} \text{Bo}_2 &= 8r_1, \end{aligned}$$

where the coefficients k_{pqr} are functions of (m, n, s) given in Appendix B, and r_1 is a cubic polynomial in Ma_0 whose coefficients are known combinations of k_{pqr} , and which lacks the quadratic term (cf. the discussion

around equation (6.10)). The consistency of this system requires that $r_1 = 0$, which is a cubic equation for Ma_0 . Clearly $\text{Bo}_2 = -(k_{206}/k_{116})\text{Ma}_2$, which simplifies to

$$\text{Bo}_2 = \kappa\text{Ma}_2. \quad (6.3)$$

The cubic equation for Ma_0 can be examined using the well known Cardano's formula and the underlying theory for the case with real coefficients.

The inclination of a critical curve at any quasi-intersection point is

$$d\text{Bo}/d\text{Ma} = (d\text{Bo}/d\alpha)/(d\text{Ma}/d\alpha). \quad (6.4)$$

Using (6.1) and (6.2) we get $d\text{Bo}/d\text{Ma} = \text{Bo}_2/\text{Ma}_2 = \kappa$, where we have used (6.3). Thus, at the boundary point, the critical curve is tangent to the threshold curve through that quasi-intersection point.

6.2.2 The R sector finite critical curves and the threshold for their existence

We find that in the R sector the cubic equation for Ma_0 has two distinct positive roots, corresponding to the two quasi-intersection points, for m greater than some threshold value m_d , and one non-physical negative root. For $m = m_d$, the two positive roots merge into a single double root, which means that the interval of mid-wave instability shrinks to a single point, so that there is no mid-wave instability for $m < m_d$. If the cubic equation is written in the form $\text{Ma}_0^3 + p\text{Ma}_0 + q = 0$, the condition for the double root is that a certain discriminant is zero, or $27q^2 + 4p^3 = 0$, whose solution for given n and s is m_d , the threshold value above which the mid-wave instability exists. For example, when $n = 4$ and $s = 1$, as in 17, $m_d = 10.2783$. This value of m is between those for the panels (a) and (b), as it should be. Thus, one can predict also the location of the boundaries of the critical curves in the R sector. A somewhat different way for this, leading to a cubic equation for Bo , is as follows. A more explicit form of the system (5.14)-(5.15) is

$$C_0(\text{Ma}, \alpha, \text{Bo}) = \text{Ma}(A_1 + A_2\text{Ma} + A_3\text{Ma}^2) = 0, \quad (6.5)$$

$$\frac{\partial C_0}{\partial \alpha} = \text{Ma}(A'_1 + A'_2\text{Ma} + A'_3\text{Ma}^2) = 0 \quad (6.6)$$

where

$$A_1 = k_{11}B + k_{13}B^3, \quad A_2 = k_{20} + k_{22}B^2, \quad A_3 = k_{31}B, \quad (6.7)$$

and the prime stands for the α -derivative. Since $\text{Ma} > 0$, we divide equations (6.5) and (6.6) by Ma , and then the system consists of two quadratic equations, from which we obtain two different linear equations for Ma , one by eliminating the quadratic term, and the other by eliminating the zero-power term. The solvability condition, obtained by equating the two expressions for Ma , is

$$(A_1A'_3 - A'_1A_3)^2 - (A_1A'_2 - A'_1A_2)(A_2A'_3 - A'_2A_3) = 0. \quad (6.8)$$

Since $\alpha \downarrow 0$ near a boundary point, we use the small- α expansions to find, to the leading order, the standard-form cubic equation

$$\text{Bo}^3g_3 + \text{Bo}g_1 + g_0 = 0, \quad (6.9)$$

where the coefficients are defined as $g_0 = k_{116}k_{206}^2$, $g_1 = k_{206}(k_{118}k_{206} - k_{116}k_{208})$, and $g_3 = k_{116}^2k_{318} - k_{116}k_{206}k_{228} + k_{206}^2k_{138}$. (One can see from the expressions for k_{pqr} that here $g_0 > 0$ and $g_3 > 0$.) This cubic equation can be written in the standard form $\text{Bo}^3 + p_1\text{Bo} + q_1 = 0$, with $p_1 = g_1/g_3$ and $q_1 = g_0/g_3$. The viscosity value $m_d(n, s)$ satisfies the double-root condition

$$27q_1^2 + 4p_1^3 = 0, \quad (6.10)$$

which is essentially the same equation as the one found above using a different approach, where no explicit expressions were shown for p and q (in fact, it is clear from relation (6.3) that $p_1 = \kappa^2p$ and $q_1 = \kappa^3q$).

Consider the asymptotics as $s \uparrow \infty$. Note that $p_1 \propto s^2$ and $q_1 \propto s^2$. Hence, (6.10) simplifies to $p_1 = 0$, which implies $g_1 = 0$ (provided $g_3 \neq 0$), and then, since $k_{206} > 0$, it follows that $k_{206}k_{118} = k_{208}k_{116}$. Expanding, this equation involves m and n only:

$$(1/2)\varphi(m - n^2)(m(n(8n - 3) + 7) + n(n(7n - 3) + 8))$$

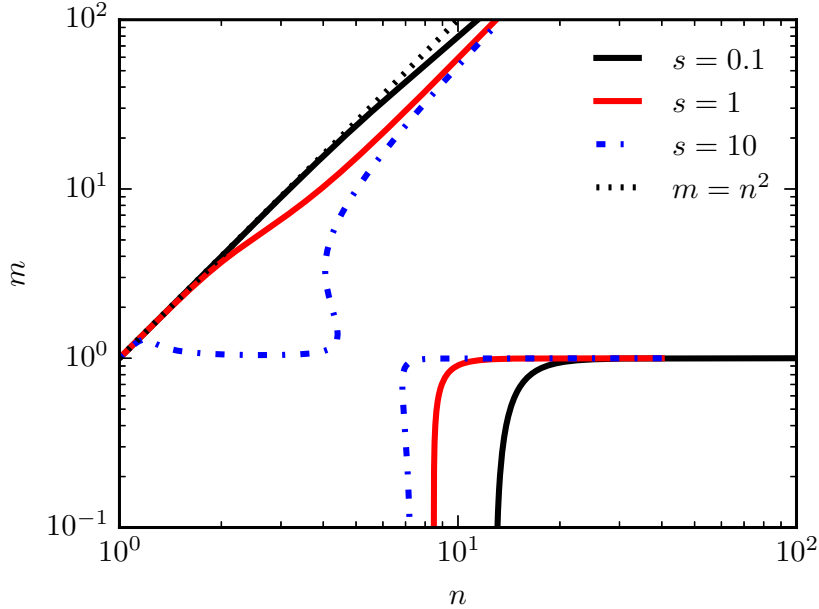


Figure 25: Numerical solutions of equation (6.10) for the representative values of s given in the legend.

$$= (n+1)(n+m)(m^2(n(3n+8)+3) - 4mn^2(n^2-1) - n^4(n(3n+8)+3)), \quad (6.11)$$

where φ is given by (4.6). For $n \uparrow \infty$, we look for solutions in the form $m \sim \chi n^2$ with $0 < \chi < 1$. The leading order is proportional to n^8 , yielding $9\chi^2 - 4\chi - 1 = 0$. The only acceptable solution is $\chi = (2 + \sqrt{13})/9 \approx 0.623$. Note that even for $s = 1$ and $n = 4$, our (mentioned above) result $m_d = 10.2783$ implies $m_d/n^2 \approx 0.643$ (cf. the asymptotic value 0.623).

If $s \uparrow \infty$ but $n \downarrow 1$, it turns out that no appropriate solutions exist for m_d . Then the curve $m = m_d(n)$ should intersect the sector boundary $m = 1$ at some finite $n = n_0 > 1$. Substituting $m = 1$ into (6.11), we obtain the following equation for n_0 : $(n-1)^4 - 16n^2 = 0$, which has a single acceptable solution, $n_0 = 3 + \sqrt{8}$. Consider now the asymptotic case $s \downarrow 0$. Here, equation (6.10) simplifies to the leading order equation $q_1 = 0$, and thus its numerator is also zero. But this contradicts the fact, mentioned above, that it is strictly positive. Therefore, there is no mid-wave instability for sufficiently small base shear.

Fixing the value of s , we solve numerically equation (6.10) for the solution curve $m = m_d(n)$. In figure 25, we show these solution curves for several representative values of s , ranging from small, to medium, to large. For large and small values of s , numerical solutions can be verified with analytical asymptotics. It is difficult to get numerical solutions for very large s . In particular, we obtain the point $(n = n_0, m = 1)$ which is approached when $s \uparrow \infty$ by the m_d curves of the R and S sectors (the upper and lower branches in figure 25).

As was established in the last paragraph of section 6.2.1, at any boundary point of a critical curve, the latter is tangent to the threshold curve through that quasi-intersection point of the two curves. Hence, since in the R sector the threshold curves have positive slopes (see figure 17), the same holds for the critical curves near their boundary points. This means that the critical function $\text{Bo}_{cM}(\text{Ma})$ is increasing near its boundary points. Therefore, if there is a maximum, then there must be a minimum between this maximum and the right-end quasi-intersection point. It transpires that as m rises through a certain threshold value m_t , such a maximum and a minimum appear at some (Ma, Bo) . The latter is an inflection point on the $m = m_t$ critical curve, where the tangent is horizontal. We call it an “extrema bifurcation point” (EBP; see figure 17 (c)). The EBPs, in both R and Q sectors, are discussed in detail below, in section 6.4.

6.2.3 The Q sector semi-infinite critical curves and their asymptotic behavior

Turning next to the Q sector, the cubic equation for Ma_0 has a single positive root and two non-physical complex conjugate roots. The physical root corresponds to the single “quasi-intersection” points in figure 20(a). Since the threshold curve has $\text{Bo} = \text{Bo}_{cL}(\text{Ma}) < 0$ and for the critical curve $\text{Bo} \rightarrow 0$ as $\text{Ma} \rightarrow \infty$, it is clear that the critical curve of the mid-wave instability lies above this threshold curve of the long-wave instability. This conclusion agrees with figure 20.

For the Q sector, the fact of the shared direction with the threshold curve at the boundary point of the critical curve, $d\text{Bo}/d\text{Ma} = \text{Bo}_2/\text{Ma}_2 = \kappa$, (see the last paragraph of section 6.2.1), implies that the function $\text{Bo}_{cM}(\text{Ma})$ is decreasing near the (single) quasi-intersection point. For $\text{Ma} \uparrow \infty$, postulating, from numerical results, that $\text{Bo} \rightarrow 0$ and also $\alpha \rightarrow 0$, we look for asymptotics $\text{Ma} = c_1\alpha^{-\zeta}$ (with $c_1 \neq 0$) and $\text{Bo} = d_1\alpha^\xi$ (with $d_1 \neq 0$), where ζ and ξ are positive, and substitute this into the system of equations (5.14) and (5.15). In more detail, these equations are (3.21), which for convenience is divided by Ma^2 , and its partial derivative with respect to α . Considering the first of these equations, it is clear that the second term is much smaller than the first one and the fourth and fifth terms are negligible in comparison with the third one. Thus, at leading order, the third term must balance the first one:

$$k_{20} + k_{31}\text{Ma}B = 0. \quad (6.12)$$

Since the $k_{20} \propto \alpha^6$, and $k_{31} \propto \alpha^8$, it follows that the product $\text{Ma}B \propto \alpha^{-2}$. Since $B = \text{Bo} + \alpha^2$ (which, clearly, entails that $\partial B/\partial \alpha = 2\alpha$), one can see that necessarily $\xi = 2$. This can be proved by showing that the assumption of $\xi < 2$ or $\xi > 2$ leads to a contradiction in the system consisting of (6.12) and

$$k'_{20} + k'_{31}\text{Ma}B + k_{31}\text{Ma}(2\alpha) = 0 \quad (6.13)$$

has the power $9 - \zeta$ which is greater than 5 (since $-\zeta + \xi = -2$, so $\zeta = 2 + \xi < 4$). Therefore, the last term of (6.13) is negligible compared to the other terms, which are clearly of power -5 . The first equation of the system yields $k_{206} + k_{318}c_1d_1 = 0$, and the second equation becomes $6k_{206} + 8k_{318}c_1d_1 = 0$, which is clearly contradictory for $c_1d_1 \neq 0$.

If we assume that $\xi > 2$ then $B = \alpha^2$ to leading order. The first equation of the system yields $k_{206} + k_{318}c_1 = 0$ and the second equation $6k_{206} + 8k_{318}c_1 + 2k_{318}c_1 = 0$. This system again has only the unacceptable solution $c_1 = 0$. Thus, we are left with $\xi = 2$, and therefore $\zeta = 4$. The system for c_1 and d_1 is now

$$k_{206} + k_{318}(1 + d_1)c_1 = 0$$

and

$$3k_{206} + k_{318}(5 + 4d_1)c_1 = 0.$$

Eliminating k_{206} from the last two equations yields $d_1 = -2$. Then

$$c_1 = \frac{k_{206}}{k_{318}} = \frac{3(n-1)(m-n^2)(n+1)^2}{n^2(n^3+m)^2} > 0.$$

Therefore, $\text{Bo} = c_1^{1/2}d_1\text{Ma}^{-1/2} < 0$. This is in excellent quantitative agreement with the numerical results documented in figure 20(a).

6.3 Local extrema of the critical curves

As figure 20 shows, in the Q sector there is a local maximum on the critical curve for m sufficiently close to n^2 , just as there is one at $m = n^2$, the boundary between the R and Q sectors (see figure 19). Taking into account that $\text{Bo}_{cM}(\text{Ma})$ is increasing at large Ma (as it is negative and goes up to zero in the limit of infinitely increasing Ma), we conclude that there must be at least two local minima on the critical curve, which is also in agreement with the numerical results shown in figure 20(a). For sufficiently large m , however, the critical curve is seen numerically to have just a single minimum.

At any extremum, be it in the R or the Q sectors, we have

$$\frac{d\text{Bo}}{d\text{Ma}} = 0. \quad (6.14)$$

Also, since substituting the solutions $\text{Bo}(\text{Ma})$ and $\alpha(\text{Ma})$ of the system of equations (5.14) and (5.15) for the critical curve into the left-hand side of equation (5.14) makes it true for all Ma , the total Ma -derivative of the left-hand side must be zero, i.e.

$$\frac{\partial C_0}{\partial \text{Ma}} + \frac{\partial C_0}{\partial \alpha} \frac{d\alpha}{d\text{Ma}} + \frac{\partial C_0}{\partial \text{Bo}} \frac{d\text{Bo}}{d\text{Ma}} = 0.$$

For the extremum, in view of equations (5.15) and (6.12), this leads to the third equation in addition to (5.14) and (5.15):

$$\frac{\partial C_0}{\partial \text{Ma}} = 0. \quad (6.15)$$

Thus the system of the three quadratic equations for the extrema points is

$$A_1 + A_2 \text{Ma} + A_3 \text{Ma}^2 = 0, \quad (6.16)$$

$$A'_1 + A'_2 \text{Ma} + A'_3 \text{Ma}^2 = 0, \quad (6.17)$$

$$A_1 + 2A_2 \text{Ma} + 3A_3 \text{Ma}^2 = 0. \quad (6.18)$$

Subtracting (6.16) from (6.18), we get the linear equation

$$A_2 + 2A_3 \text{Ma} = 0, \quad (6.19)$$

which can be solved for Ma in terms of the other variables, provided that $A_3 \neq 0$, i.e., since $k_{31} > 0$, that $B \neq 0$. On the other hand, another linear equation for Ma is obtained by eliminating the quadratic terms by linearly combining the quadratic equations (6.16) and (6.18),

$$2A_1 + A_2 \text{Ma} = 0. \quad (6.20)$$

This can also be solved for Ma in terms of the other variables (provided that $A_2 \neq 0$; also, it is easy to see that one has to assume that $B \neq 0$ in order to have a nonzero Ma). The solvability condition of the over-determined system of the two linear equations for Ma , (6.19) and (6.20), is

$$\mathcal{D} = 0, \quad (6.21)$$

where we have introduced the notation

$$\mathcal{D} = A_2^2 - 4A_1A_3, \quad (6.22)$$

which is independent of Ma .

One has to distinguish the cases $B \neq 0$ and $B = 0$. For $B \neq 0$, the solution of equation (6.19) is

$$\text{Ma} = -\frac{A_2}{2A_3}. \quad (6.23)$$

Substituting this into the quadratic equation (6.6), we have a system of two transcendental equations for B and α , which can be written in the following form:

$$\mathcal{D} = 0, \quad (6.24)$$

$$\mathcal{D}' = 0. \quad (6.25)$$

In the R -sector, two solutions, a maximum and a minimum, are found by solving numerically the system of equations, (6.24) and (6.25), and then finding Ma from (6.23). In the Q sector, this gives a single solution, which is a maximum for $m < m_N$, and a minimum for $m > m_N$.

Also, there are, in a certain interval of viscosity ratios, solutions with $B = 0$. In this case, the solvability condition (6.21) implies

$$k_{20} = 0, \quad (6.26)$$

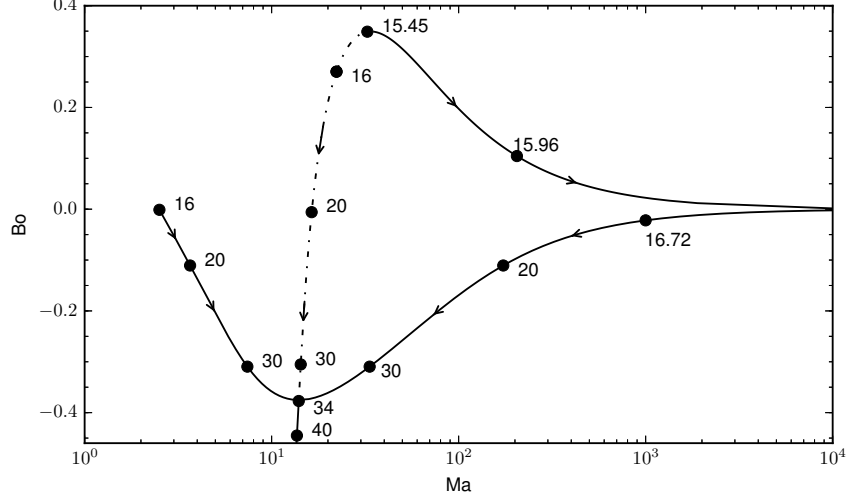


Figure 26: The trajectories of the extrema of the critical curves $\text{Ma} = \text{Ma}_{cM}(\text{Bo})$ in the (Ma, Bo) -plane (for $n = 4$ and $s = 1$; see figures 17(c) and (d), 19(a), and 20(a)) as m changes starting in the R sector and increasing through the R sector and after that, for $m > 16$, the Q sector. In the R sector, for $15.45 < m < 16$, there is one maximum, the dashed curve, and one minimum, the solid curve, for $16 < m < 34.31$, there is one maximum between two minima, and finally, for $m > 34.31$ there is one minimum. The arrows indicate the increase of m and the dots correspond to the displayed values of m next to them. The minimum moves to infinite Ma as $m \rightarrow 16$, from either side.

which yields the wavenumber. Then the Bond number is determined uniquely as

$$\text{Bo} = -\alpha^2. \quad (6.27)$$

The quadratic equation (6.17), with the now known α and Bo , gives two distinct solutions for the Marangoni number if the discriminant ζ is positive, where

$$\zeta = A_2'^2 - 4A_1'A_3'. \quad (6.28)$$

For the case at hand we have the simplified relations $A_2' = k_{20}'$, $A_1' = 2\alpha k_{11}$, and $A_3' = 2\alpha k_{31}$. Thus, the solutions are

$$\text{Ma} = \frac{-k_{20}' \pm \sqrt{k_{20}'^2 - 16\alpha^2 k_{11} k_{31}}}{4k_{31}\alpha}, \quad (6.29)$$

corresponding to the two minima on the critical curves in the Q sector (see figure 20).

Figure 26 shows the trajectories of the extrema in the (Ma, Bo) -plane for $n = 4$ as the viscosity ratio m increases, starting from $m = 15.45$, in the R sector, reaching the Q sector at $m = 16$, and continuing to increase in the Q sector. Consistent with the stability diagrams shown in figures 17 and 19, there are two extrema, a maximum and a minimum, for $m < 16$, which is in the R sector, provided $m > m_t = 15.45$. In the Q sector, there are three extrema as long as $m < m_N$. At $m = m_N$, the three extrema, one of them a maximum and two of them minima, collapse together into a single minimum, which then persists through the Q sector. (Recall that we term this point the extrema bifurcation point (EBP)).

In connection with the non-monotonic character of critical curves that have multiple local extrema, we note the following. In panels (e) and (f) of figure 15 (where $n = 2$), we see that as Ma increases, the long-wave instability gives way to stability at $\text{Ma} = \text{Ma}_{cL}$, which persists up to $\text{Ma} = \text{Ma}_{cM}$, at which point the mid-wave instability sets in, further persisting for all larger Ma . For short, we symbolically describe this sequence of Ma -intervals with different stability types as L-S-M, (where L indicates the long-wave instability, S denotes stability, and M stands for the mid-wave instability). The same stability interval sequence is obtained from figure 20 (where $n = 4$) if, e.g., we fix $m = 25$ and $\text{Bo} = -0.1$, and go rightwards parallel to the Ma -axis. However, different sequences occur for other sets of parameters. For example, at $m = 20$ and

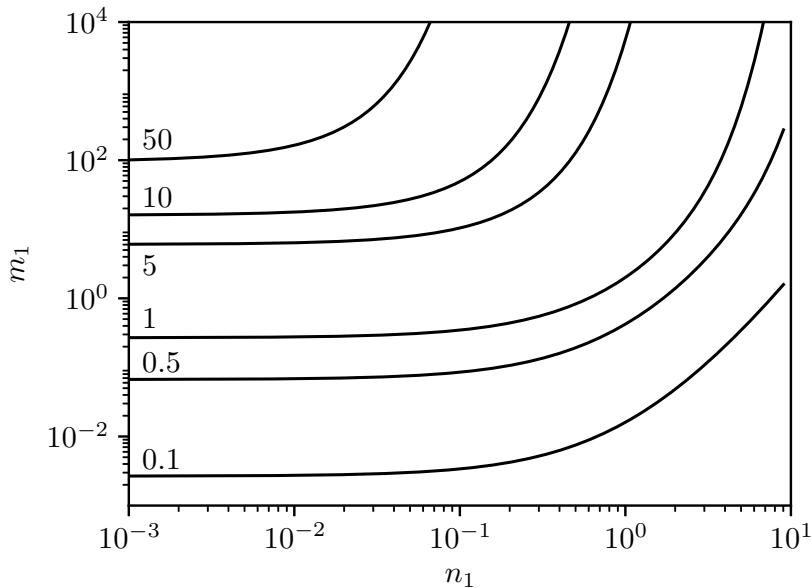


Figure 27: Level curves of $\alpha(n_1, m_1)$ for the extrema bifurcation points in the Q sector. The numbers next to the curves are the corresponding values of α .

$Bo = -0.05$, we observe the sequence L-S-M-S-M; at $m = 36$ and $Bo = -0.3$, the sequence is L-M-S-M; and at $m = 25$ and $Bo = -0.2$, we have the longer sequence L-M-S-M-S-M. It appears that for any $Bo < 0$, any sequence starts with L and ends with M. In contrast, for positive Bo , e.g., at $Bo = 0.05$ and $m = 18$, we have a S-M-S sequence of Ma-intervals.

6.4 Extrema bifurcation points

6.4.1 The EBP in the Q sector

We turn now to the problem of equations determining the extrema bifurcation points. In this section, we consider those in the Q -sector, while those in the R -sector are examined in the following section.

Clearly, the bifurcation point of the two minima and one maximum at $m = m_N$ in the Q sector, which has $B = 0$ (inherited, by continuity, from the $B = 0$ property of the two minima existing at the smaller m), must satisfy, in addition to equations (5.14), (5.15) and (6.15), the condition that the Ma values of the two minima coalesce to a double root. It is clear from equation (6.29) that this means

$$k_{20}'^2 - 16\alpha^2 k_{11} k_{31} = 0. \quad (6.30)$$

As we already noted above, the latter corresponds to the discriminant (6.28) being zero, so that the two Ma solutions of (6.17) for the two minima merge into just a single one. For the extrema bifurcation points in the Q sector, it is convenient to use new variables $n_1 = n - 1$ and $m_1 = (m - n^2)/(n - 1)$ so that the Q sector corresponds to the entire first quadrant. For any given (n_1, m_1) , as we already mentioned above, we can find the other properties of the EBP as follows: First, α is determined by solving equation (6.26) (which can be simplified, yielding that the quantity within the curly-bracket of k_{20} in (B.7), denoted by \mathcal{C} , must vanish). This dependence $\alpha(n_1, m_1)$ is shown as the contour plot in figure 27. We observe this unique solution for the extended region of realistic (n_1, m_1) . For small n_1 and α , we find that asymptotically $m_1 = (4/15)\alpha^2$, independent of n_1 , so that the level curves of α intersect the vertical axis at different heights. With corrections, the equation of the level curves at $\alpha \ll 1$ and $n_1 \ll 1$ is $m_1 = 4/15\alpha^2(1 + 5n_1/2 + 2n_1^2)$, where we have suppressed the terms which have powers of α^2 higher than one or powers of n_1 higher than

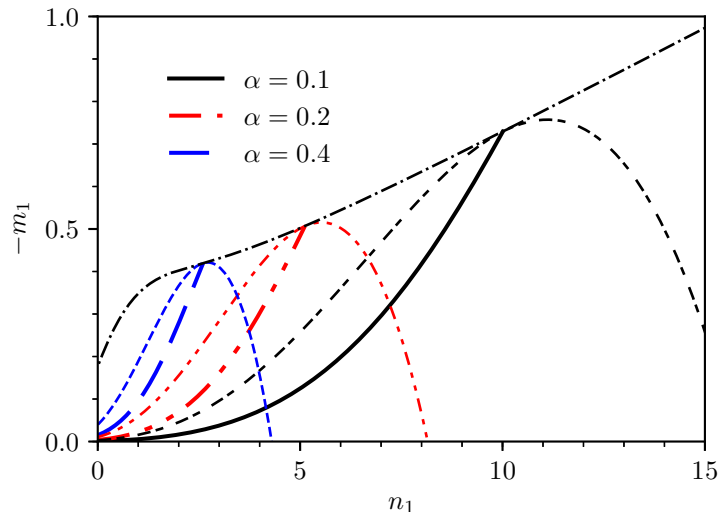


Figure 28: Level curves of $\alpha(n_1, m_1)$ for the extrema bifurcation points in the R sector. (For other curves, see the text.)

two. Keeping the two correction terms in the formula is necessary for predicting the flip of the sign of the level curve curvature as one switches between the linear and log scales of the n_1 -axis.

Having found α from equation (6.26), the Bond number $\text{Bo}(n_1, m_1)$ is given by equation (6.27) with $\alpha = \alpha(n_1, m_1)$. Next, equation (6.30), after being divided through by s^2 , is a linear equation in s^2 , and gives $s(n_1, m_1)$, provided the derivative of k_{20} with respect to α is negative. In view of $k_{20} = 0$, it is enough to require that $\mathcal{C}' < 0$. There is a strong evidence that the latter is indeed the case. At fixed n_1 and m_1 , $\mathcal{C} > 0$ and growing at sufficiently small α ; asymptotically, we find that $\mathcal{C} = \frac{1}{9}\varphi n^2 (n_1 + 2) n_1 m_1 \alpha^8$. This factor attains a (positive) maximum and then monotonically decreases; asymptotically, at $\alpha \uparrow \infty$, we have $\mathcal{C} = -\frac{1}{32}(m+1)\exp(4\alpha n + 2\alpha)$. Since \mathcal{C} is decreasing at its zero, it is clear that $\mathcal{C}' < 0$ at that α , and this is confirmed by numerics. In addition, for a few fixed values of n_1 , we computed $\alpha(n_1, m_1)$ and the corresponding \mathcal{C}' up to large values of m_1 , e.g. $m_1 = 10^6$, and this always showed $\mathcal{C}' < 0$. We find analytically that the large- m_1 log-log asymptotic slope is $d \ln(-\mathcal{C}')/d \ln m_1 = 4(n_1 + 1)/n_1$ (with the logarithmic asymptotics $d\alpha/d \ln m_1 = (1/2)n_1$). These asymptotic results are in excellent agreement with the numerical computations (which are not shown).

Finally, $\text{Ma}(n_1, m_1)$ of the EBP is given by (6.29) with discriminant equal to zero, so that

$$\text{Ma} = \frac{-k'_{20}}{4k_{31}\alpha}. \quad (6.31)$$

For example, there is a solution that corresponds to the EBP in figure 26, with $n = 4$, $s = 1$, $m = m_N = 34.31$, $\text{Ma} = 13.97$, $\text{Bo} = -0.375$, and $\alpha = 0.61$. These values are also consistent with figure 20. Note that in figure 27, $\alpha(n_1, m_1)$ has no external parameters. The same is true of the other EBP dependencies: $\text{Bo}(n_1, m_1)$; $s(n_1, m_1)$; and $\text{Ma}(n_1, m_1)$.

6.4.2 The EBP in the R sector

It was mentioned above, at the end of section 6.2.2, that one maximum and one minimum appear at the EBP on the critical curve in the R sector corresponding to a threshold value m_t of m . It is clear that for this EBP

$$\frac{d^2 \text{Bo}}{d \text{Ma}^2} = 0$$

along the critical curve. (This bifurcation point of extrema corresponds to the inflection point with the horizontal tangent line in figure 17(c).) Here $\text{Bo}(\text{Ma})$ is one of the two functions defined implicitly by the

system (5.14) and (5.15), where the other implicit function is $\alpha(\text{Ma})$. By the well-known formula for the derivative of an implicit function we have

$$\frac{d\text{Bo}}{d\text{Ma}} = \frac{\partial(C_0, C'_0)}{\partial(\alpha, \text{Ma})} \left[\frac{\partial(C_0, C'_0)}{\partial(\text{Bo}, \alpha)} \right]^{-1}.$$

We differentiate this expression with respect to Ma , taking into account (5.14), (5.15) and (6.15). As a result, we obtain a fourth equation of the system for the bifurcation point of the extrema:

$$\left(\frac{\partial^2 C_0}{\partial \alpha \partial \text{Ma}} \right)^2 - \frac{\partial^2 C_0}{\partial \alpha^2} \frac{\partial^2 C_0}{\partial \text{Ma}^2} = 0,$$

which is, more explicitly, given by

$$2\text{Ma}(A_2 + 3A_3\text{Ma})(A'_1 + A'_2\text{Ma} + A'_3\text{Ma}^2) - (A'_1 + 2A'_2\text{Ma} + 3A'_3\text{Ma}^2)^2 = 0. \quad (6.32)$$

We note that $\text{Bo} > 0$ in the R sector and therefore $B \neq 0$. The four equations, (6.24), (6.25), (6.23), and (6.32), are solved numerically. As an example, for $n = 4$ and $s = 1$, we find $\alpha = 0.21$, $\text{Bo} = 0.35$, $\text{Ma} = 33.81$ and $m = m_t = 15.45$. These numbers are consistent with figure 17(c) and figure 26.

Similarly to the Q sector procedure used above, for the four EBP equations in the R sector, an algebraic reduction is possible where a single equation is used to solve for one variable, and then the three other parameters of the EBP are found (with given values of n and m). For this, we note the algebraic identity $k_{22}^2 - 4k_{13}k_{31} = 0$. Hence, equation (6.24) can be written, explicitly showing the s and B dependencies, as

$$k_{20s}^2 s^2 + 2B^2 k_{sB} = 0 \quad (6.33)$$

and equation (6.25) is written as

$$k_{20s} k'_{20s} s^2 + B^2 k'_{sB} + 4B\alpha k_{sB} = 0. \quad (6.34)$$

Here we have defined the quantity k_{sB} as $k_{sB} = k_{20s}k_{22} - 2k_{11s}k_{31}$, where k_{20s} and k_{11s} are defined by $k_{20s} = k_{20}/s^2$ and $k_{11s} = k_{11}/s^2$. The last two displayed equations are linear equations for s^2 , so s^2 is obtained explicitly in terms of the quantities α , m , n , and B . Moreover, the solvability condition of the over-determined system of the two linear equations for s^2 yields (after dividing through by Bk_{20s}) a linear equation for B ,

$$B(k_{20s}k'_{sB} - 2k'_{20s}k_{sB}) + 4k_{20s}\alpha k_{sB} = 0, \quad (6.35)$$

whose coefficients depend on α , m , and n . Solving it (provided that the coefficient of B is nonzero) yields B in terms of α , m , and n ; using this expression in equation (6.33), we obtain s^2 in terms of α , m , and n , and then, from equation (6.23), an expression for Ma in terms of α , m , and n . Substitute these expressions into (6.32) to obtain an equation containing α , m , and n , which can be numerically solved for α giving it as a function of n_1 and m_1 . Then, for the given values of n_1 and m_1 , we find sequentially B , s^2 , and Ma , in that order, using the linear-equations solutions for them described above. Thus, for given n_1 and m_1 , we determine all the parameters, α , B , s , and Ma , of the corresponding EBP in the R sector. The level curves of α are seen in figure 28 as the monotonically rising curves. Through the upper point of each curve passes the level curve, with the same value of α , of the α function which makes identically vanish the coefficient B_d of B in equation (6.35). It is clear that the envelope of the family of level curves for $B_d = 0$ is the locus of the upper ends of the level curves for the EBPs. (The envelope curve shown in the figure was obtained by solving the system $B_d = 0$ and $\partial B_d / \partial \alpha = 0$.) When approaching the envelope curve, the values of B grow to infinity. The EBP level curves can be formally continued above the envelope curve, but lead to unphysical negative values of B and Ma . (Note that the R sector is completely mapped into the region of the $(n_1, -m_1)$ -plane bounded above by the line $-m_1 = n_1 + 2$, corresponding to $m = 1$; however, this line is outside the range of figure 28.)

7 Summary and discussion

In this paper, we have considered the linear stability of two immiscible viscous fluid layers flowing in the channel between two parallel plates that may move steadily with respect to each other driving a Couette

flow. The combined effects of gravity and an insoluble surfactant monolayer at the fluid interface were examined for certain flows such that the effect of inertia on their stability properties is negligible. The bulk velocity components satisfy linear homogeneous equations with constant coefficients. Therefore, their general solution, in the standard normal-mode analysis, is available with a few undetermined constants. The latter are determined, by the plate and interfacial-balance boundary conditions, in terms of the interface deflection and surfactant disturbance amplitudes. This yields a system of two algebraic linear homogeneous equations for the latter two amplitudes. Nontrivial solutions of this algebraic eigenvalue problem exist only if the increment γ , the complex “growth rate,” satisfies a quadratic equation whose coefficients are known functions of the wavenumber α , the Marangoni number Ma , the Bond number Bo , the viscosity ratio m , the aspect ratio n , and the interfacial shear parameter s . The two solutions of this dispersion equation were shown to yield two continuous increment branches, defined almost everywhere in the wavenumber-parameters space (with a “branch cut” hypersurface excluded from it), and their real parts, the two continuous growth rate branches, were analyzed to infer conclusions concerning the stability of the flow. Similar to FH and subsequent papers, we call one of the branches the “robust” branch, as it is present even when $\text{Ma} = 0$, and we call the other one, that vanishes as $\text{Ma} \downarrow 0$, the “surfactant” branch. Thus, we have explicit formulas allowing us to readily compute the growth rates of instability for any given input values of the wavenumber and the five parameters of the problem.

In the long-wave analysis of FH, three open sectors in the part of the (n, m) -plane given by $n \geq 1$ and $m \geq 0$, categorizing the stability of the system without gravity ($\text{Bo} = 0$), were identified: the Q sector, ($m > n^2$), where both modes are stable; the R sector, ($n^2 > m > 1$), where only the robust branch is unstable; and the S sector, ($0 < m < 1$), where only the surfactant mode is unstable. The same long-wave sectors were found to be relevant for non-zero Bo in the lubrication theory of FH17. In the present paper, by using the long-wave asymptotics for the coefficients of the quadratic dispersion equation, we corroborate the lubrication approximation results of FH17 for the instability thresholds. In the S sector, the surfactant mode remains unstable for all Bo , that is for arbitrarily strong stabilizing gravity; while in the R sector the growth rate of the robust branch is unstable provided Bo is below some positive threshold value Bo_c . In the Q sector, both branches remain stable for $\text{Bo} \geq 0$, but the robust branch is long-wave unstable for the smaller values of Ma (while mid-wave unstable for larger values of Ma , so that there are longer waves that are stable, as discussed below), when Bo is below some negative Bo_c . We have obtained the long-wave marginal wavenumbers and extremum growth rates which depend on the two main orders of the growth rate expression and were not considered in FH17. In particular, the small- s behavior of the marginal wavenumber was obtained from the asymptotic form of our general equation for the marginal wavenumber. We have established that in the R sector there are parametric situations in which the stabilizing effects, responsible for the emergence of the marginal wavenumber, are due, instead of the capillary forces, as is usual for larger s , to the nontrivial combined action of gravitational and surfactant forces.

We also obtained the asymptotic small- s behavior of the (long-wave) growth rate maximum and its corresponding wavenumber, which yielded different power laws for the cases of zero and non-zero Bond numbers. The asymptotic behavior in nearing the instability thresholds in the different sectors was established as well.

The long-wave instabilities at the different borders between the three (n, m) -sectors were analyzed, such as the $S - R$ one, $m = 1$. For the latter case, it was not clear from the small-wavenumber expression for the growth rates, equation (4.25), whether the unstable mode belonged to the surfactant branch, or, alternatively, to the robust one. We used complex analysis to show that there are indeed two separate branches of the growth rate function continuous for all wavenumbers and all the values of the parameters, one of the branches everywhere positive and the other one everywhere negative. The surfactant branch is easily identified near the wavenumber axis in the wavenumber-Marangoni number space, as the one of the two branches which vanishes in this limit of Marangoni number approaching zero, and it turns out to be positive or negative for positive or negative Bond number, respectively. The same is then true in the alternative limit, the wavenumber approaching zero at a finite Marangoni number, (corresponding to equation (4.25)), since the branches keep their signs everywhere, and in particular the surfactant branch of the growth rate has the same sign near the Ma -axis as its sign near the α -axis. In this way, we established that the unstable mode, corresponding to the positive sign in equation (4.25), belongs to the surfactant (robust) branch for positive (negative) Bond numbers (and the stable mode belongs to the other branch, in each case).

For cases of arbitrary, (not necessarily small) wavenumbers, we still have explicit formulas for the stability quantities of interest, albeit more complicated and therefore, in general, studied numerically. It was found

that in the S sector and in the R sector sufficiently far from the Q sector, as well as in the Q sector for sufficiently small Marangoni numbers, the dominant-mode instability has a long-wave character, in the sense that the left endpoint of the interval of unstable wavenumbers is zero. Otherwise, in particular in the Q sector, for sufficiently large Marangoni numbers, the 'mid-wave' instability may occur, in which the interval of unstable wavenumbers is bounded away from zero. These two situations were considered in turn. An interesting phenomenon, the dispersion-curve reconnection, was observed in the S sector. Both branches are unstable for sufficiently negative values of Bond number, and, as Bo decreases further, the robust-mode dispersion curve starts to cross the other dispersion curve at a single intersection point. Later in this process, at some sufficiently large value of $|Bo|$, the four parts of the two curves emanating from the intersection point recombine and detach, forming two new, non-intersecting, continuous curves, with the upper curve having two local maxima, of unequal heights. Then, as the Bond number decreases further, a jump in the global maximum may occur, as the shorter local maximum grows and eventually overcomes the other local maximum (figure 10).

The long-wave instability was studied with respect to gravity effects, as indicated by the dependencies of the characteristic dispersion quantities on the Bond number, figure 9, and, in the S and R sectors, with respect to the surfactant effects, as expressed in the dependencies on the Marangoni number, figure 11. For the small and large values of these parameters, the relevant wavenumbers may be small, allowing for simpler asymptotics. Even when the limits of the characteristic dispersion quantities are not small, we sometimes get simplified equations which are easier to solve numerically, or, occasionally, even approximate analytic expressions, such as equation (5.10).

In the R and S sectors, at a fixed Bond number, the long-wave growth rate has a maximum at certain finite values of the wavenumber and the Marangoni number. We have observed, numerically, that both the maximum growth rate and its Marangoni number, grow linearly with the shear parameter s , starting from zero, while the corresponding wavenumber, which starts from zero as well, grows very fast at first, but then remains almost constant at larger s (figure 13). Similar dependencies take place in the Q sector as well (figure 16).

The mid-wave instability turns out to emerge in two distinct ways (as a control parameter increases): it starts either from a stability stage, which we call the true onset of the mid-wave instability, or, alternatively, from a long-wave instability stage. The latter occurs when the left endpoint of the interval of the unstable wavenumbers, which is zero for the long-wave instability, starts moving away from zero (as shown in figure 18(b)), the maximum growth rate remaining positive all along. In the alternative scenario of the onset of the mid-wave instability, the maximum growth rate is equal to zero at a certain positive wavenumber, for which, therefore, the marginal wavenumber equation holds. But in view of the maximum, the partial derivative of the growth rate equals zero as well. Thus, we have a system of two equations, whose solution gives the critical values of the Marangoni number and the wavenumber as a function of the Bond number, for arbitrarily fixed values of the remaining three parameters. We follow, as the viscosity ratio is increased in the R sector toward its border with the Q sector, the emergence of the critical curve, and its consequent change, in the Marangoni number-Bond number plane (figure 17). The critical curve has its two endpoints on the threshold curve of the long-wave instability. The latter is rightward-increasing in the R sector, horizontal at the boundary with the Q sector (figure 19), and a decreasing curve in the Q sector (figure 20). The right-side endpoint of the critical curve moves away to infinity as we cross into the Q sector. The critical wavenumber is small near a critical curve endpoint, and so one can look for the critical solutions in the form of asymptotic power series. This gives rise to a cubic equation for the endpoint locations. Analysis of this equation leads to conclusions which are in agreement with the numerical observations, such that the critical curve in the R sector exists only above a certain value of the viscosity ratio and has two endpoints, while there is just one single endpoint in the Q sector. In all cases, the critical curve at its end point is tangent to the long-wave threshold curve. We also obtain and solve equations for the extrema of the critical curve, obtaining conclusions that agree with the numerical results. In the R sector, there is a certain value of the viscosity ratio below which the critical curve has no extrema, but above which it has exactly two extrema: a maximum and a minimum. The latter disappears into the right-side infinity at the boundary with the Q sector, and so we have just one extremum at this boundary, a maximum. Moving into the Q sector as the viscosity ratio increases, there are at first one maximum in between two minima on the critical curve. These extrema coalesce into a single minimum at a certain value of the viscosity ratio m , and this minimum persists for the larger values of m .

As we go from an arbitrary critical point to a critical extremum, one more constraint is added, which decreases the number of free parameters by one. The 'extrema bifurcation points', at which the number of extrema changes, correspond to another reduction of the number of free parameters. Thus, for given n and m , they determine all the other values: the wavenumber, Marangoni number, Bond number, and the shear parameter of the corresponding extrema bifurcation point (figure 28). Thus, figures 14, 15, 20, 26 and 28 represent different levels of information about the stability properties. Namely, going from one of the figures to the next, in the given order, the description gets more refined. On the other hand, the amount of data in the description decreases, in a certain sense. Figure 14 gives the growth rates at every wavenumber, but all the parameters are fixed at certain values. So, out of the seven quantities, α , γ_R , Ma, Bo, m , n and s , six are independent variables, and just one quantity is a dependent variable. Thus, these data make up a six-dimensional hypersurface in the seven-dimensional space. Figure 15 corresponds to some five independent variables determining the values of the other two quantities, thus resulting in a five-dimensional manifold of data. Figure 20 corresponds to a four-dimensional manifold, figure 26 implies a three-dimensional manifold of data, and figure 28 corresponds to a two-dimensional manifold parameterized by the independent variables m and n , whose values determine α , γ_R , Ma, Bo, s , (where $\gamma_R = 0$ since our consideration here is confined to the critical conditions of mid-wave instability.) The envelope curve in figure 28 corresponds to a one-dimensional curve in the seven-dimensional space of the relevant quantities. Finally, for the inflection point of the envelope curve in figure 28, there are no independent variables, and all seven quantities are uniquely determined.

There is the mid-wave instability of the robust branch in the S sector too, albeit the long-wave instability of the surfactant branch is the stronger of the two there. In the (Ma,Bo)-plane, in the vicinity of the threshold line of the long-wave instability, in addition to the more usual critical mid-wave curve which consists of the points that correspond to dispersion curves with zero maximum growth rate, there is, below the latter, another critical mid-wave curve, consisting of the points corresponding to dispersion curves with zero minimum growth rate (see figure 21). Correspondingly, as the Bond number decreases (to bigger-magnitude negative values), it is possible that at some point after the onset of the mid-wave instability, the long-wave instability starts, whose wavenumber interval is initially small and does not intersect the mid-wave interval of unstable wavenumbers. The coexistence of the mid-wave and the long-wave instabilities lasts until their intervals coalesce, corresponding to the critical curve of zero minimum growth rates in the (Ma,Bo)-plane. After this coalescence, there is just one long-wave continuous interval of the unstable wavenumbers, with the dispersion curve having two positive local maxima of the growth rate at first, but just one single maximum eventually, at the most negative Bond number values. For another range of Marangoni number, an alternative scenario is possible, which differs from the one described above solely in that the long-wave instability starts first and the mid-wave one at the smaller (more negative) values of the Bond number. The consequent coalescence into purely long-wave instability is the same in both scenarios (figures 23 and 22).

A The Continuous Branches of the Growth Rate Function

Recall that the two distinct analytic branches of the function $\sqrt{\zeta}$ exist in any simply connected domain in the complex plane that does not contain the origin ($\zeta = 0$). As was mentioned in the text, it may happen for the discriminant ζ of the dispersion relation that $\zeta = 0$ for some values of α and the parameters. This implies the two real equations, $\text{Re}(\zeta) = 0$ and $\text{Im}(\zeta) = 0$. The imaginary part of ζ (3.16) is

$$\text{Im}(\zeta) = \frac{s}{\alpha^5} \left(k_{Ma} \text{Ma} + \frac{k_b}{\alpha^2} (\text{Bo} + \alpha^2) \right) \quad (\text{A.1})$$

with the coefficients here

$$\begin{aligned} k_{Ma} = & (m-1)(\alpha n + \alpha n^2 - n^2 s_\alpha c_\alpha - s_{\alpha n} c_{\alpha n}) \\ & \times (m(s_\alpha^2 - \alpha^2)(\alpha n + s_{\alpha n} c_{\alpha n}) + (\alpha + s_\alpha c_\alpha)(s_{\alpha n}^2 - \alpha^2 n^2)) \\ & + 2(s_{\alpha n} - n s_\alpha)(n s_\alpha + s_{\alpha n})(-\alpha^4(-1+m)^2 n^2 + (m c_{\alpha n} s_\alpha + c_\alpha s_{\alpha n})^2 \\ & + \alpha^2(-c_\alpha n^2 m^2 + n(-c_\alpha^2 n + m(-2 + m n s_\alpha^2)) + s_{\alpha n}^2)) \end{aligned}$$

and

$$k_b = (m-1)(n(\alpha + \alpha n - c_{\alpha n} s_\alpha) - c_{\alpha n} s_{\alpha n})(\alpha^3 n(m+n) + s_\alpha s_{\alpha n}(m c_{\alpha n} s_\alpha + c_\alpha s_{\alpha n}) - \alpha^2(c_{\alpha n}^2 s_\alpha + m c_{\alpha n} s_{\alpha n}) - \alpha(m n s_\alpha^2 + s_{\alpha n}^2))$$

As we mentioned before, the two equations $\text{Re}(\zeta) = 0$ and $\text{Im}(\zeta) = 0$ define a manifold of codimension two in the α -parameter space. This manifold is analogous to a multivalued-function branch point in the complex plane. We consider the trace of this “branch manifold” in the three-dimensional space of $(\alpha, \text{Ma}, \text{Bo})$, with the rest of the parameters fixed, as follows. Solving $\text{Im}(\zeta) = 0$ for Marangoni number yields

$$\text{Ma} = -\frac{k_b}{\alpha^2 k_{Ma}}(\text{Bo} + \alpha^2). \quad (\text{A.2})$$

Note that not all values of (Bo, Ma) are appropriate here because Ma must be positive.

Similarly to the above expression for $\text{Im}(\zeta)$, we obtain

$$\text{Re}(\zeta) = \frac{1}{\alpha^{10}} \left(K_{20} \text{Ma}^2 + K_{02} (\text{Bo} + \alpha^2)^2 + K_{11} \text{Ma}(\text{Bo} + \alpha^2) + K_{00} \right),$$

where

$$\begin{aligned} K_{20} &= \frac{1}{4} \alpha^4 (\alpha n (\alpha^2 (m+n) + \alpha c_{\alpha n} s_\alpha - s m s_\alpha^2) - m c_{\alpha n} (s_\alpha^2 - \alpha^2) s_{\alpha n} - (\alpha + c_\alpha s_\alpha) s_{\alpha n}^2)^2, \\ K_{02} &= \frac{1}{4} (\alpha^3 n(m+n) + s_\alpha s_{\alpha n} (m c_{\alpha n} s_\alpha + c_\alpha s_{\alpha n}) - \alpha^2 (c_{\alpha n}^2 s_\alpha + m c_{\alpha n} s_{\alpha n}) - \alpha (m n s_\alpha^2 + s_{\alpha n}^2))^2, \\ K_{11} &= \frac{1}{2} \alpha^2 (m (s_\alpha^2 - \alpha^2) (s_{\alpha n}^2 - \alpha^2 n^2) ((\alpha + c_\alpha s_\alpha) (c_{\alpha n} s_{\alpha n} - \alpha n) + (c_\alpha s_\alpha - \alpha) (\alpha n + c_{\alpha n} s_{\alpha n})) \\ &\quad + (c_\alpha^2 s_\alpha^2 - \alpha^2) (s_{\alpha n}^2 - \alpha^2 n^2)^2 \\ &\quad + m^2 (s_\alpha^2 - \alpha^2)^2 (c_{\alpha n}^2 s_{\alpha n}^2 - \alpha^2 n^2) + 2 (s_\alpha^2 - \alpha^2) (s_{\alpha n}^2 - \alpha^2 n^2) (\alpha^4 (m-1)^2 n^2 \\ &\quad - (m c_{\alpha n} s_\alpha + n c_\alpha s_\alpha)^2 + \alpha^2 (m^2 c_{\alpha n}^2 + n (n c_\alpha^2 + m (2 - m n s_\alpha^2)) - s_{\alpha n}^2))), \\ K_{00} &= -s^2 \alpha^6 (m-1)^2 (-\alpha n (1+n) + c_{\alpha n}^2 s_\alpha + c_{\alpha n} s_{\alpha n})^2. \end{aligned}$$

To solve the system $\text{Re}(\zeta) = 0$ and $\text{Im}(\zeta) = 0$ for Ma and Bo as functions of α (with s , m , and n fixed), equation (A.2) is substituted into $\text{Re}(\zeta)$ which yields

$$\text{Re}(\zeta) = AB^2 + C = 0, \quad (\text{A.3})$$

where $B = \text{Bo} + \alpha^2$, and A and C do not depend on Ma :

$$A = \frac{1}{\alpha^{10}} \left(\frac{k_b^2}{\alpha^4 k_{Ma}^2} K_{20} + K_{02} - \frac{k_b}{\alpha^2 k_{Ma}} K_{11} \right), \quad C = \frac{K_{00}}{\alpha^{10}}.$$

Therefore, $\text{Bo} = \text{Bo}(\alpha)$, where

$$\text{Bo}(\alpha) = -\alpha^2 \pm \sqrt{-\frac{C}{A}}. \quad (\text{A.4})$$

Substituting (A.4) for Bo into equation (A.2) yields Ma such that $\zeta = 0$ for a given α . Only the unique value $\text{Bo} = \text{Bo}(\alpha)$ that yields $\text{Ma} = \text{Ma}(\alpha) > 0$ is admitted here. In figures 29(a) and (b) curves $\text{Bo} = \text{Bo}(\alpha)$ and $\text{Ma} = \text{Ma}(\alpha)$ are plotted for various values of m . One can see that $\text{Ma} \uparrow \infty$ in the limit $\alpha \downarrow 0$ for all m . In this limit, $\text{Bo} \uparrow \infty$ for $m > 1$, but $\text{Bo} \uparrow -\infty$ for $m < 1$. At $\alpha \uparrow \infty$, for all m , $\text{Bo} \sim -\alpha^2$ and $\text{Ma} \downarrow 0$. There are no points where the discriminant is zero for $m = 1$, as was shown in the main text for all parameter values (formally, in the figure, we get $\text{Ma}(\alpha) = 0$ and $\text{Bo}(\alpha) = -\alpha^2$). This indicates that the branch manifold consists of at least two pieces, and perhaps more than two, some with $m > 1$ and others with $m < 1$. The same fact is reflected in the infinite discontinuities of the curves in the figure at finite values of α , which take place provided $m > n^2$.

Also, if we consider the (α, Ma) -plane, with all the other parameters fixed, including Bo , corresponding to a horizontal line in figure 29(a), there will be at most two branch points in the (α, Ma) -plane since any

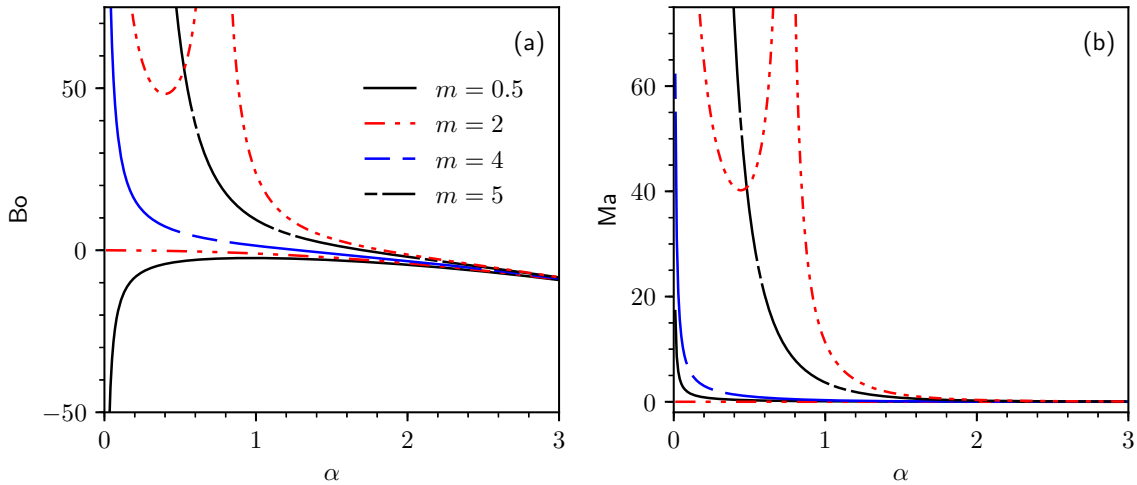


Figure 29: The curves (a) $Bo = Bo_m(\alpha)$ and (b) $Ma = Ma_m(\alpha)$ such that the discriminant $\zeta = 0$ are plotted for the values of viscosity ratio m indicated in the legend.

horizontal line there intersects any curve at no more than two points. Therefore, in some sufficiently narrow infinite strip whose left boundary is the (vertical) Ma -axis, the discriminant is non-zero at all its points, and so there are two continuous branches, in agreement with the long-wave results in the main text. These results also show no intersections of the two dispersion curves (when the wavenumbers are small enough), which means that $\text{Re} \sqrt{\zeta}$ is non-zero in a sufficiently narrow strip bordering the Ma -axis. The equation $\text{Re} \sqrt{\zeta} = 0$ implies that ζ is real (and negative). We have solved this equation for Ma as a function of α at fixed values of Bo (and the other parameters), and every resulting curve in the (α, Ma) -plane indeed lies entirely outside some strip bordering the Ma -axis.

Regarding the entire (α, Ma) -plane, if we remove from it the branch points together with the infinite rays emanating from each branch point to the right and going parallel to the α -axis, then in the remaining domain the discriminant is nowhere zero, and thus there are two continuous branches of the growth rate in this domain, smooth in α at each point that they are defined.

Next, we note that the horizontal line $Bo = 0$ in panel (a) of figure 29 intersects every curve whose $m > 1$. So, even in the absence of gravity, there may be intersections of the two dispersion curves. As Ma is varied, these intersections disappear at some Ma , with the reconnection of the curve parts lying to the right of the “marginal intersection” point and consequent separation of the two “renovated” dispersion curves. This happens in the ranges of wavenumbers when both branches are stable, which was not noted in HF.

Figure 30 shows, as an example, the curve in the three-dimensional space which corresponds to the two dash-dotted, $m = 2$, curves of figure 29. The coordinate box there is shown with its front, top, and right faces removed for a better view. The curve of zero discriminant starts at the back top right vertex and steadily goes downward and to the left simultaneously twisting first toward the viewer and then backward, until it ends at the back bottom left vertex.

Next, we demonstrate that there is always a strip $\mathcal{D}_s = \{0 < \alpha < \alpha_s, Ma > 0\}$ where $\zeta \neq 0$. Indeed, it appears in figure 29(a) that any horizontal line $Bo = Bo_f$ intersects any of the graphs of $Bo = Bo_m(\alpha)$ at no more than three points. If there are no intersections then the value of α_s is chosen completely arbitrarily. Otherwise, α_s must be smaller than the smallest α of the intersection points. For the purpose of this paper, the existence of \mathcal{D}_s (and thus of the two branches of the growth rate) is sufficient with any small but finite α_s . The existence of α_s is shown analytically for small values of α .

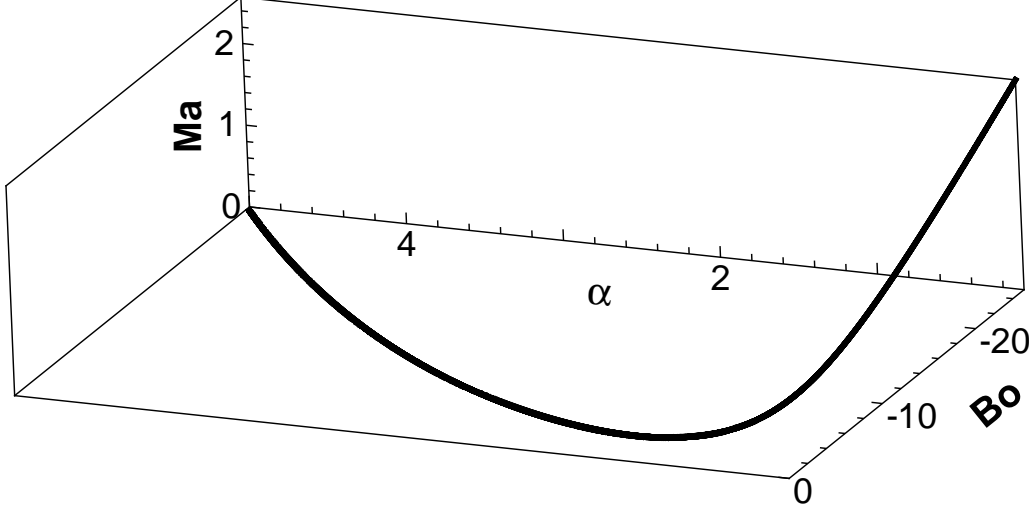


Figure 30: The zero discriminant curve corresponding to the $m = 2$ projection curves shown in panels (a) and (b) of figure 29.

B Coefficients of equations

The coefficients A_{11} , A_{12} , A_{21} , and A_{22} of equation (3.5) are:

$$\operatorname{Re}(A_{11}) = (m(s_\alpha^2 - \alpha^2)(s_{\alpha n}c_{\alpha n} - \alpha n) + (s_{\alpha n}^2 - \alpha^2 n^2)(s_\alpha c_\alpha - \alpha)) \frac{1}{2\alpha^5 F_2} B, \quad (\text{B.1})$$

$$\operatorname{Im}(A_{11}) = -\frac{(m-1)s}{\alpha^2 F_2} (n^2(s_\alpha c_\alpha - \alpha) + s_{\alpha n}c_{\alpha n} - \alpha n), \quad (\text{B.2})$$

$$A_{12} = (s_{\alpha n}^2 - \alpha^2 n^2 - mn^2(s_\alpha^2 - \alpha^2)) \frac{\operatorname{Ma}}{2\alpha^2 F_2}, \quad (\text{B.3})$$

$$\operatorname{Re}(A_{21}) = (s_{\alpha n}^2 - \alpha^2 n^2 - mn^2(s_\alpha^2 - \alpha^2)) \frac{1}{2\alpha^2 F_2} B, \quad (\text{B.4})$$

$$\operatorname{Im}(A_{21}) = (m((s_\alpha c_\alpha - \alpha)(s_{\alpha n}c_{\alpha n} + \alpha n) + c_{\alpha n}^2(s_\alpha^2 - \alpha^2) + \alpha^2 n^2 s_\alpha^2) + (s_\alpha c_\alpha + \alpha)(s_{\alpha n}c_{\alpha n} + \alpha n) + c_\alpha^2(s_{\alpha n}^2 - \alpha^2 n^2) + \alpha^2 s_{\alpha n}^2) \frac{s}{\alpha^3 F_2}, \quad (\text{B.5})$$

$$A_{22} = (m((s_\alpha^2 - \alpha^2)(s_{\alpha n}c_{\alpha n} + \alpha n)) + (s_{\alpha n}^2 - \alpha^2 n^2)(s_\alpha c_\alpha + \alpha)) \frac{\operatorname{Ma}}{2\alpha^3 F_2}. \quad (\text{B.6})$$

The coefficients k_{20} , k_{11} , k_{31} , k_{22} and k_{13} that appear in equation (3.21) are

$$\begin{aligned} k_{20} = & \frac{s^2}{4\alpha^6} (s_{\alpha n}^2 - n^2 s_\alpha^2) \{ (m-1) (s_{\alpha n}c_{\alpha n} - \alpha n + n^2 (s_\alpha c_\alpha - \alpha)) \\ & \times [m (s_\alpha^2 - \alpha^2) (s_{\alpha n}c_{\alpha n} + \alpha n) + (s_{\alpha n}^2 - \alpha^2 n^2) (\alpha + s_\alpha c_\alpha)] \\ & - (s_{\alpha n}^2 - s_\alpha^2 n^2) [m^2 (s_\alpha^2 - \alpha^2) (c_{\alpha n}^2 + \alpha^2 n^2) \\ & + 2m(n^2 \alpha^4 - n\alpha^2 + s_\alpha c_\alpha s_{\alpha n}c_{\alpha n}) + (c_\alpha^2 + \alpha^2) (s_{\alpha n}^2 - \alpha^2 n^2)] \}, \end{aligned} \quad (\text{B.7})$$

$$\begin{aligned} k_{11} = & \frac{s^2}{4\alpha^8} (m-1) (s_{\alpha n}^2 - s_\alpha^2 n^2) (s_{\alpha n}c_{\alpha n} - \alpha n + n^2 (s_\alpha c_\alpha - \alpha)) \\ & \times [m(s_{\alpha n}c_{\alpha n} - \alpha n) (s_\alpha^2 - \alpha^2) + (s_\alpha c_\alpha - \alpha) (s_{\alpha n}^2 - \alpha^2 n^2)], \end{aligned} \quad (\text{B.8})$$

$$\begin{aligned} k_{31} = & \frac{1}{16\alpha^{10}} (s_\alpha^2 - \alpha^2) (s_{\alpha n}^2 - \alpha^2 n^2) [(s_\alpha c_\alpha + \alpha) (s_{\alpha n}^2 - \alpha^2 n^2) \\ & + m(s_{\alpha n}c_{\alpha n} + \alpha n)(s_\alpha^2 - \alpha^2)]^2, \end{aligned} \quad (\text{B.9})$$

$$\begin{aligned}
k_{22} = & \frac{1}{8\alpha^{12}} (s_\alpha^2 - \alpha^2) (s_{\alpha n}^2 - \alpha^2 n^2) [m(s_{\alpha n} c_{\alpha n} - \alpha n)(s_\alpha^2 - \alpha^2) \\
& + (s_\alpha c_\alpha - \alpha) (s_{\alpha n}^2 - \alpha^2 n^2)] [m(s_{\alpha n} c_{\alpha n} + \alpha n)(s_\alpha^2 - \alpha^2) \\
& + (s_\alpha c_\alpha + \alpha) (s_{\alpha n}^2 - \alpha^2 n^2)],
\end{aligned} \tag{B.10}$$

and

$$\begin{aligned}
k_{13} = & \frac{1}{16\alpha^{14}} (s_\alpha^2 - \alpha^2) (s_{\alpha n}^2 - \alpha^2 n^2) [(s_\alpha c_\alpha - \alpha) (s_{\alpha n}^2 - \alpha^2 n^2) \\
& + m(s_{\alpha n} c_{\alpha n} - \alpha n)(s_\alpha^2 - \alpha^2)]^2.
\end{aligned} \tag{B.11}$$

The corresponding long-wave approximations are

$$k_{20} \approx k_{206}\alpha^6 + k_{208}\alpha^8, \tag{B.12}$$

where

$$k_{206} = \frac{n^4 s^2}{108} \varphi(n-1)(n+1)^2(m-n^2)$$

and

$$\begin{aligned}
k_{208} = & \frac{s^2}{810} (n-1)n^4(n+1)^3 (m^2(n(3n+8)+3) - 4m(n^2-1)n^2 \\
& - (n(3n+8)+3)n^4),
\end{aligned}$$

$$k_{11} \approx k_{116}\alpha^6 + k_{118}\alpha^8, \tag{B.13}$$

where

$$k_{116} = \frac{n^7 s^2}{81} (n-1)(n+1)^2(m-1)(n+m)$$

and

$$k_{118} = \frac{s^2}{1215} (m-1)(n-1)n^7(n+1)^2(m(n(8n-3)+7) + n(n(7n-3)+8)),$$

$$k_{31} \approx k_{318}\alpha^8, \tag{B.14}$$

where

$$k_{318} = \frac{n^6}{324} (n^3 + m)^2,$$

$$k_{22} \approx k_{228}\alpha^8, \tag{B.15}$$

where

$$k_{228} = \frac{n^8}{486} (n+m)(n^3+m),$$

and

$$k_{13} \approx k_{138}\alpha^8, \tag{B.16}$$

where

$$k_{138} = \frac{n^{10}}{2916} (n+m)^2.$$

The coefficient of the α^4 term that appears in equation (4.5) is

$$\begin{aligned}
k_S = & \frac{\text{Ma} (n^3 - 4n^2 + 4n - 1)}{60(m-1)} \\
& + \frac{\text{Ma}^3}{128(m-1)^5 n^4 (n+1) s^2} (n-1) (m^4(3n+1) + 2m^3(-3n^3 - 2n^2 + 4n+1)n \\
& + 4m^2(n^3 - 2n^2 - 2n+1)n^3 + 2m(n^3 + 4n^2 - 2n-3)n^5 + (n+3)n^8) \\
& + \frac{\text{BoMa}^2}{192(m-1)^4 n(n+1)^2 s^2} (m^3(3n^2 - 4n-3) + m^2(2n^3 + 13n^2 - 6n-5)n \\
& + m(-5n^3 - 6n^2 + 13n+2)n^3 + (-3n^2 - 4n+3)n^5) \\
& + \text{Bo}^2 \text{Ma} \frac{n^2(-m^2 + m(n-1)n + n^3)}{144(m-1)^3(n+1)^2 s^2}
\end{aligned} \tag{B.17}$$

The coefficients of the constant, quadratic and quartic terms of the marginal wavenumber equation (4.8) are

$$\zeta_0 = \frac{1}{108} s^2 (n-1)(n+1)^2 (m-n^2) \varphi \text{Ma} + \frac{1}{81} n^3 s^2 (n-1)(n+1)^2 (m-1)(n+m) \text{Bo}, \tag{B.18}$$

$$\begin{aligned}
\zeta_2 = & \frac{\text{Ma}}{810} (-1+n)(1+n)^3 (-4mn^2(-1+n^2) + m^2(3+n(8+3n)) - n^4(3+n(8+3n))) s^2 \\
& + \text{Bo} \frac{(-1+m)(-1+n)n^3(1+n)^2(n(8+n(-3+7n)) + m(7+n(-3+8n))) s^2}{1215} \\
& + \text{Bo} \frac{n^2}{2916} (3(m+n^3)\text{Ma} + n^2(m+n)\text{Bo})^2 + \frac{1}{81} s^2 n^3 (n-1)(n+1)^2 (m-1)(n+m)
\end{aligned} \tag{B.19}$$

and

$$\zeta_4 = \frac{1}{324} n^2 (m+n^3)^2 \text{Ma}^2, \tag{B.20}$$

where only the leading order term in s has been retained in ζ_4 , so that $\zeta_4 = \zeta_{40}$ of section 4.1.2.

The linear and cubic coefficients in Bo_c of expression (4.17) are given by

$$\begin{aligned}
\beta_1 = & \frac{1}{15} \left(\frac{(m^2-1)m}{m+n} - m^2 + \frac{2(m-1)m}{m-n^2} - \frac{6(m-1)(3mn+m+4n^2)}{3mn+m+(n+3)n^2} \right. \\
& \left. + (m-7)n + 4m + n^2 - 2 \right)
\end{aligned} \tag{B.21}$$

and

$$\beta_3 = \frac{1}{36} \frac{n^3(n+m)|n-1|\psi^2}{[\varphi s(m-n^2)(n+1)]^2 |m-1|}. \tag{B.22}$$

The constant, linear and cubic coefficients in Ma_{cL} , M_0 , M_1 and M_3 , of the expression (4.22) are

$$M_0 = \frac{4n^3(m-1)(m+n)}{3\phi(m-n^2)}, \tag{B.23}$$

$$\begin{aligned}
M_1 = & \frac{1}{15} \left(\frac{m(1-m^2)}{m+n} + \frac{2(m-1)m}{n^2-m} + \frac{6(m-1)(3mn+m+4n^2)}{\phi} \right. \\
& \left. - mn + (m-4)m - n^2 + 7n + 2 \right)
\end{aligned} \tag{B.24}$$

and

$$M_3 = -\frac{(n-1)\psi^2}{64(m-1)^3 n^3 (n+1)^2 s^2 (m+n)}. \tag{B.25}$$

C Long-wave formulas for F_0 , F_1 and F_2

The small wavenumber approximations for the case of finite thickness, n , and small Marangoni number, Ma are given here. The long-wave approximations of (3.9)-(3.14) are first written as polynomials in Ma and Bo , then the coefficients are expanded, so that keeping only the leading term in α , equations (3.9)-(3.14) are approximately

$$F_2 = \text{Re}(F_2) \approx \frac{1}{3} \psi, \quad (\text{C.1})$$

$$\text{Re}(F_1) \approx \frac{1}{9} n^3 (m+n) \alpha^4 + \frac{1}{3} n (m+n^3) \alpha^2 Ma + \frac{1}{9} n^3 (m+n) \alpha^2 Bo, \quad (\text{C.2})$$

$$\text{Im}(F_1) \approx \frac{2}{3} n^2 s (n+1) (1-m) \alpha, \quad (\text{C.3})$$

$$\text{Re}(F_0) \approx \frac{1}{36} n^4 \alpha^6 Ma + \frac{1}{36} n^4 \alpha^4 Ma Bo, \quad (\text{C.4})$$

$$\text{Im}(F_0) \approx \frac{1}{6} n^2 s (1-n^2) \alpha^3 Ma, \quad (\text{C.5})$$

where ψ is given by equation (4.7). For $m = 1$, we find

$$F_2 = \text{Re}(F_2) \approx \frac{1}{3} (n+1)^4, \quad (\text{C.6})$$

$$\text{Re}(F_1) \approx \frac{1}{9} n^3 (n+1) \alpha^4 + \frac{1}{3} n (n^3+1) \alpha^2 Ma + \frac{1}{9} n^3 (n+1) \alpha^2 Bo, \quad (\text{C.7})$$

$$\text{Im}(F_1) = 0, \quad (\text{C.8})$$

$$\text{Re}(F_0) \approx \frac{1}{36} n^4 \alpha^6 Ma + \frac{1}{36} n^4 \alpha^4 Ma Bo, \quad (\text{C.9})$$

and

$$\text{Im}(F_0) \approx \frac{1}{6} n^2 s (1-n^2) \alpha^3 Ma. \quad (\text{C.10})$$

D Normal modes with undisturbed surfactant

Assuming that the surfactant is undisturbed, $G = 0$, which implies that $h \neq 0$, it follows from the second equation of (3.5) that $A_{21} = 0$. This implies in particular that $\text{Im}(A_{21}) = 0$. However, in expression (B.5), each term is positive, since each of the expressions $s_\alpha c_\alpha - \alpha$, $s_\alpha^2 - \alpha^2$, and $s_{\alpha n}^2 - \alpha^2 n^2$ is positive. This contradiction shows that there are no normal modes with $G = 0$ if $s \neq 0$.

If, however, $s = 0$, but B is nonzero, then $\text{Im}(A_{21}) = 0$ identically. However, $\text{Re}(A_{21}) = 0$ yields, from equation (B.4), that

$$m = \frac{s_{\alpha n}^2 - \alpha^2 n^2}{n^2 (s_\alpha^2 - \alpha^2)}. \quad (\text{D.1})$$

This equation gives a two-dimensional manifold of normal modes (parameterized with variables n and α). Thus, the normal modes with $G = 0$ (and $h \neq 0$) do exist, but only when $s = 0$. Note that the first equation of the system (3.5) implies that $\gamma = -A_{11}$, and we find, making use of (D.1), the growth rate for this mode is

$$\gamma_R = -\text{Re}(A_{11}) = \left(\frac{s_{\alpha n} c_{\alpha n} - \alpha n}{n^2 (s_\alpha^2 - \alpha^2)} + s_\alpha c_\alpha - \alpha \right) (s_{\alpha n}^2 - \alpha^2 n^2) \frac{1}{2\alpha^5 F_2} B.$$

Thus, we have one nonzero branch of modes, which are the usual Rayleigh-Taylor modes for the stagnant base configuration. Also, for any negative Bo , if $B = 0$, that is $\alpha^2 = -Bo$, then $A_{21} = 0$ without any restrictions on m and n . We can see that $A_{11} = 0$ in this case as well, so that $\gamma_R = 0$, which indicates the marginal stability mode for the Rayleigh-Taylor instability of the stagnant base configuration.

References

- J. Bak and D.J. Newman. *Complex Analysis*. Springer, 2010.
- A. P. Bassom, M. G. Blyth, and D. T. Papageorgiou. Nonlinear development of two-layer Couette-Poiseuille flow in the presence of surfactant. *Phys. Fluids*, 22(10):102102, 2010.
- M. G. Blyth and C. Pozrikidis. Effect of inertia on the Marangoni instability of two-layer channel flow, Part II: normal-mode analysis. *J. Eng. Math.*, 50(2-3):329–341, 2004a.
- M. G. Blyth and C. Pozrikidis. Effect of surfactants on the stability of two-layer channel flow. *J. Fluid Mech.*, 505:59–86, 2004b.
- M. C. Cross and P. C. Hohenberg. Pattern formation outside of equilibrium. *Rev. Mod. Phys.*, 65:851–1112, Jul 1993. doi: 10.1103/RevModPhys.65.851. URL <https://link.aps.org/doi/10.1103/RevModPhys.65.851>.
- D. A. Edwards, H. Brenner, and D. T. Wasan. *Interfacial Transport Processes and Rheology*. Butterworth-Heinemann, Boston, 1991.
- A. L. Frenkel and D. Halpern. Stokes-flow instability due to interfacial surfactant. *Phys. Fluids*, 14(7):L45–L48, 2002.
- A. L. Frenkel and D. Halpern. Effect of inertia on the insoluble-surfactant instability of a shear flow. *Physics Review E*, 71(1):016302, 2005.
- A. L. Frenkel and D. Halpern. Strongly nonlinear nature of interfacial-surfactant instability of Couette flow. *Int. J. Pure Appl. Math.*, 29(2):205–224, 2006. URL <http://www.citebase.org/abstract?id=oai:arXiv.org:nlin/0601025>.
- A. L. Frenkel and D. Halpern. Surfactant and gravity dependent inertialess instability of two-layer Couette flows and its nonlinear saturation. *arXiv preprint arXiv:1610.04909*, 2016.
- A. L. Frenkel and D. Halpern. Surfactant and gravity dependent instability of two-layer Couette flows and its nonlinear saturation. *J. Fluid Mech.*, 826:158–204, 2017.
- D. Halpern and A. L. Frenkel. Destabilization of a creeping flow by interfacial surfactant: Linear theory extended to all wavenumbers. *J. Fluid Mech.*, 485:191–220, 2003.
- D. Halpern and A. L. Frenkel. Nonlinear evolution, travelling waves, and secondary instability of sheared-film flows with insoluble surfactants. *J. Fluid Mech.*, 594:125–156, 2008.
- A. Kalogirou and D. T. Papageorgiou. Nonlinear dynamics of surfactant-laden two-fluid Couette flows in the presence of inertia. *J. Fluid Mech.*, 802:5–36, 2016.
- J. Peng and K.-Q. Zhu. Linear instability of two-fluid Taylor-Couette flow in the presence of surfactant. *J. Fluid Mech.*, 651:357–385, 005 2010. doi: 10.1017/s002211200999406x.
- J. R. Picardo, T. G. Radhakrishna, and S. Pushpavanam. Solutal Marangoni instability in layered two-phase flows. *J. Fluid Mech.*, 793:280–315, 2016.
- C. Pozrikidis. Effect of inertia on the Marangoni instability of two-layer channel flow, Part I: numerical simulations. *J. Eng. Math.*, 50(2-3):311–327, 2004.
- A. J. Schweiger. *Gravity, surfactants, and instabilities of two-layer shear flows*. PhD thesis, The University of Alabama, 2013.
- H. H. Wei. On the flow-induced Marangoni instability due to the presence of surfactant. *J. Fluid Mech.*, 544:173–200, 2005.
- H. Wong, D. Rumschitzki, and C. Maldarelli. On the surfactant mass balance at a deforming fluid interface. *Phys. Fluids*, 8:3203–3204, 1996.
- C. S. Yih. Instability due to viscosity stratification. *J. Fluid Mech.*, 27:337–352, 1967.